Measurement of the Production Cross-Section of $Z \rightarrow \mu^+\mu^-$ with ATLAS at the LHC at $\sqrt{s} = 7$ TeV

by

John Charles Purdham

A dissertation submitted in partial fulfillment
of the requirements for the degree of
Doctor of Philosophy
(Physics)
in the University of Michigan
2011

Doctoral Committe:

Professor Rudolf P. Thun, Chair
Professor Robert L. Griess, Jr
Professor Bing Zhou
Assistant Professor Aaron T. Pierce

To my family.

Acknowledgements

There are a good many people without which this thesis would not have come to pass. First and foremost I owe an immense debt to my advisor, Rudolf Thun, whose guidance was instrumental in nearly every aspect of my graduate career. Next I thank the rest of the members of my committee—Bing Zhou, Aaron Pierce, and Robert Griess, Jr—for their insights, assistance, and willingness to help. Jianming Qian also provided valuable contributions, both in explaining the physics processes involved as well as the software used to investigate them. Further appreciation goes out to Junjie Zhu sharing his expertise on differential distributions. I thank Haijun Yang, for his work in preparing the data format and samples used in this thesis, as well as Tiesheng Dai for his assistance in several matters, most particularly with regard to Monte Carlo generation. In addition to that, he and Ed Diehl helped me with my work on the muon system, when I was doing calibration and commissioning studies while waiting for the LHC to be repaired and collision data to become available. I also thank Dan Levin for his time working with me on investigating J/ψ decays to muons and looking into the performance of the different muon reconstruction algorithms. Back when I thought I may be working on Higgs searches, Jonas Strandberg was of great help to me, and his assistance and mentorship have continued to influence me, even after our subjects of focus diverged. In a similar vein, I thank my fellow students, in particular Hao Liu and Aaron Armbruster. When we were all at CERN sharing tips and helping to troubleshoot each others' problems it was a most beneficial experience. I will close this first section of the acknowledgements by simply thanking the rest University of Michigan ATLAS group, as well as the whole of the U of M Physics department. Even if not mentioned explicitly by name, the support of the entire community here was widespread and welcomed.

In the broader ATLAS spectrum, over the course of my program I owe much to the Higgs working group, in particular the $H \rightarrow WW$ subgroup, and the guidance of Louis Fayard, Aleandro Nisati, and Ketevi Assamagan; to Takashi Matsushita and Andreas Korn of the low p_T muon performance group; and to the Standard Model working group, specifically the W/Z subgroup, with particular mention to Maarten Boonekamp and Matthias Schott.

Outside of the academics, I also have many people to thank for their presence in my life over the course of my graduate program. I first thank my parents, Mary and David, for always being supportive and encouraging, and my brother Michael for often reminding me that there is more to life than work and that I need to spend a little time on myself. I owe a special mention to my Aunt Lois, for providing a home away from home for the majority of my time at CERN. Further I thank Danielle Ausems, for countless hours spent on the phone, and for being a dear friend whom I could always go to with any of life's problems. I acknowledge the CERN Games Club, and in particular Nir Amram and Herta Richter, for managing to provide a good mix of business with pleasure and friendship with collaboration. The University of Michigan's anime club, Animania, also provided me with many good friends and other outlets for social gathering. This list would not be complete without mention of my lifelong friends. From my undergraduate education, I must thank specifically the fellow members of Wahlstrom Section 202: Zach Armstrong, Nate Haleen, Ben Hardy, Jared Lee, Josh Zimmerman, and all the "honorary" members. I also need to thank the tight-knit Gustavus Physics program. Keeping in touch through yearly reunions has been a wonderful tradition, one that I hope we can keep up indefinately. Further in the past, but no less important are those from my high school days, and from my time in the Boy Scouts. While I've kept in closest contact with Brian Littlefield and Destry Hinck, there were many more of you that helped to shape me into who I am today. Finally, I wish to thank the several online communities which I have been a part of and where I have developed many lasting bonds of friendship over common interests, specifically the folks of the Do You Believe In Mods? thread at Gaiaonline, and the whole of the Serenes Forest forums.

Contents

Chapter

List of Figures

Figure

List of Tables

Table

List of Appendices

Appendix

List of Abbreviations

ATLAS	A Toroidal LHC ApparatuS
LHC	Large Hadron Collider
nb	nanobarn
TeV	tera electron volt
GeV	giga electron volt
SM	Standard Model
EW	Electroweak
QED	Quantum Electrodynamics
GWS	Glashow-Weinberg-Salam
QCD	Quantum Chromodynamics
BR	Branching Ratio
$BR_{\mu\mu}$	Branching Ratio of Z to muons
PDF	Parton Distribution Function
MC	Monte Carlo
IP	Interaction Point
ID	Inner Detector
SCT	Silicon Microstrips
TRT	Transition Radiation Tracker
MET	Missing Transverse Energy
EM	Electromagnetic
LAr	Liquid Argon
FCal	Forward Calorimeter
HEC	Hadronic End-cap Calorimeter
MS	Muon Spectrometer
MDT	Monitored Drift Tube
CSC	Cathode Strip Chamber
RPC	Resitive Plate Chamber
TGC	Thin Gap Chamber
L1	Level 1
L2	Level 2
EF	Event Filter
HLT	High Level Trigger
FSR	Final-State Radiation
AOD	Analysis Object Data
DPD	Derived Physics Data

ROD	Readout Device
MB	Main Dipole Magnet
MQ	Main Quadropole Magnet
BCT	Bunch Current Transformer
DCCT	Direct Current-Current Transformer
ROI	Region of Interest
SA	Standalone
CERN	European Organization for Nuclear Research
SSB	Spontaneous Symmetry Breaking
U(n)	Unitary group of degree n
SU(n)	Special Unitary group of degree n
LEP	Large Electron-Positron Collider
PeV	peta electron volt
CMS	Compact Muon Solenoid
ALICE	A Large Ion Collider Experiment
LHCb	Large Hadron Collider beauty
QDS	Quench Detection Systems
MuCTPI	Muon to Central Trigger Processor Interface
MOORE	Muon Object Oriented REconstruction
MuID	Muon Identification
STACO	STAtistical COmbination
MBTS	Minimum Bias Trigger Scintillator
LUCID	LUminosity measurement using a Cherenkov Integrating Detector
ZDC	Zero Degree Calorimeter
ESD	Event Summary Data
ADC	Analog to Digital Converter
TDC	Time to Digital Converter
dof	degree of freedom
GRL	Good Run List
LO	Leading Order
NLO	Next-to Leading Order
NNLO	Next-to Next-to Leading Order
RMS	root mean square
LBID	Luminosity Block Identification

Abstract

This thesis presents measurements of the inclusive process $pp \to (Z \to \mu^+\mu^-) +$ anything based on 40.2 pb^{-1} of data from LHC collisions with center-of-mass energy of $\sqrt{s} = 7$ TeV as recorded by the ATLAS detector. For events with two isolated muons satisfying transverse momentum $(p_T)_\mu > 20$ GeV, pseudorapidity $|(\eta)_\mu| < 2.4$, and dimuon invariant mass $60 < M_{\mu\mu} < 120$ GeV, the product of the fiducial Z production cross-section and branching ratio to muons was determined to be $(\sigma_Z)_{fid} \times BR_{\mu\mu} = 0.455 \pm 0.017$ nb, in agreement with a Standard Model prediction of 0.447 ± 0.022 nb. Using Monte Carlo programs this result was extrapolated to yield a result for the total Z production cross-section, $(\sigma_Z)_{tot} \times BR_{\mu\mu} = 0.943 \pm 0.041$ nb.

Normalized distributions for the transverse momentum and rapidity of $Z/\gamma^* \to \mu^+\mu^-$ muon pairs were also measured and found to be in good agreement with theory modeled by the PYTHIA Monte Carlo program.

Chapter 1

Introduction

This thesis presents measurements of the inclusive process $pp \to (Z \to \mu^+\mu^-) +$ anything at a center-of-mass energy of $\sqrt{s} = 7$ TeV with the ATLAS detector at the CERN Large Hadron Collider (LHC). These measurements, based on an integrated luminosity of 40237 nb^{-1}, include a determination of the cross-section of Z boson production with subsequent decay to muons. For the product of the cross-section and branching ratio ($\sigma_Z \times BR_{\mu\mu}$) the dimuon mass spectrum was analyzed using fitting techniques to extract a Z boson signal, excluding contributions from photon (γ^*) mediation and Z-photon interference effects. Normalized transverse momentum and rapidity distributions are also presented for $\mu^+\mu^-$ pairs with a dimuon invariant mass in the range $66 < M_{\mu\mu} < 116$ GeV. For these distributions ($\frac{1}{\sigma}\frac{d\sigma}{dp_T}$ and $\frac{1}{\sigma}\frac{d\sigma}{dY}$), however, the measurements included all Z/γ^* contributions.

This thesis begins with an introduction to the Standard Model of particle physics in Chapter 2. Specific emphasis is placed on those aspects most relevant to the production and decay of Z bosons. Chapter 3 describes the layout and construction of the LHC, the particle accelerator that produced the proton-proton collisions. The focus of Chapter 4 is the ATLAS detector and its many specialized subsystems. Chapter 5 introduces the Monte Carlo event generation and detector simulation programs. These programs are necessary to provide samples with which to compare the data to predictions from theory. Chapters 6 and 7 outline the measurements of the Z production cross-section and the normalized transverse momentum and rapidity distributions, respectively. Detailed comparisons are made with Monte Carlo theory predictions and also with other published ATLAS analyses. Chapter 8 summarizes all of the results, while supplementary material is located in the Appendices.

Chapter 2

Theory

The Standard Model of particle physics (SM) is a theory that describes subatomic phenomena on the fundamental level, and does so with great success. This theory defines the basic building blocks of matter, the forces that govern their interactions, and the quantum field theories that tie them together. The SM is known to be incomplete, and there are other theories that aim to extend it, such as supersymmetry. However, the scope of this thesis focuses entirely on SM processes. In particular, our study will concentrate on those processes in the electroweak (EW) sector related to Z bosons.

2.1 Fundamental Particles and Forces

There are 12 fundamental spin $\frac{1}{2}$ fermions (and corresponding antiparticles) that are divided into two classes: quarks and leptons. These are further split into three families, or generations, and a summary of the particles and basic properties is displayed in Table 2.1. The only apparent difference between the fermion generations lies in the masses of the particles. These fermions are the basic constituents of matter.

These particles interact via four different fundamental forces characterized by dif-

Table 2.1: Fundamental fermions of the Standard Model. Charge is given in multiples of the magnitude of electron charge.

	Quarks		Leptons	
Charge	+2/3	-1/3	-1	0
Generation 1	u	d	e	ν_e
Generation 2	c	s	μ	ν_μ
Generation 3	t	b	τ	ν_τ

ferent strengths. On the subatomic scale they are ordered from weakest to strongest: gravity, the weak force, electromagnetism, and the strong force. Not only do they differ in the magnitude of their effects, but the four forces also act on differing particle properties. Furthermore, each force is mediated by one or more force-carrying bosons. A summary of these interactions and associated particles is found in Table 2.2. However, it should be noted that electromagnetism and the weak force are not *actually* independent forces, rather they have been shown to be different aspects of a unified electroweak force. They appear as distinctly different forces as a result of a spontaneously broken symmetry. This Spontaneous Symmetry Breaking (SSB) is responsible for giving mass to the mediating W and Z bosons (while the other mediating bosons remain massless). On the scales involved in particle physics, gravity is so weak that its effect can be neglected, and a theory of gravity does not enter into the SM.

Table 2.2: Fundamental forces of the Standard Model.

Force	Acts on	Mediated by
Weak	quarks, leptons, electroweak bosons	$W^{\pm}$, Z^0
Electromagnetism	electrically charged particles	photon (γ)
Strong	particles with color charge	gluons (g)

2.2 Lagrangians and Gauge Invariance

The theories that tie the fundamental particles and the fundamental forces together are quantum field theories, which rely heavily on the notions of symmetries and gauge invariance [1] [2]. Electromagnetism taken alone can be described by Quantum Electrodynamics (QED) and is connected to the Unitary group U(1). When unified with the weak force by the Glashow-Weinberg-Salam (GWS) formalism, this group is extended to a combination of a Special Unitary group, SU(2), with a U(1) group. The strong interaction is governed by Quantum Chromodynamics (QCD) which operates within the framework of a SU(3) group. The full Standard Model can then be described as a theory of $\mathrm{SU}(3)_C \otimes \mathrm{SU}(2)_L \otimes \mathrm{U}(1)_Y$, where C refers to color charge, Y to hypercharge, and L to left-handed fermions.

In particle physics, theories are based on Lagrangians, with the particles and the forces expressed in terms of quantum fields. These Lagrangians are required to be invariant under Lorentz transformation and transformations associated with the U(n) and SU(n) groups (such as local phase invariance). This requirement of the invariance of the Lagrangian introduces the gauge boson fields and their transformations, along with what is called the covariant derivative.

2.3 Quantum Electrodynamics

Considering QED as a standalone theory, for the moment, will provide an instructive demonstration of the principles and method involved. Consider the following local phase transformation:

$$\psi(x) \to \psi'(x) \equiv e^{i\alpha(x)}\psi(x). \tag{2.1}$$

A Lagrangian of the form

$$\mathcal{L} = i\bar{\psi}(x)\gamma^{\mu}\partial_{\mu}\psi(x) + \cdots , \tag{2.2}$$

is not invariant under local phase transformations since the existence of the derivative will bring about an additional term due to the spatial dependence of the phase rotation α. By changing the definition of the derivative to the *covariant derivative* as follows

$$\mathcal{D}_{\mu} \equiv \partial_{\mu} + ieA_{\mu}(x), \tag{2.3}$$

and by requiring that $A(x)$ transforms under the local phase transformation as

$$A_{\mu}(x) \to A'_{\mu}(x) \equiv A_{\mu}(x) - \frac{1}{e}\partial_{\mu}\alpha(x), \tag{2.4}$$

the resulting Lagrangian possesses the desired invariance and, furthermore, contains the expected interaction term between the fermion field and the gauge field.

2.4 Electroweak Theory

As mentioned earlier, the GWS approach proposes that the Lagrangian for the EW sector is based on $\mathrm{SU}(2)_L \otimes \mathrm{U}(1)_Y$. This choice was motivated by observation that the weak charged currents only couple to left-handed chiralities, and that this coupling involves doublets of fermions. Further, it was apparent from quark decays that the mass eigenstates differ from the weak eigenstates. While recent experiments have shown that neutrinos also undergo mixing, and have masses, in the SM the three neutrinos are considered to be massless [3] [4].

Considering only the first generation, for the moment, we identify the following fermion fields:

$$\psi_1(x) = \begin{pmatrix} u \\ d' \end{pmatrix}_L, \psi_2(x) = u_R, \psi_3(x) = d'_R. \tag{2.5}$$

where the prime indicates the weak eigenstate of the down-type quarks. Equivalently for the leptons:

$$\psi_1(x) = \begin{pmatrix} \nu_e \\ e \end{pmatrix}_L, \psi_3(x) = e_R, \tag{2.6}$$

(right-handed neutrinos do not enter into the SM). The $\psi_1(x)$ are the left-handed SU(2) weak isospin doublets that partake in the weak interaction while $\psi_2(x)$ and $\psi_3(x)$ are right-handed SU(2) singlets that do not. All three $\psi(x)$ are affected by the U(1) symmetry, however, and that leads to the combined field transformations required by local gauge invariance to be:

$$\psi_1(x) \to \psi'_1(x) \equiv e^{iY_1\beta(x)} e^{iT^a\alpha^a(x)}\psi_1(x) \tag{2.7}$$

$$\psi_2(x) \to \psi'_2(x) \equiv e^{iY_2\beta(x)}\psi_2(x) \tag{2.8}$$

$$\psi_3(x) \to \psi'_3(x) \equiv e^{iY_3\beta(x)}\psi_3(x) \tag{2.9}$$

where $a = 1, 2, 3$ and T^a are the three SU(2) generator matrices.

The three $\alpha^a(x)$ give rise to three gauge fields (W^1, W^2, W^3), and the $\beta(x)$ introduces one more field (B^0). The Y_i are identified with the charge of the U(1) group, called *hypercharge*. The appropriate covariant derivative then is, for $\psi_1(x)$:

$$\mathcal{D}_\mu \equiv \partial_\mu + ig\mathbf{T} \cdot \mathbf{W}_\mu(x) + ig'Y_1B_\mu(x), \tag{2.10}$$

and similarly for $\psi_2(x)$ and $\psi_3(x)$, omitting the SU(2) term and changing the index on Y_i.

This definition for the covariant derivative also fixes the transformation of the gauge fields as follows:

$$B_\mu(x) \to B'_\mu(x) \equiv B_\mu(x) - \frac{1}{g'}\partial_\mu\beta(x) \tag{2.11}$$

$$\tilde{W}_\mu \to \tilde{W}'_\mu \equiv U_L(x)\tilde{W}_\mu U_L^\dagger(x) + \frac{i}{g}\partial_\mu U_L(x)U_L^\dagger(x) \tag{2.12}$$

where $\tilde{W}_\mu \equiv \mathbf{T} \cdot \mathbf{W}_\mu(x)$ and $U_L(x) \equiv e^{iT^a\alpha^a(x)}$.

The full electroweak Lagrangian is then:

$$\mathcal{L} = \sum_{j=1}^{3} i\bar{\psi}_j(x)\gamma^\mu \mathcal{D}_\mu \psi_j(x) - \frac{1}{4}B_{\mu\nu}B^{\mu\nu} - \frac{1}{4}W^i_{\mu\nu}W^{\mu\nu}_i, \tag{2.13}$$

where $B_{\mu\nu} \equiv \partial_\mu B_\nu - \partial_\nu B_\mu$ and $W^i_{\mu\nu} \equiv \partial_\mu W^i_\nu - \partial_\nu W^i_\mu - g\epsilon^{ijk}W^j_\mu W^k_\nu$.

The existence of quadratic terms in the W field strength gives rise to self-coupling of the weak bosons. However, at this stage, the gauge fields in the Lagrangian still do not correspond to the observed particles. Rather, these fields mix together to form the observed fields, with W^1 and W^2 producing the observed charged fields W^+ and W^-, while W^3 and B^0 mix to form the neutral fields Z^0 and the photon (γ). These mixings are $W_\mu \equiv (W^1_\mu + iW^2_\mu)/\sqrt{2}$ and $W^\dagger_\mu \equiv (W^1_\mu - iW^2_\mu)/\sqrt{2}$ for the charged fields, and $Z_\mu \equiv \cos\theta_W W^3_\mu - \sin\theta_W B_\mu$ and $A_\mu \equiv \sin\theta_W W^3_\mu + \cos\theta_W B_\mu$ for the neutral fields.

The Lagrangian can be rewritten in terms of these new fields. Concentrating only on the section of the Lagrangian connected to the neutral bosons, this results in:

$$\bar{\psi}_j\gamma^\mu[A_\mu(gT_3\sin\theta_W + g'Y_j\cos\theta_W) + Z_\mu(gT_3\cos\theta_W - g'Y_j\sin\theta_W)]\psi_j. \tag{2.14}$$

By associating the field A_μ with QED, we obtain $g\sin\theta_W = g'\cos\theta_W$ and $Y = Q - T_3$, giving us relations between the gauge coupling strengths, and defining electrical charge as a combination of hypercharge and the third component of weak isospin.

However, there is still a problem. Adding explicit mass terms to the Lagrangian spoils the gauge invariance, and so the particles associated with these fields should all be expected to be massless, which is in contradiction with observation. Not only is this the case for the gauge bosons, but also for the fermions, as adding their mass terms would spoil the separation of chiralities. A solution to this problem is the subject of the following section.

2.5 Higgs and Spontaneous Symmetry Breaking

In the previous section a Lagrangian was derived that explained the EW interactions well, save for one key aspect: particle masses. The W and Z bosons are forbidden to have mass due to gauge invariance, and fermion masses violate symmetry considerations. This flies in the face of experiment, however, where we observe that particles are massive.

The SM solves this problem through the so-called Higgs Mechanism [5]. This mechanism is based on SSB and posits a universal scalar field that has degenerate ground states with non-zero expectation value. Settling into one or the other of these will result in a broken symmetry that generates masses for the particles.

A complex scalar field

$$\phi(x) \equiv \begin{pmatrix} \phi^+(x) \\ \phi^0(x) \end{pmatrix} \tag{2.15}$$

is added to the Lagrangian resulting in the following new terms

$$\mathcal{L}_S = (\mathcal{D}_\mu \phi)^\dagger \mathcal{D}^\mu \phi - \mu^2 \phi^\dagger \phi - h(\phi^\dagger \phi)^2. \tag{2.16}$$

Requiring that $h > 0$ and that $\mu^2 < 0$ yields a stable ground state with non-zero expectation value for the scalar field.

We reparameterize by expanding around the vacuum state so that

$$\phi(x) = \frac{1}{\sqrt{2}} \begin{pmatrix} 0 \\ v + H(x) \end{pmatrix}, \tag{2.17}$$

where v is the vacuum expectation value ($v = 246$ GeV) and $H(x)$ is a real field. (The more general form would include a $e^{iT^a \alpha^a(x)}$ term, but by the gauge symmetry we can rotate that away.) Substituting this representation into the Lagrangian results in the following:

$$(\mathcal{D}_\mu \phi)^\dagger \mathcal{D}^\mu \phi \to \frac{1}{2}\partial_\mu H \partial^\mu H + (v + H)^2 [\frac{g^2}{4} W_\mu^\dagger W^\mu + \frac{g^2}{8\cos^2\theta_W} Z_\mu Z^\mu]. \tag{2.18}$$

This development has led directly to mass terms for the W and Z bosons, $M_Z \cos\theta_W = M_W = \frac{1}{2} v g$. The scalar H field also persists and acquires a mass term, and it is this that is referred to as the Higgs boson.

Further, the problem of fermion masses is also solved by this mechanism. Using the first family of leptons as an example, adding the following interaction term to the Lagrangian

$$g_e(\bar{\psi}_1 \phi \psi_3 + \phi^\dagger \bar{\psi}_3 \psi_1) \tag{2.19}$$

(using the notation given in Equation 2.6) will give rise to mass terms for the electron, as well as an interaction with the Higgs field, both of which come with the arbitrary coupling g_e.

2.6 Quantum Chromodynamics

QCD is based on the gauge group SU(3)$_C$. The C refers the SU(3) color charge, and the strong force only operates on colored objects. There are three different colors: red, green, and blue. Isolated colored particles have never been observed, leading to the *confinement hypothesis*, which states that observed particles involve either a combination of color-anticolor or of all three colors. Requiring local gauge invariance of the Lagrangian, the algebra of the SU(3) group gives rise to eight gauge bosons, called gluons. As was the case with EW, the anticommutivity of SU(3) gives rise to self-interaction terms for the gauge bosons. While QCD and the strong force are a rich field of study and full of many interesting physics topics, for the purpose of this thesis, they will only play a small role. A more in-depth discussion can be found in [6], while for current considerations QCD simply provides the main method by which the Z boson can be produced with non-zero transverse momentum. In the tree-level production diagram, Figure 2.1, the Z is produced alone in the final state and has no transverse momentum. It is through additional diagrams, shown in Figure 2.2, where the Z is produced in association with jets (either quark jets or gluon jets) that it has appreciable p_T.

2.7 Z Boson

Several important results were derived in the previous sections that are directly relevant to Z boson physics. First, since the Z boson field is a combination of W_μ^3 and B_μ, it only operates on diagonal elements of SU(2) and thus cannot participate in flavor-changing processes. Additionally, the coupling strength of the Z interaction vertex depends on the properties of the fermion involved. With these facts in mind, we discuss Z boson production and Z boson decay.

While Z boson production can occur in a number of different ways, the main process in proton-proton collisions is through what is called *Drell-Yan*, where a quark in one proton annihilates with a same flavor anti-quark from the sea of the other proton. The Feynman diagram for such a process is shown in Figure 2.1.

However, there are other higher-order diagrams that also contribute. Some of the higher-order effects include processes which produce gluons or quarks in addition to the Z, shown in Figure 2.2. In these cases these final-state gluons or quarks will hadronize into jets that will accompany the signature of the Z decay. Another type of higher-order process deals with radiative effects, such as bremsstrahlung of photons.

Examples of such diagrams are seen in Figure 2.3.

The properties of the Z are well measured, yielding a mass of 91.1876 GeV and a full width of 2.4952 GeV [7]. Additionally its partial widths (decays to specific channels) and branching ratios (partial width / full width) are known; the relevant branching ratio for Z decaying to muons is 3.366%. A summary of its important properties are found in Table 2.3. Z decays to $t\bar{t}$ are kinematically forbidden.

Table 2.3: Z boson properties [7].

Property	Value
Charge	0
Mass	91.1876 ± 0.0021 GeV
Full Width Γ	2.4952 ± 0.0023 GeV
$\Gamma(e^+e^-)/\Gamma$	$3.363 \pm 0.004\%$
$\Gamma(\mu^+\mu^-)/\Gamma$	$3.366 \pm 0.007\%$
$\Gamma(\tau^+\tau^-)/\Gamma$	$3.370 \pm 0.008\%$
$\Gamma(invisible)/\Gamma$	$20.00 \pm 0.06\%$
$\Gamma(u\bar{u} + c\bar{c})/2\Gamma$	$11.6 \pm 0.6\%$
$\Gamma(d\bar{d} + s\bar{s} + b\bar{b})/3\Gamma$	$15.6 \pm 0.4\%$

Z decay branching ratios can be derived from the interaction term in the Lagrangian. From Equation 2.14 this term can be expressed as

$$\frac{g}{\cos\theta_W}[T_3 - \sin^2\theta_W Q]\bar{\psi}Z_\mu\psi. \tag{2.20}$$

The branching ratio (BR) to a particular fermion pair is then given approximately by

$$BR(Z \to f\bar{f}) \approx \frac{\sum\limits_{c}(T_{3,f} - \sin^2\theta_W Q_f)^2}{\sum\limits_{c,g,f}(T_{3,f} - \sin^2\theta_W Q_f)^2} \tag{2.21}$$

where summation indices run over color (c), generation (g), and flavor (f), and where the kinematic effect of the fermion masses has been neglected. This is a reasonable approximation given that $M_Z \gg m_f$. For this thesis since the branching ratio of Z to muons is referred to frequently, the shorthand $BR_{\mu\mu}$ will be employed. Table 2.4 lists the fermions, their associated isospin, charge, hypercharge, and the theoretical and measured branching ratios. In the calculations used to arrive at the theoretical values in Table 2.4 a value of $\sin^2\theta_W = 0.23152$ was used [7]. Measured branching ratios to u, d, and s quarks are inferred from measurement of the combined decay modes for up- or down-type quarks while branching ratios to neutrinos are assumed

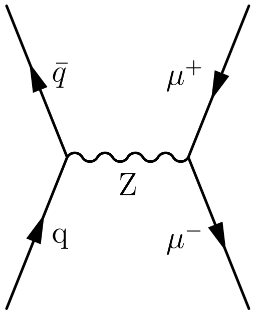

Figure 2.1: Drell-Yan production of the Z.

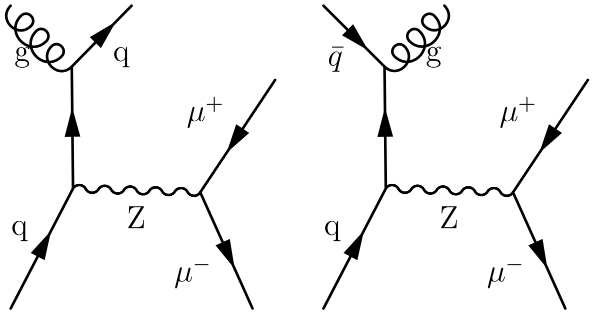

Figure 2.2: Z production with a quark or gluon in final state.

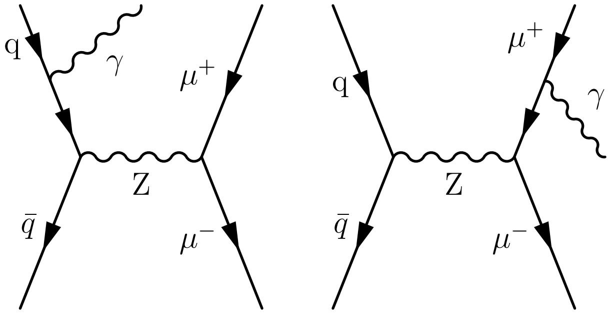

Figure 2.3: Z production with initial and final-state radiation.

to contribute equally to the “invisible” decays which constitute $20.00 \pm 0.06\%$ of all Z decays.

2.8 Muon Pair Production

We detect Z bosons through their decay to $\mu^+\mu^-$ pairs. However, muon pairs can also be produced by photon-mediated quark-antiquark annihilation and by interference of the Z and photon amplitudes indicated in Figure 2.4.

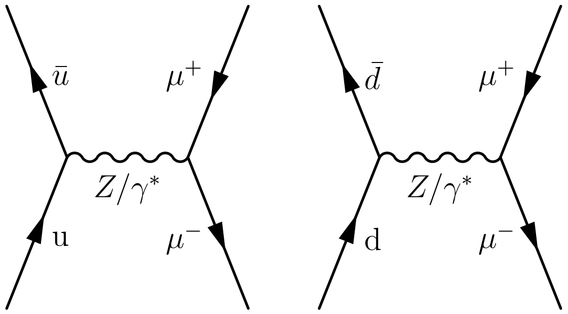

Figure 2.4: Muon pair production through mediation of both Z bosons and photons. (The γ^* notation indicates that the photon is produced off the mass shell.) The two processes also produce an interference term.

The total cross-section for the production of muon pairs can therefore be written as

$$\sigma(s) = \sigma_Z(s) + \sigma_\gamma(s) + \sigma_{\gamma Z}(s) \tag{2.22}$$

with dependence on $s = M^2$ where M is the invariant mass of the muon pair. Following reference [8], expressions for the individual contributions to the muon-pair production cross-section are:

$$\sigma_Z(s) = k_1 \frac{s}{|s - s_Z|^2} \tag{2.23}$$

$$\sigma_\gamma(s) = k_2 \frac{1}{s} \tag{2.24}$$

$$\sigma_{\gamma Z}(s) = k_3 \frac{s - M_Z^2}{|s - s_Z|^2} \tag{2.25}$$

where $s_Z = M_Z^2 - iM_Z\Gamma_Z$, with M_Z the mass of the Z and Γ_Z the width of the Z. For up and down quarks of a particular color, and to lowest order, we give values for k_1, k_2, and k_3 in Table 2.5 as computed using reference [8].

Table 2.4: A summary of fermion electroweak properties. This covers weak isospin, hypercharge, charge, and the Z decay branching ratios [7].

Fermion	T_3	Q	Y	Theoretical BR	Measured BR
u_L	$\frac{1}{2}$	$\frac{2}{3}$	$\frac{1}{6}$	11.8%	11.6%
u_R	0	$\frac{2}{3}$	$\frac{2}{3}$		
d_L	-$\frac{1}{2}$	-$\frac{1}{3}$	$\frac{1}{6}$	15.2%	15.6%
d_R	0	-$\frac{1}{3}$	-$\frac{1}{3}$		
ν_{eL}	$\frac{1}{2}$	0	-$\frac{1}{2}$	6.9%	6.67%
ν_{eR}	0	0	0	0%	0%
e_L	-$\frac{1}{2}$	-1	-$\frac{1}{2}$	3.4%	3.36%
e_R	0	-1	-1		
c_L	$\frac{1}{2}$	$\frac{2}{3}$	$\frac{1}{6}$	11.8%	12.0%
c_R	0	$\frac{2}{3}$	$\frac{2}{3}$		
s_L	-$\frac{1}{2}$	-$\frac{1}{3}$	$\frac{1}{6}$	15.2%	15.6%
s_R	0	-$\frac{1}{3}$	-$\frac{1}{3}$		
$\nu_{\mu L}$	$\frac{1}{2}$	0	-$\frac{1}{2}$	6.9%	6.67%
$\nu_{\mu R}$	0	0	0	0%	0%
μ_L	-$\frac{1}{2}$	-1	-$\frac{1}{2}$	3.4%	3.37%
μ_R	0	-1	-1		
t_L	$\frac{1}{2}$	$\frac{2}{3}$	$\frac{1}{6}$	NA	NA
t_R	0	$\frac{2}{3}$	$\frac{2}{3}$		
b_L	-$\frac{1}{2}$	-$\frac{1}{3}$	$\frac{1}{6}$	15.2%	15.1%
b_R	0	-$\frac{1}{3}$	-$\frac{1}{3}$		
$\nu_{\tau L}$	$\frac{1}{2}$	0	-$\frac{1}{2}$	6.9%	6.67%
$\nu_{\tau R}$	0	0	0	0%	0%
τ_L	-$\frac{1}{2}$	-1	-$\frac{1}{2}$	3.4%	3.37%
τ_R	0	-1	-1		

Table 2.5: Values of the constants in Equations 2.23–2.25.

	k_1	k_2	k_3
u	3.60×10^{-5}	1.14×10^{-4}	3.44×10^{-6}
d	4.64×10^{-5}	2.84×10^{-5}	3.10×10^{-6}

At the peak of the Z resonance ($s = M_Z^2$),

$$\frac{\sigma_\gamma}{\sigma_Z} = \frac{k_2}{k_1}\frac{\Gamma_Z^2}{M_Z^2} = 7.38 \times 10^{-4}\frac{k_2}{k_1}$$

and the interference term $\sigma_{\gamma Z}(M_Z^2) = 0$ as it undergoes a change in sign from negative (for $s < M_Z^2$) to positive (for $s > M_Z^2$).

In our analysis we extract a Z signal over an extended range in $\sqrt{s} = M$. We can estimate the relative contributions of σ_Z, σ_γ, and $\sigma_{\gamma Z}$ by integrating Equations 2.23–2.25 over this range in $\sqrt{s}$. We find that $\frac{\int \sigma_\gamma dM}{\int \sigma_Z dM} \approx$ a few percent, indicating photon effects will be significant enough to enter into the data analysis. Table 2.6 gives the values for this ratio for different quark configurations. We note that protons contain two valence up quarks and one valence down quark.

Table 2.6: Ratios of the γ and Z contributions to the cross-section. The range of integration is $60 < M < 120$ GeV and three input scenarios are presented.

	u	**d**	**(2u+d)/3**
$\frac{\int \sigma_\gamma dM}{\int \sigma_Z dM}$	4.30%	0.83%	2.94%

The contribution of $\int \sigma_{\gamma Z} dM$ is down by another two orders of magnitude from the γ contribution, and will be neglected given the overall level of uncertainty of the measurements presented in this thesis.

2.9 Parton Distribution Functions

The LHC collides two proton beams. How does colliding protons on protons lead to the sorts of production diagrams shown earlier in the chapter? The answer lies in the parton model. The proton is not only made up of three valence quarks (uud), but also contains virtual quark-antiquark pairs (called *sea quarks*) as well as gluons.

The parton model of the proton operates by assuming that the proton is composed of a collection of point-like particles, called partons, with each individual parton (specifically a quark, anti-quark, or gluon) carrying some fraction x_i of the proton's overall momentum. In a collision between two protons, one can then consider the event to actually be a collision between two partons, one from each proton, with the rest of the partons going on to form the underlying event. The effective mass of the two partons is $M = \sqrt{x_1 x_2 s}$, where s is the square of the proton-proton center of mass energy. The rapidity of the di-parton state is $y = \frac{1}{2}\ln\frac{x_1}{x_2}$.

The computation of proton-proton collision cross-sections relies on structure functions that describe the parton densities as a function of x. Such functions are not calculable from first principles, and instead have to be derived from experiment, relying on data obtained from deep-inelastic scattering and other processes. As indicated in the previous paragraph, if the two partons form a Z boson, then the rapidity distribution of the Z will be sensitive to the parton densities in the protons.

Groups of physicists work with the accumulated data from various particle physics experiments to provide up-to-date structure functions, also known as *parton distribution functions* (PDFs) [9] [10]. One such PDF set is shown in Figure 2.5.

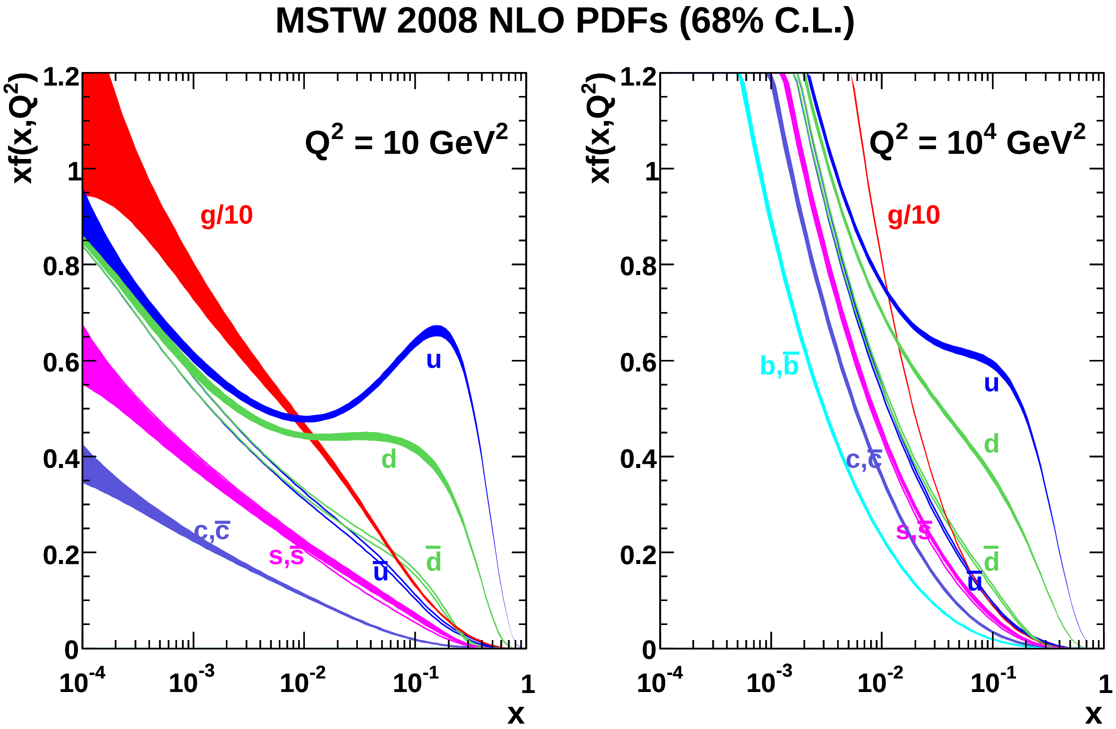

Figure 2.5: Example of parton distribution functions. These are from the 2008 NLO MSTW PDF set [10].

2.10 Motivation for Studying the Z Boson

Studying Z production at the LHC is important for a number of reasons. First and foremost is that the LHC explores a new energy scale, not yet probed by previous experiments, as well as a new production mode (proton-proton collisions rather than proton-antiproton or positron-electron collisions). Since the properties of the Z are very well understood from previous experiments, measuring them again at the LHC and checking for consistency is vital, as discrepancies could indicate deficiencies in the current PDF models, or the Monte Carlo generators. To go forward and engage in searches for new physics, such as the Higgs or supersymmetry, we first want to have confidence in the tools we are using to undertake such searches. We can gain that by studying the Z boson.

Chapter 3

The LHC

The Large Hadron Collider (LHC) is an accelerator and collider designed to produce proton-proton collisions at 14 TeV and also lead ion collisions at 1.15 PeV [11]. For reasons discussed in Section 3.4 the 2010 running period, providing the data used in this thesis, had proton-proton collisions at 7 TeV. The LHC is installed in the 26.7 km circumference LEP tunnel which is located 50 to 175 m below ground, having been constructed with a slope of 1.4% in accordance with the local geography and geology [12]. The diameter of the tunnel is approximately 3.8 m, and it consists of eight arced segments as well as the eight straight sections which house the beam interaction points (IPs). The LHC accommodates four main experiments, each one located at one of these IPs. Figure 3.1 provides a diagram of the LHC, outlining the location of the experiments and services.

The LHC makes use of the existing accelerator complexes already present from past CERN experiments to provide the initial acceleration and injection. Figure 3.2 details the layout of these initial-stage accelerators through which the proton beams pass before being injected into the main LHC ring. Since the LHC is designed for collisions of protons or nuclei with the same charge, the two beams rotate in opposite directions around the ring and require separate magnetic fields and vacuum chambers, except at the IPs where they share a common segment. In these common segments special adjustments are made either to avoid unwanted collisions or to collide the beams at a certain crossing angle, the value of which depends on the experiment.

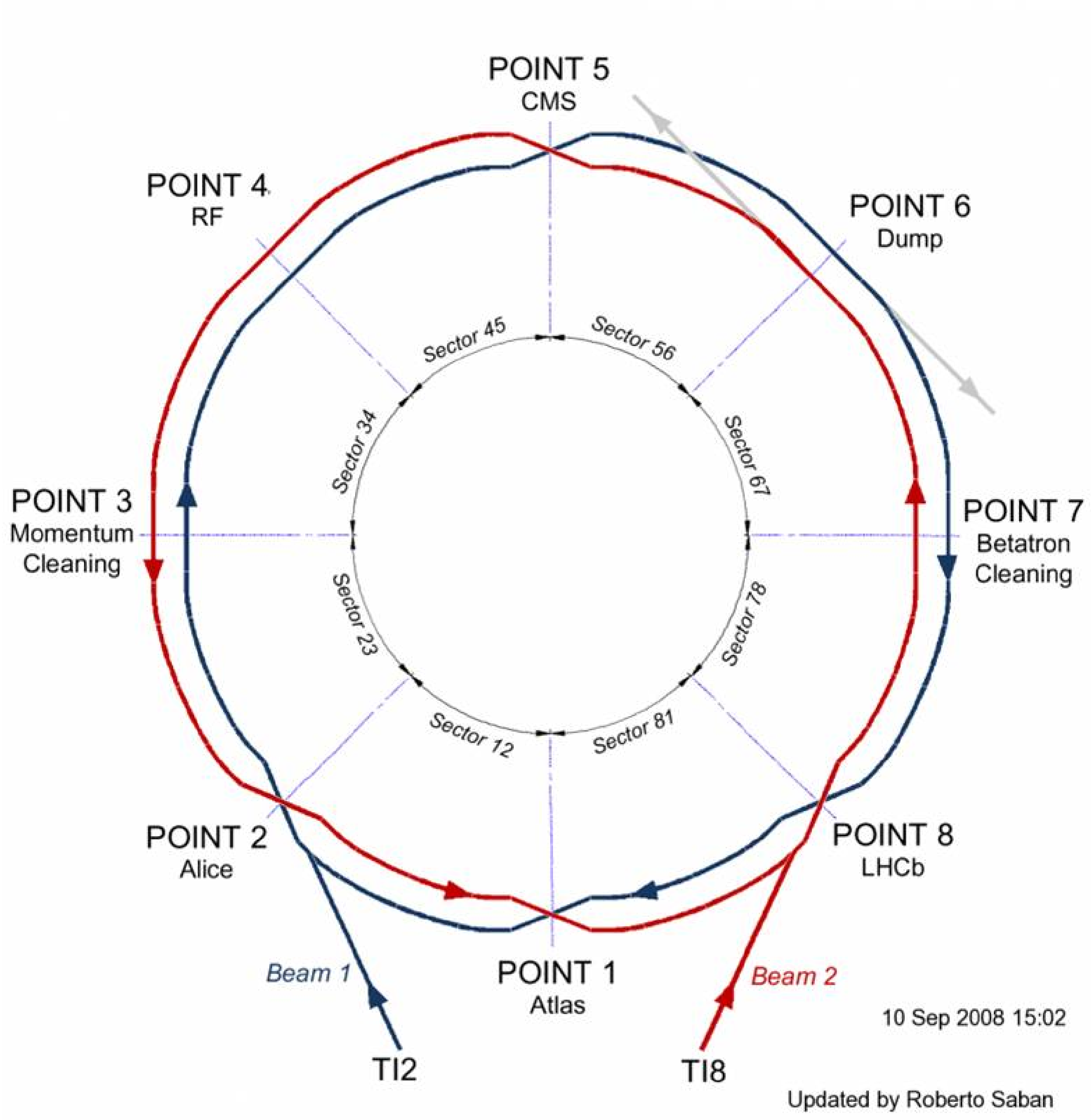

Figure 3.1: Diagram of the LHC ring with the standard naming conventions. Note the two injection lines (TI2, TI8) for the counter-rotating beams, as well as the positions of the four main experiments: ATLAS (IP1), ALICE (IP2), CMS (IP5), and LHCb (IP8) [13].

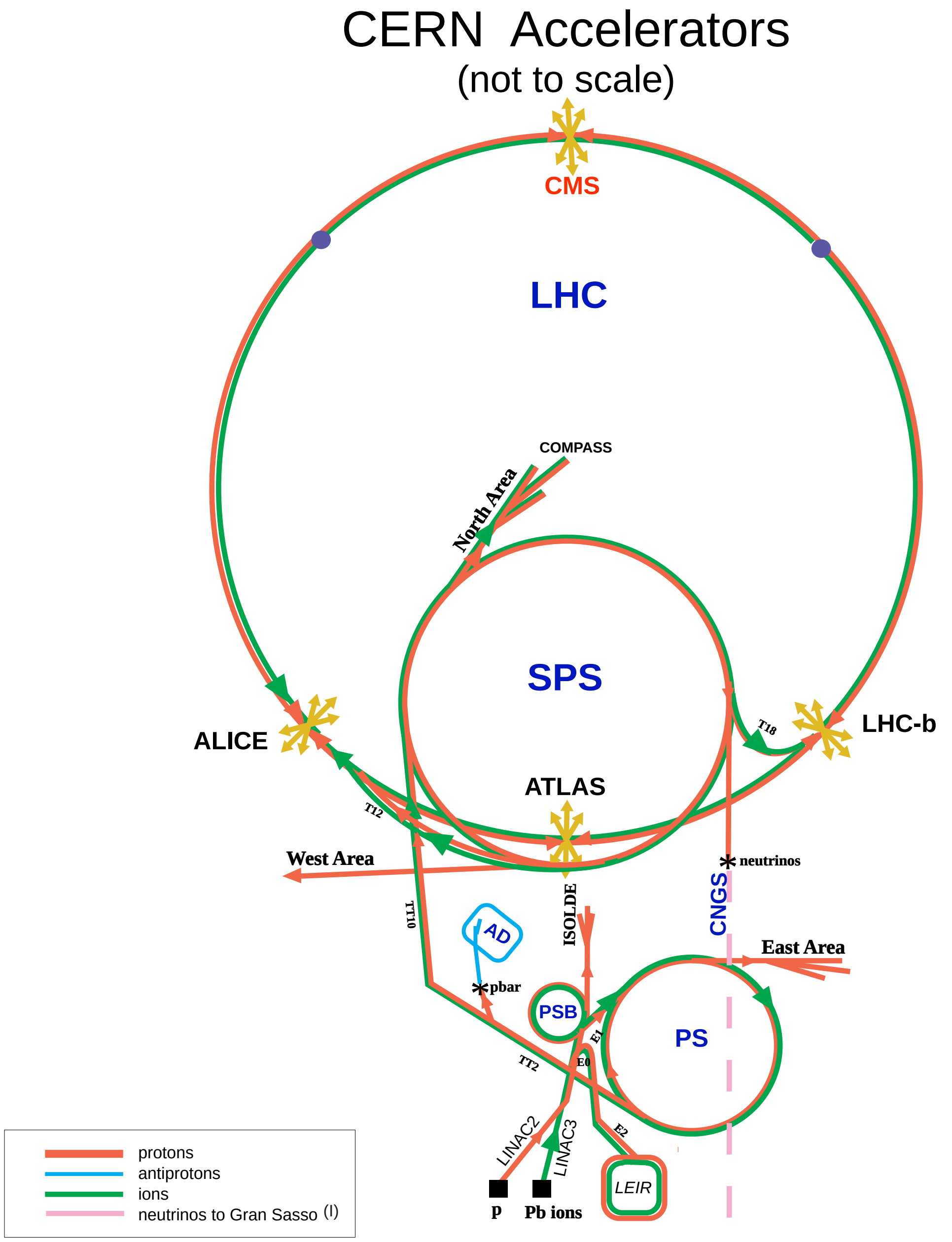

LHC: Large Hadron Collider
SPS: Super Proton Synchrotron
AD: Antiproton Decelerator
ISOLDE: Isotope Separator OnLine DEvice
PSB: Proton Synchrotron Booster
PS: Proton Synchrotron
LINAC: LINear ACcelerator
LEIR: Low Energy Ion Ring
CNGS: Cern Neutrinos to Gran Sasso

Rudolf LEY, PS Division, CERN, 02.09.96
Revised and adapted by Antonella Del Rosso, ETT Div.,
in collaboration with B. Desforges, SL Div., and
D. Manglunki, PS Div. CERN, 23.05.01

Figure 3.2: Schematic diagram of the CERN accelerator complex [14].

3.1 Magnets

To keep the beam particles in their orbit along the ring, as well as to guide and focus the beams and manage their collisions, the LHC employs a large number of magnets, including both normal and superconducting varieties. There are 1232 main dipole magnets (MB) designed to produce magnetic fields of 8.33 T, 392 main quadrupole magnets (MQ), as well as thousands of corrector magnets [11]. The superconducting magnets are designed to operate at 1.9 K, and are cooled to this temperature by a superfluid helium bath. At nominal operation, the MB magnets have a temperature margin of approximately 1.5 K, while for the MQ magnets this is approximately 2.2 K. If the difference in temperature between the magnet and the helium bath exceeds this margin, the magnet will lose superconductivity, which is referred to as a *quench*. Figure 3.3 provides an illustration of the cross section of one of the MB magnets.

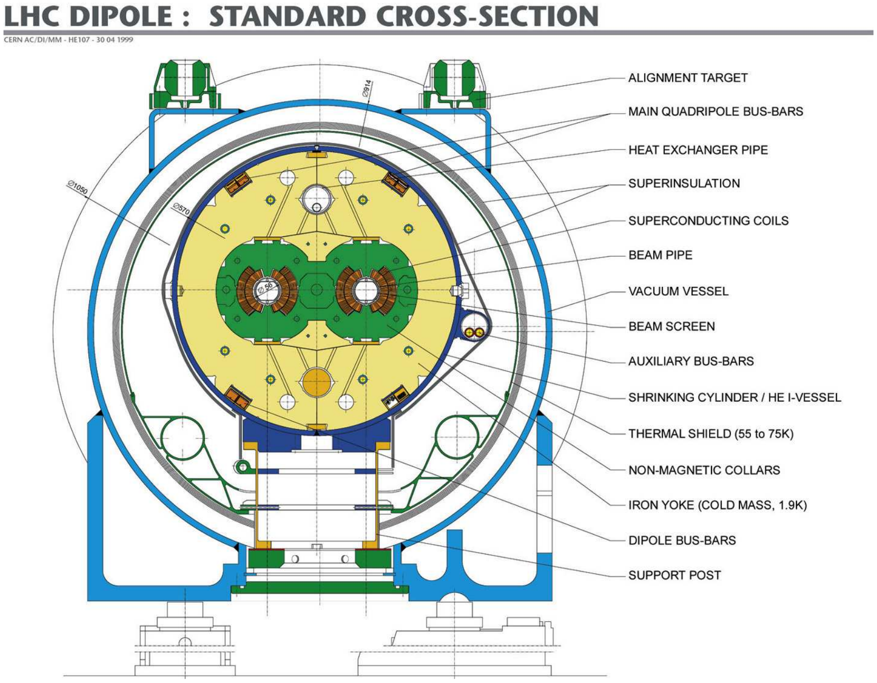

Figure 3.3: LHC superconducting dipole magnet [15].

3.2 LHC Interaction Points

Referring back to Figure 3.1, the LHC is divided into eight sections, each with its own unique purpose. A brief summary of each is provided here. Four of these sections are for housing the main LHC experiments, while the other four sections perform important operational tasks. ATLAS and CMS, located at IP1 and IP5 respectively, are the two general purpose detectors dedicated to searches for possible new physics, including the Higgs Boson and supersymmetry. The ATLAS detector will be described in much greater detail in the next chapter. The other main LHC experiments are at IP2 and IP8, and are more focused experiments. Respectively, they are ALICE which studies mainly, though not exclusively, the lead ion collisions that are a part of the LHC program [16], and LHCb which is designed to detect and record the various decays of B mesons and baryons [17].

The sections not associated with particular experiments are dedicated to specific LHC machine operations. IP4 contains the RF system, which operates at a frequency of 400 MHz and is responsible for capturing the injected beam and accelerating it up to its final energies [11]. IP3 and IP7 are responsible for the momentum and betatron cleaning, respectively, which ensure the high quality of the beams for physics collisions and minimize beam losses into the surrounding material. Excessive beam losses could lead to magnet quenches. Finally, IP6 houses the beam dumping system, which deals with the disposal of the circulating beams, both for planned dumps at the successful end of a luminosity run, as well as for dumps that may arise due to equipment failure.

3.3 Luminosity

The LHC luminosity can be determined with a general-purpose detector using the fundamental relation

$$L = \frac{R_{inel}}{\sigma_{inel}} = \frac{\mu n_b f_r}{\sigma_{inel}} \tag{3.1}$$

where R_{inel} is the rate of inelastic collisions, μ is the number of inelastic interactions per bunch crossing, n_b is the number of bunch crossings, f_r is the revolution frequency, and σ_{inel} is the inelastic cross section [18]. Use of this relation requires prior knowledge of σ_{inel}.

An independent method for measuring the LHC luminosity is based on the method of *van der Meer scans* [19]. Such scans involve shifting one of the two beams with respect to the other and observing the resulting counting rate versus displacement. In this case, the equation for luminosity is expressed entirely in terms of the beam parameters as

$$L = \frac{N_1 N_2 n_b f_r}{2\pi \Sigma_x \Sigma_y} \tag{3.2}$$

where N_i is the number of particles per bunch in beam i, n_b the number of bunches per beam, f_r the revolution frequency, and Σ_i are measures of the size of the beam profiles in the vertical (y) and horizontal (x) directions [18]. The N_i are measured with two complementary LHC systems, fast bunch-current transformers (BCT) and direct current-current transformers (DCCT), described in some detail in reference [20]. For the beams in the first year of operation at the LHC, uncertainties in measuring the N_i limit the precision of the luminosity measurement to about ± 3.4%.

A further expression for the LHC luminosity is given by

$$L = \frac{N_b^2 n_b f_{rev} \gamma_r}{4\pi \epsilon_n \beta^*} F \tag{3.3}$$

where N_b is the number of particles per bunch, n_b the number of bunches per beam, f_{rev} the revolution frequency, γ_r the relativistic gamma factor, ϵ_n the normalized transverse beam emittance, β^* the beta function at the collision point, and F is a geometric luminosity reduction factor related to the crossing angle [11]. Table 3.1 lists the nominal values of beam parameters for proton-proton running at peak luminosity of 1.0×10^{34} cm^{-2}s^{-1}. During the 2010 run period, using 3.5 TeV colliding beams, the peak luminosity of 2×10^{32} cm^{-2}s^{-1} was obtained with 348 colliding bunches, a transverse normalized emittance of 2.1 μm, β^* of 3.5 m, and a full crossing angle of 200 μrad [21].

The machine luminosity will decrease with time during the course of a run as a result of beam-beam interactions and other factors. The estimated average luminosity lifetime is 15 hours. In light of this, it is necessary to periodically refill the beam. The time required to do so is referred to as turnaround time, and is calculated to be a minimum of 70 minutes for the LHC.

3.4 The Incident

On the 19th of September 2008, while sector 3-4 was being commissioned at high current for 5 TeV operation, an electrical fault led to a mechanical failure and a massive helium leak into the vacuum enclosure [22].

Specifically, the fault lay with one of the splices in the superconducting busbars that serve as connections between the dipole magnets. The specification for these splices is that the resistance should be below 0.6 nΩ, while the splice that failed was measured to have reached 220 nΩ. Though the quench-detection systems (QDS) in the dipoles themselves were operating properly, the QDS monitoring the busbars turned out not to be sensitive to the appropriate level, only registering changes at

Table 3.1: Important design LHC beam parameters [11].

Data	Injection	Collision
Number of particles per bunch	1.15×10^{11}	
Number of bunches	2808	
Revolution frequency [kHz]	11.245	
Relativistic gamma	479.6	7461
Transverse normalized emittance [μm]	3.5	3.75
β at IP1 and IP5 [m]	18	0.55
Geometric luminosity reduction factor F[a]	-	0.836
Proton energy [GeV]	450	7000
Circulating beam current [A]	0.582	
Stored energy per beam [MJ]	23.3	362

---

[a] Depends on the total crossing angle at the IP. The quoted number assumes a total crossing angle of 285 μrad as it is used in IP1 and IP5.

the order of magnitude of 300 mV, compared to the 2 mV that was produced by the resistive zone. In addition to splicing the superconducting cables, these busbar interconnects are outfitted with a copper stabilizer that is designed to double as a fail-safe conductor able to carry the current in the event of a quench. However, for the joint that failed, contact between the superconducting cables and the copper stabilizer was also faulty. These problems resulted in thermal runaway, followed by an electrical arc that punctured the helium enclosure [23].

The helium safety relief valves were unable to accommodate the sudden pressure increase resulting in significant longitudinal forces beyond the tolerances of the magnet supports. This led to large magnet displacements and subsequent damage. As a result, 53 magnets—39 dipoles and 14 short straight sections—had to be removed from the tunnel and brought to ground level for inspection, cleaning, and repair. In addition, four jumper connections in the cryogenics system were deformed and had to be replaced [24].

The full impact of the incident was, however, not limited to the immediate damages to LHC components. It also resulted in a detailed investigation into the nature and cause of the electrical fault, as well as an implementation of preventative measures to ensure that any similar situations are avoided in the future. This included systematic testing of similar magnet interconnections, the development of a system to monitor the development of abnormal electrical resistances, and increasing the number and size of the pressure relief devices.

As a result of this program, all bad joints in the interconnections for the LHC sectors that had been raised to room temperature were found and corrected. Three defective splices located within dipole magnets were also repaired. In the three sectors that remained cold, an upper limit on the possible severity of remaining defects was placed, resulting in a limit of 4.5 T for safe operation of the magnets, allowing for collisions at 3.5 TeV per beam [23]. The overall delay imposed on the LHC operation schedule was slightly over one year, with the LHC resuming operation at 900 GeV in November of 2009 before a winter shut-down, and then finally ramping up to the first year operating energy of 7 TeV in March 2010.

Chapter 4

ATLAS Detector

The ATLAS detector is a complex device composed of several subsystems, each with a specialized focus. The four main subsystems are: the inner tracker, the calorimeter (which is further divided into electromagnetic and hadronic sections), the muon system, and the trigger system. The following treats each of the systems in turn, focusing on their design philosophies, principles of operation, and performance.

4.1 Coordinate System

Throughout this thesis the standard ATLAS coordinate system will be used, with the x-axis pointing towards the center of the LHC ring, the y-axis pointing upwards, and the z-axis aligned colinear with the beamline and chosen so as to make the system right-handed. Furthermore, R refers to the distance from the beamline in the plane perpendicular to the z-coordinate, with ϕ being the azimuthal angle, and θ the polar angle. The pseudorapidity is defined as $\eta = -\ln \tan \frac{\theta}{2}$.

4.2 Inner Tracker

The inner tracker, also referred to as inner detector (ID), provides precision measurements of the charged particle tracks produced by each recorded collision event. It is divided into three main parts. The innermost is the pixel detector, followed by the silicon microstrips (SCT), and finally the transition radiation tracker (TRT). The inner tracker surrounds the LHC beam pipe in a cavity with inner radius of 36 mm, outer radius of 115 cm, and length along the beam axis of seven meters. It is divided into a barrel region spanning ±80 cm, and two end-cap sections [25].

The entire inner tracker is located within the 2 T magnetic field produced by the ATLAS central solenoid. This magnet has a length of 5.3 m and a diameter of 2.5 m. The pixel and SCT subsystems combine to provide high precision track measurements in the pseudorapidity interval $|\eta| < 2.5$, while the TRT produces a significant number of hits in exchange for lesser precision and covers the region $|\eta| < 2.0$ [26].

The pixel detectors provide the highest granularity and are arranged in three layers. The innermost layer, referred to as the B layer or the vertexing layer, is located at a radius of 51 mm and provides important impact parameter and vertexing information. Overall the pixel detector has approximately 80.4 million readout channels [26].

The SCT has four layers in the barrel and nine in the end caps, with each layer consisting of a pair of stereo strips (one rotated by 40 mrad with respect to the other) to allow measurement of both coordinates [25]. The whole of the SCT consists of approximately 6.3 million readout channels.

The TRT is a straw tube tracker, using 4 mm diameter tubes to obtain track coordinates in the plane transverse to the solenoid axis. The TRT on average provides around 30 hits per track and because of this it plays an important role in both the track momentum measurement and pattern recognition [26]. Additionally, the transition radiation tracker provides information for use in electron reconstruction, although its design was not optimized for this purpose [25]. The total number of TRT readout channels is approximately 351,000 [26].

A summary of the important parameters of the inner tracker is given in Table 4.1, while a cross-sectional view of the inner detector is displayed in Figure 4.1.

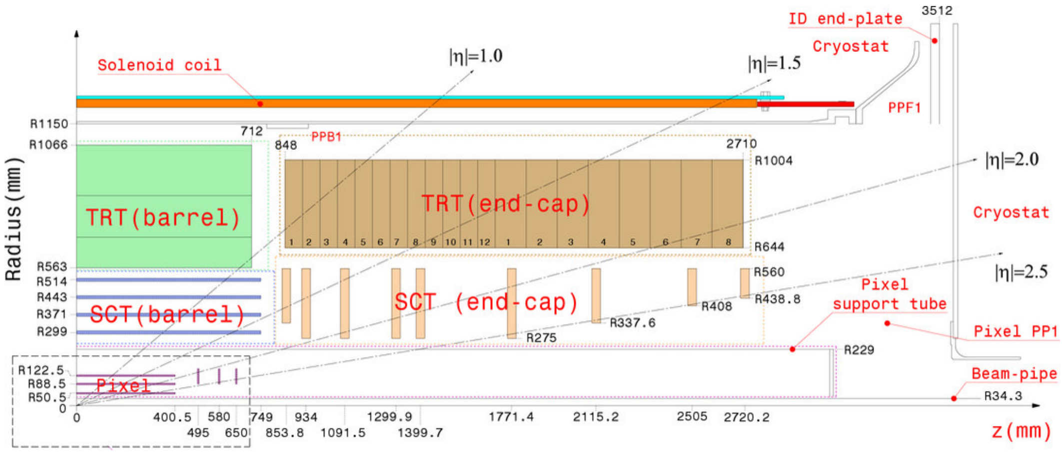

Figure 4.1: Cross-section of the ATLAS inner tracker [26].

Table 4.1: Main parameters of the ATLAS inner tracker [26].

Item		**Radial extension (mm)**	**Length (mm)**
Pixel	Overall envelope	$45.5 < R < 242$	$0 < \|z\| < 3092$
3 cylindrical layers	Sensitive barrel	$50.5 < R < 122.5$	$0 < \|z\| < 400.5$
2 × 3 disks	Sensitive end-cap	$88.8 < R < 149.6$	$495 < \|z\| < 650$
SCT	Overall envelope	$255 < R < 549$(barrel)	$0 < \|z\| < 805$
		$251 < R < 610$(end-cap)	$810 < \|z\| < 2797$
4 cylindrical layers	Sensitive barrel	$299 < R < 514$	$0 < \|z\| < 749$
2 × 9 disks	Sensitive end-cap	$275 < R < 560$	$839 < \|z\| < 2735$
TRT	Overall envelope	$544 < R < 1082$(barrel)	$0 < \|z\| < 780$
		$617 < R < 1106$(end-cap)	$827 < \|z\| < 2744$
73 straw planes	Sensitive barrel	$563 < R < 1066$	$0 < \|z\| < 712$
160 straw planes	Sensitive end-cap	$644 < R < 1004$	$848 < \|z\| < 2710$

4.3 Calorimeter

The ATLAS calorimeter provides precision reconstruction of electrons, photons, and hadronic jets. The calorimeter's broad coverage of the central rapidity region allows accurate measurements of missing transverse energy (MET), essential for searches for new physics. The calorimeter is divided into electromagnetic (EM) and hadronic sections, with further subdivisions in each.

The EM calorimeter is a lead-liquid argon (LAr) calorimeter, using an accordion geometry for full ϕ coverage. It is composed of three sections, each in its own cryostat. The barrel section covers $|\eta| < 1.475$ and two identical end-cap sections cover $1.375 < |\eta| < 3.2$. Additionally, a presampling layer covers the region $|\eta| < 1.8$. It is used to correct for the energy lost by electrons and photons in the inner tracker and beam pipe [27]. The total thickness of the EM calorimeter is greater than 22 radiation lengths (X_0) in the barrel and greater than 24 X_0 in the end-caps [26].

The hadronic calorimeter is subdivided into a scintillator tile calorimeter in the barrel region, and a LAr calorimeter in the end-caps. Additionally, a LAr forward calorimeter (FCal) is integrated into the end-cap cryostats. The scintillator tile calorimeter is located directly beyond the EM calorimeter and covers the region $|\eta| < 1.7$. It is segmented in depth in three layers, approximately 1.5, 4.1, and 1.8 interaction lengths (λ) thick for the central barrel and 1.5, 2.6, and 3.3 λ for the extended barrel. The LAr Hadronic End-cap Calorimeter (HEC) is located directly beyond the EM end-caps. It shares the same cryostats but uses copper instead of lead plates. The range covered by the HEC is $1.5 < |\eta| < 3.2$. Finally, the FCal is approximately 10 interaction lengths deep and consists of three modules in each end-cap: the first, made of copper, is optimized for electromagnetic measurements, while the other two, made of tungsten, measure predominantly the energy of hadronic interactions. The extent of the FCal is $3.1 < |\eta| < 4.9$ [27].

Details of the various calorimeters are found in Table 4.2, while Figure 4.2 provides a pictorial view.

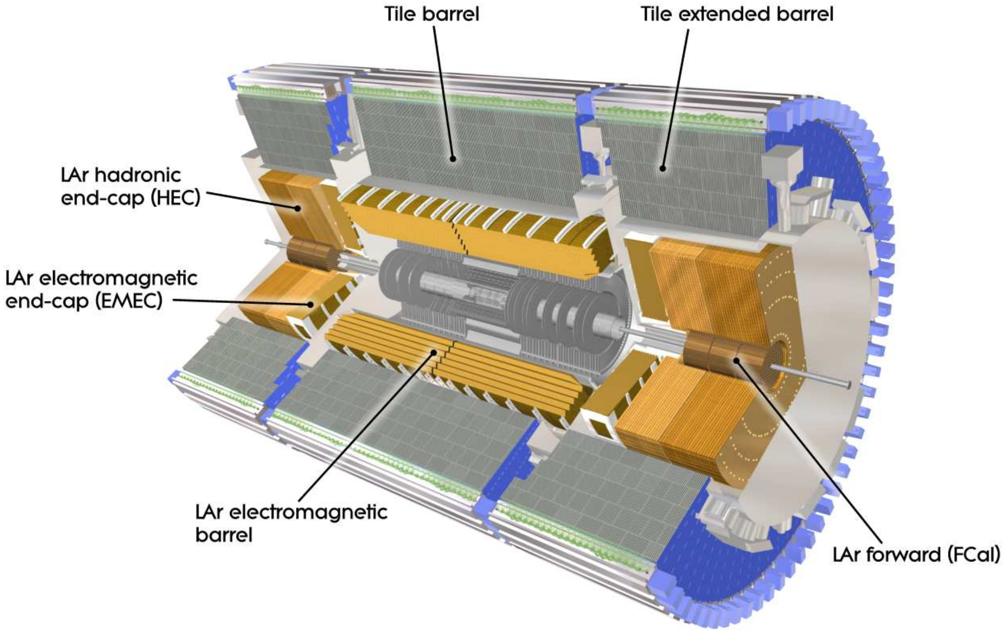

Figure 4.2: ATLAS calorimeters [27].

4.4 Muon System

4.4.1 Overview

Muons in the ATLAS detector are detected and measured with a dedicated muon spectrometer (MS) enveloping the rest of the detector. While electrons and hadrons are absorbed by the calorimeters, the muons pass through and are deflected by toroidal magnets. This provides a momentum measurement that can then be compared with the muon momentum obtained by the Inner Detector.

The ATLAS detector has four distinct types of chambers for the detection of muons, with each chamber technology tailored to a different need. Monitored Drift Tube (MDT) chambers comprise a large fraction of all muon chambers and provide

Table 4.2: Main parameters of the ATLAS calorimeter [27].

	Barrel		**End-cap**	
EM calorimeter				
Number of layers and $\|\eta\|$ coverage				
Presampler	1	$\|\eta\| < 1.52$	1	$1.5 < \|\eta\| < 1.8$
Calorimeter	3	$\|\eta\| < 1.35$	2	$1.375 < \|\eta\| < 1.5$
	2	$1.35 < \|\eta\| < 1.475$	3	$1.5 < \|\eta\| < 2.5$
			2	$2.5 < \|\eta\| < 3.2$
Granularity $\Delta\eta \times \Delta\phi$ versus $\|\eta\|$				
Presampler	0.025×0.1	$\|\eta\| < 1.52$	0.025×0.1	$1.5 < \|\eta\| < 1.8$
Calorimeter 1st layer	$0.025/8 \times 0.1$	$\|\eta\| < 1.40$	0.050×0.1	$1.375 < \|\eta\| < 1.425$
	0.025×0.025	$1.40 < \|\eta\| < 1.475$	0.025×0.1	$1.425 < \|\eta\| < 1.5$
			$0.025/8 \times 0.1$	$1.5 < \|\eta\| < 1.8$
			$0.025/6 \times 0.1$	$1.8 < \|\eta\| < 2.0$
			$0.025/4 \times 0.1$	$2.0 < \|\eta\| < 2.4$
			0.025×0.1	$2.4 < \|\eta\| < 2.5$
			0.01×0.1	$2.5 < \|\eta\| < 3.2$
Calorimeter 2nd layer	0.025×0.025	$\|\eta\| < 1.40$	0.050×0.025	$1.375 < \|\eta\| < 1.425$
	0.075×0.025	$1.40 < \|\eta\| < 1.475$	0.025×0.025	$1.425 < \|\eta\| < 2.5$
			0.1×0.1	$2.5 < \|\eta\| < 3.2$
Calorimeter 3rd layer	0.050×0.025	$\|\eta\| < 1.35$	0.050×0.025	$1.5 < \|\eta\| < 2.5$
Number of readout channels				
Presampler	7808		1536 (both sides)	
Calorimeter	101760		62208 (both sides)	
LAr hadronic end-cap				
$\|\eta\|$ coverage			$1.5 < \|\eta\| < 3.2$	
Number of layers			4	
Granularity $\Delta\eta \times \Delta\phi$			0.1×0.1	$1.5 < \|\eta\| < 2.5$
			0.2×0.2	$2.5 < \|\eta\| < 3.2$
Readout channels			5632 (both sides)	
LAr forward calorimeter				
$\|\eta\|$ coverage			$3.1 < \|\eta\| < 4.9$	
Number of layers			3	
Granularity $\Delta\eta \times \Delta\phi$			FCal1: 3.0×2.6	$3.15 < \|\eta\| < 4.30$
			FCal1: $\sim$ four times finer	$3.10 < \|\eta\| < 3.15$
			FCal1: $\sim$ four times finer	$4.30 < \|\eta\| < 4.83$
			FCal2: 3.3×4.2	$3.24 < \|\eta\| < 4.50$
			FCal2: $\sim$ four times finer	$3.20 < \|\eta\| < 3.24$
			FCal2: $\sim$ four times finer	$4.50 < \|\eta\| < 4.81$
			FCal3: 5.4×4.7	$3.32 < \|\eta\| < 4.60$
			FCal3: $\sim$ four times finer	$3.29 < \|\eta\| < 3.32$
			FCal3: $\sim$ four times finer	$4.60 < \|\eta\| < 4.75$
Readout channels			3524 (both sides)	
Scintillator tile calorimeter				
	Barrel		Extended barrel	
$\|\eta\|$ coverage	$\|\eta\| < 1.0$		$0.8 < \|\eta\| < 1.7$	
Number of layers	3		3	
Granularity $\Delta\eta \times \Delta\phi$	0.1×0.1		0.1×0.1	
Last layer	0.2×0.1		0.2×0.1	
Readout channels	5760		4092 (both sides)	

precision measurements of one spatial coordinate per tube. Cathode Strip Chambers (CSC) are deployed in regions of high pseudorapidity ($|\eta| > 2.0$), in the layer closest to the interaction point where they must operate in a high-rate environment. The CSCs provide precision measurements along one coordinate direction as well as a rough measurement of the second orthogonal coordinate. The other two types of chambers are similar in function, providing the means to trigger muon events, and yielding measurements of the second coordinate. They consist of Thin Gap Chambers (TGC) for the end-cap regions of the detector and Resistive Plate Chambers (RPC) for the barrel region.

The various muon chambers are assembled in different *stations* (called inner, middle, and outer), providing enough measurements to reconstruct muons. The triggering chambers are located alongside the precision chambers, shown in Figures 4.3 and 4.4. In the barrel these three stations are concentric cylinders about the beam line, while in the end-cap these stations are installed in wheels perpendicular to the beam line. Table 4.3 provides a summary of chamber parameters and number of chambers for each type of technology.

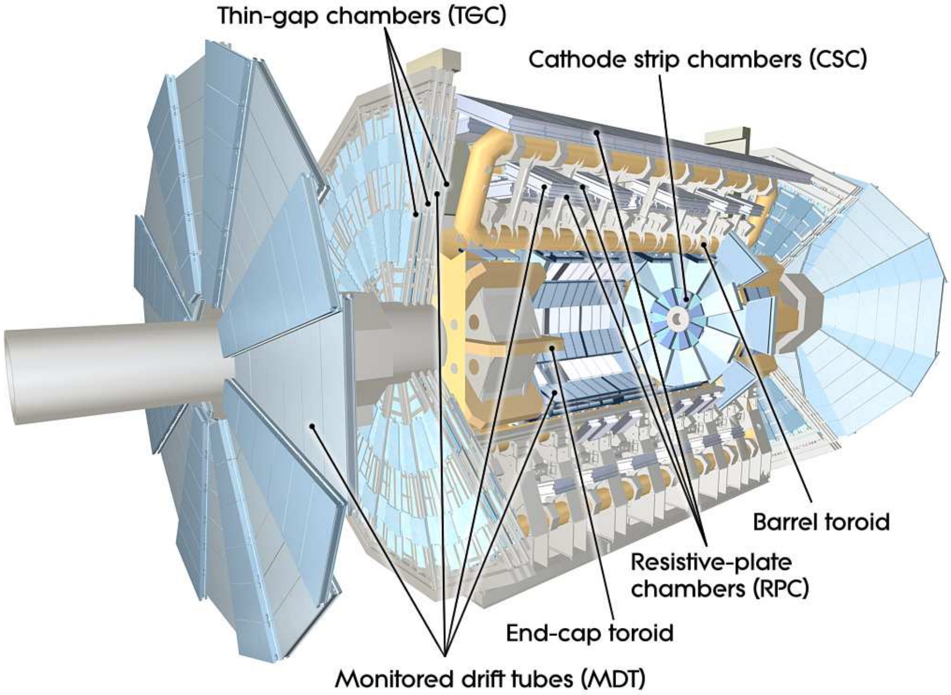

Figure 4.3: Cut-away view of the ATLAS muon system [27].

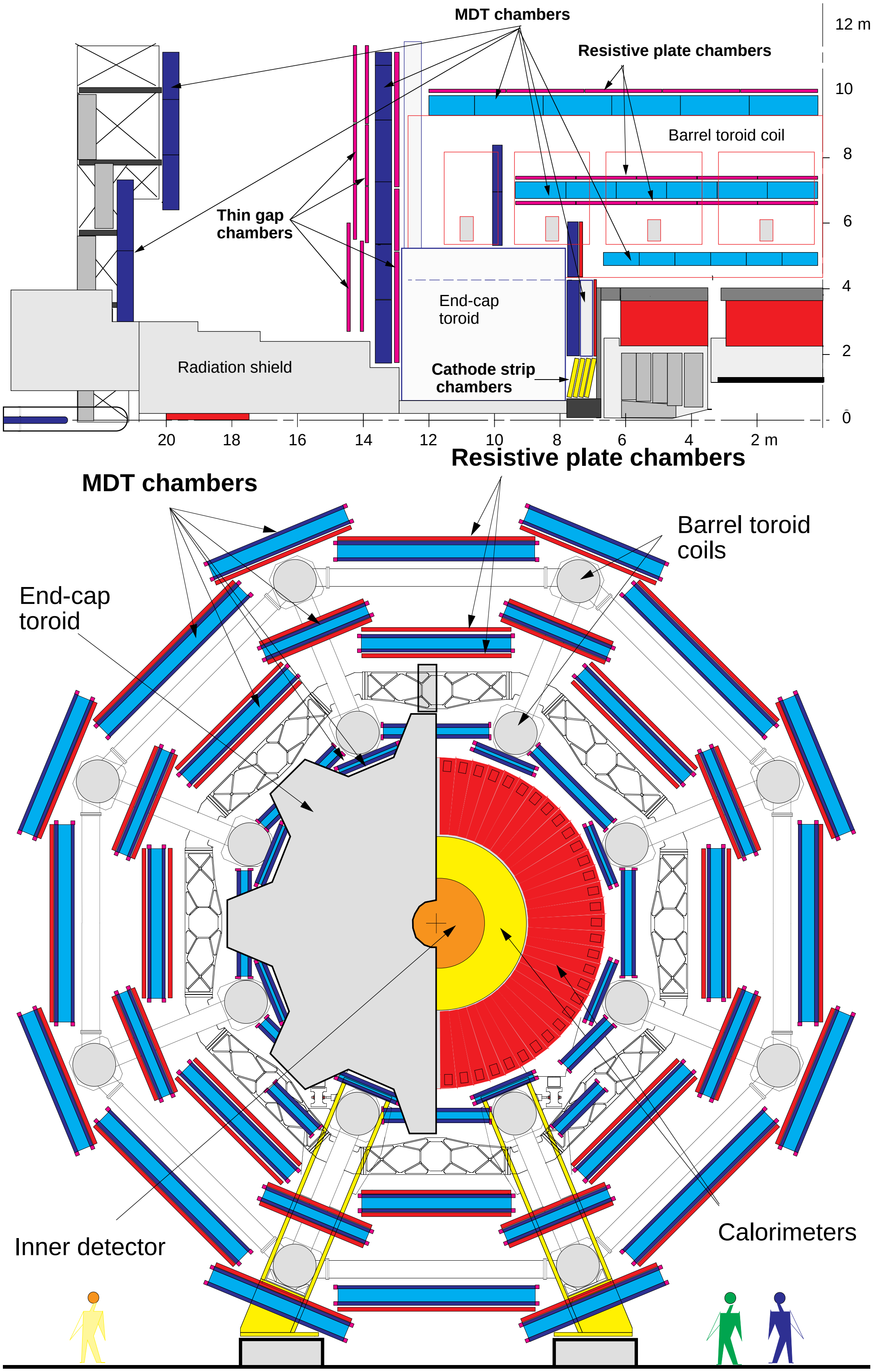

Figure 4.4: Cross-sections of the ATLAS muon system [28].

Table 4.3: Main parameters of the ATLAS muon spectrometer [27].

		Chamber resolution (RMS) in			**Measurements/track**		**Number of**	
Type	**Function**	z/R	ϕ	time	barrel	end-cap	chambers	channels
MDT	Precision	35 μm (z)	—	—	20	20	1150	354k
CSC	Precision	40 μm (R)	5 mm	7 ns	—	4	32	30.7k
RPC	Trigger	10 mm (z)	10 mm	1.5 ns	6	—	606	373k
TGC	Trigger	2-6 mm (R)	3-7 mm	4 ns	—	9	3588	318k

4.4.2 ATLAS Toroids

The magnetic field of the ATLAS muon spectrometer is produced by a set of three superconducting air-core toroids: one large barrel toroid, and two smaller toroids for the end-caps. The barrel toroid covers the region $|\eta| < 1.4$, while the end-cap toroids cover $1.6 < |\eta| < 2.7$. The remaining region, $1.4 < |\eta| < 1.6$, is referred to as the *transition region*, and the magnetic field there results from the combined fields of the barrel and end-cap toroids.

Each of the toroids is constructed with eight coils distributed evenly around the beam line, with the end-cap toroids rotated by 22.5 degrees with respect to the barrel toroid. The bending power of the barrel toroid is 1.5 to 5.5 Tm within its range of pseudorapidity coverage, while the bending power of the end-cap magnets is 1 to 7.5 Tm. In the transition region, this bending power is reduced [27].

4.4.3 Muon Precision Chambers

Monitored Drift Tube Chambers

The precision tracking of muons is accomplished with chambers composed of layers of aluminum tubes filled with pressurized gas (a mixture of 93% Ar and 7% CO_2 at 3 bar). Each tube surrounds a sense wire operated at high voltage (3080 V). When a muon passes through a tube, it ionizes some of the gas atoms. Ionization electrons drift toward the sense wire and generate a further ionization avalanche which produces a detectable signal on the wire. This signal is recorded as a hit. The maximum drift time for a track passing the wall of the tube to reach the center wire is $\sim$ 750 ns, and the spatial resolution of each tube is 75 μm. A summary of key MDT parameters is listed in Table 4.4.

Chambers in the barrel and in the end-cap have different shapes to ensure proper coverage. Barrel chambers are rectangular while end-cap chambers have a trapezoidal geometry. As mentioned previously, the MDTs are arranged in three stations of increasing distance from the beam line and they are labeled accordingly. Furthermore, the chambers are divided into 16 azimuthal sectors and alternate between large and

Table 4.4: MDT parameters [29].

Tube material	Aluminum
Outer tube diameter	29.970 mm
Tube wall thickness	0.4 mm
Wire material	gold-plated W/Re (97/3)
Wire diameter	50 μm
Gas mixture	$Ar/CO_2/H_2O$ ($93/7/\leq 1000$ ppm)
Gas pressure	3 bar (absolute)
Gas gain	2×10^4
Wire potential	3080 V
Maximum drift time	$\sim$ 750 ns
Resolution per tube	$\sim$ 75 μm

small chambers. This information, as well as individual chamber number within a sector, is enough to completely specify an MDT chamber. For example BML5 would specify the fifth azimuthal sector of the middle (M) barrel (B) station, which is a large (L) sector. Several additional special chambers deviate from the main design in order to accommodate detector support structures (such as the BOF and BOG sectors), or to maximize coverage (such as the EES or EEL chambers).

Cathode Strip Chambers

The CSCs are multi-wire proportional chambers, designed to provide precision measurements in the high pseudorapidity area of the detector where the expected counting rate at maximum luminosity might exceed the limit allowed for safe operation of MDT chambers.

The CSC chambers are constructed with the anode-cathode spacing equal to the pitch of the anode wires. The precision measurement is obtained by measuring the relative difference in charge induced in adjacent strips. The chambers have strips both perpendicular to and parallel to the wires, allowing for simultaneous measurement of orthogonal coordinates. The resolution is 60 μm for the precision coordinate and 5 mm for the second coordinate. Table 4.5 lists basic operating parameters of the CSCs.

4.4.4 Muon Trigger Chambers

Differences in detection requirements exist over the pseudorapidity range of the detector, and these become important when considering event triggering. In the high η region the muon momentum to p_T ratio is very different than it is in the barrel.

Table 4.5: CSC parameters [27].

Operating voltage	1900 V
Anode wire diameter	30 μm
Gas gain	6×10^4
Gas mixture	Ar/CO_2 (80/20)
Total ionization (typical track)	$\sim$ 90 ion pairs

Furthermore, magnetic field differences in these regions must also be taken into account. For these reasons two different chamber technologies were chosen, Resistive Plate Chambers (RPCs) in the barrel region, and Thin Gap Chambers (TGCs) in the end-caps.

In both the end-cap and barrel regions the trigger chambers are deployed adjacent to the precision MDT chambers. The RPCs have two layers surrounding the middle layer of the MDTs with the third layer either on the outside of the outer layer or the inside of the inner layer, depending on the chamber's azimuthal location. For the TGCs there is one layer on the inside of the inner layer of the MDTs, and three layers surrounding the middle layer. The layout of these trigger chambers is designed to select muons satisfying preselected momentum thresholds as seen in Figure 4.5.

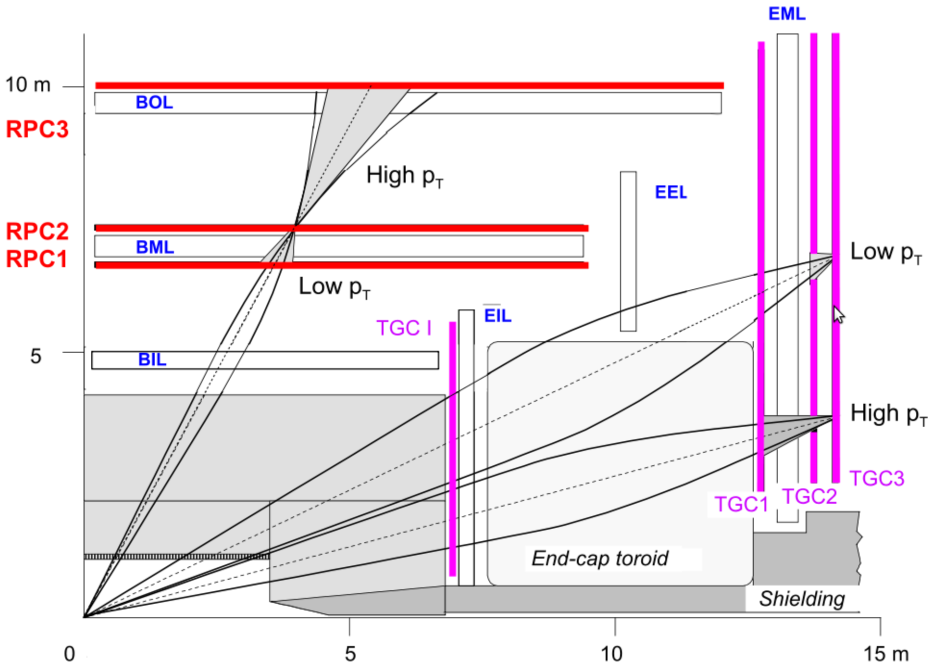

Figure 4.5: Muon triggering schemes for different transverse momenta[27].

Resistive Plate Chambers

The RPCs are wireless, their principle of operation instead relies on the electric field between two parallel resistive plates. Avalanches form along ionizing tracks and the resulting signals are read out by capacitive coupling to strips on the outside of the resistive plates. These strips are oriented in both the η and ϕ directions, allowing measurement of both coordinates. A summary of RPC parameters is found in Table 4.6.

Table 4.6: RPC parameters [27].

E field in gap	4.9 kV/mm
Gas gap	2 mm
Gas mixture	$C_2H_2F_4$/Iso-C_4H_{10}/SF_6 (94.7/5/0.3)
Readout pitch of η and ϕ strips	23–35 mm
Intrinsic time jitter	≤ 1.5 ns
Local rate capability	~ 1 kHz/cm^2

Thin Gap Chambers

TGCs provide the muon trigger and second coordinate measurement in the end-caps. Their operation is similar to that of multiwire proportional chambers, with construction parameters (e.g. wire-to-wire distance, anode pitch, electric field value) chosen to provide the necessary timing requirements. Basic TGC parameters are listed in Table 4.7.

Table 4.7: TGC parameters [27].

Gas gap	2.8 mm
Wire pitch	1.8 mm
Wire diameter	50 μm
Wire potential	2900 V
Operating plateau	200 V
Gas mixture	CO_2/n-pentane (55/45)
Gas amplification	3×10^5

4.5 Trigger System

4.5.1 Overview

Event triggering in the ATLAS detector is based on a three tier approach. First, a decision is made based purely on hardware response. This is the level one (L1) trigger decision. Following that, two successively more involved trigger levels make use of additional information to refine the decision whether to record the event on disk. These additional triggers stages are the level two (L2) and event filter (EF). Collectively the L2 and EF triggers are referred to as High Level Triggers (HLT). This threefold trigger scheme is responsible for winnowing down the $\sim$ 40 MHz collision rate to 200 Hz of interesting events to be recorded to disk.

L1

The L1 trigger has a window of operation of 2.5 μs in which to make its decision to accept or reject an event and at this stage it must reduce the rate to $\sim$ 75 kHz, a rejection factor of nearly 500 [26]. At this level the decision is based on detector signals such as energy deposits in the EM calorimeters or muon chamber hits. As the L1 trigger makes its decision it identifies regions of interest (ROIs) and passes them onward to the HLT.

L2

Information from the L1 trigger is used to seed the L2 trigger, which makes its decision after running fast software algorithms on the ROIs identified by L1, evaluating the event with finer granularity and with a more detailed analysis. The operating time allotted to L2 algorithms is 40 ms, and the additional rejection afforded at this step brings the acceptance rate to $\sim$ 2 kHz, an additional reduction factor of 40 on top of that afforded by L1 [26].

EF

The EF receives the input of the earlier trigger decisions and is responsible for the final reduction in rate required to bring it to 200 Hz. EF algorithms are typically the same as those used in offline event reconstruction.

4.5.2 Muon Triggers

This thesis is concerned with the decay of a Z boson to two muons, and as such the particularities of the muon portion of the trigger decision making process warrant further elaboration. As mentioned before, the muon system has dedicated chamber technologies to provide input to the trigger, and these are the RPCs for the barrel ($|\eta| < 1.05$) and the TGCs for the end-cap ($1.05 < |\eta| < 2.40$).

L1

At L1 the trigger algorithms examine hit coincidences in both η and ϕ, before sending the information onward to the Muon to Central Trigger Processor Interface (MuCTPI). This unit determines the number of muon candidates that pass certain transverse momentum thresholds. These thresholds are labeled MU0, MU6, MU10, MU15, and MU20 where the number following the 'MU' is the requirement (in GeV) on the muon p_T; MU0 denotes completely open coincidence intervals and can be used to trigger on cosmic rays [26][30]. The MuCTPI is also responsible for taking into account the overlap between trigger sectors through the use of look-up tables.

L2

L2 triggering makes use of algorithms which request additional detector information about the ROI provided by L1 in an attempt to identify specific muon features before making a decision to accept or reject the event. The main algorithm at L2 is muFast, which runs on the full granularity of the L1 ROI [31]. By analyzing the pattern of trigger hits, the algorithm searches for MDT regions along the expected path of the muon before performing a track fit on the precision hits. The muon p_T is then determined by look-up tables, and the reconstructed muon is passed to another algorithm, muComb, which attempts to find a match between the muon and an ID track.

MuFast operates in three sequential steps: global pattern recognition, local segment identification, and a fast transverse momentum estimate [32]. The global pattern recognition identifies the precision chambers with hits near the trigger hits contained in the ROI found by L1. These are then fit locally, and look-up tables are used to provide the p_T estimate.

EF

At the EF level the trigger has access to all the event data at full granularity, with enough time available to run full reconstruction algorithms. It uses the muons found at L2 as inputs, and performs futher operations on those. At this stage three muon objects are reconstructed from the same information: one in the MS only, another by extrapolating the muon track back to the interaction point, and finally one that combines this extrapolated track with a track from the ID. At this stage the effective trigger thresholds are set so that, at the nominal trigger threshold (the X listed in MUX), the trigger efficiency is 90% [26].

The algorithms used for the EF trigger are "Muon Object Oriented REconstruction" (MOORE) and "MuonIDentification" (MuID). MOORE handles the reconstruction of the track in the MS, while MuID performs the extrapolation and combination aspects [33]. These algorithms in the trigger can be implemented in two fashions: directly on the whole event, as would be done in the offline reconstruction, or seeded by either the L1 or L2 information.

The MOORE algorithm begins with crude local pattern recognition and attempts to construct straight line segments from muon hit information [34]. These segments are then stored, further refined, and ultimately combined into a complete track.

The MuID algorithm then proceeds to associate these MOORE tracks with information from the calorimeter and from the ID tracks, to improve resolution for muons with intermediate momentum. It first performs a refitting, using the hits from the MS and five parameters for the calorimeters (two scatter centers and an energy loss factor) to obtain the track extrapolation [34]. Following this, it performs a matching of this Standalone (SA) track with the ID track, forming a χ^2 with five degrees of freedom. The final result is a combined fit of all available information (ID hits, MS hits, calorimeter scatter centers).

4.6 Muon Tracking Algorithms

The ATLAS muon system provides three categories of reconstructed muons labelled according to quality. The highest quality muons are called *Combined* muons, and have fully reconstructed tracks in both the inner-detector and the muon spectrometer. Another quality category identifies so-called *Tagged* muons, combining a track in the inner detector with either a track stub in the muon spectrometer or calorimetry deposits matching a muon signature. Muons with low transverse momentum that penetrate but fail to traverse the muon spectrometer would fall into the Tagged category. A third quality category identifies muons as *Standalone*, in which the muon is measured in the muon spectrometer but no matching inner-detector track is found.

Furthermore, ATLAS has two complementary families of algorithms, based on different design philosophies, which both produce reconstructed muons for each quality level. The two families are referred to by the name of the algorithm used to select Combined quality muons: MuID, and STACO. The STACO algorithm performs a statistical combination [35] of the ID and MS tracks and their covariant matrices, while the MuID combination is produced by a global refit of all track hits in the ID and the MS [36]. The Standalone algorithm associated with MuID is MOORE [37], while the STACO uses Muonboy [38]. Reference [39] outlines further the differences between the two, and demonstrates that both have comparable performance. In this thesis results will be presented using muons from the MuID family of algorithms.

4.7 Luminosity Measurement

ATLAS is equipped with several detector elements whose purpose is the measurement of luminosity, as discussed in some detail in the previous chapter.

While the primary purpose of the Minimum Bias Trigger Scintillator (MBTS) is to provide a trigger for every inelastic collision event, it is also used in the calculation of luminosity. The coverage range of the MBTS is $2.09 < |\eta| < 3.84$ [40].

LUCID is one of the components of ATLAS dedicated to luminosity measurement as indicated by its acronym (LUminosity measurement using a Cherenkov Integrating Detector). LUCID consists of sixteen aluminum tubes surrounding the beam pipe on each side of the ATLAS detector that are filled with C_4F_{10} gas. The Cherenkov radiation emitted when charged particles pass through the gas is collected and sent to photomultiplier tubes where it is measured and compared against threshold values. The coverage of the LUCID system is $5.6 < |\eta| < 6.0$ [40].

Another element is the Zero Degree Calorimeter (ZDC), whose primary purpose is to detect neutral particles in the very forward region, $|\eta| > 8.3$. It operates under similar principles to the other calorimeters and also consists of electromagnetic and hadronic sections.

Also playing important roles are detector elements previously discussed, such as the Inner Detector, and the LAr forward calorimeters. All these elements work together to determine the average number of interactions per beam crossing, μ, from Equation 3.1.

4.8 ATLAS Data Acquisition and Analysis

Even after imposing strict trigger requirements, ATLAS will record vast amounts of data, up to an estimated 3 petabytes per year. To properly manage the flow of data and to handle the reconstruction of raw data into physics objects, a comprehensive computing structure has been established [41]. The computing model adopted by ATLAS relies on several factors, including a distributed Tier system, as well as several different data formats designed for certain purposes [42].

4.8.1 Computing Model

As events pass the HLT, the information from the read out devices (RODs) of the individual detector elements are recorded by the detector as raw data in bytestream format. This is then stored at what is called Tier 0, the computing infrastructure located at CERN. At this central site events are analyzed with algorithms that identify and characterize "physics objects" such as electrons, photons, muons, jets, and other charged particles [41]. To accomplish this task, the reconstruction algorithms consult a network of databases that store information pertaining to detector conditions, calibration, and alignment.

The process takes place in stages, shown schematically in Figure 4.6 with the raw data first being reconstructed into files known as Event Summary Data (ESD), before further preparation is performed resulting in Analysis Object Data (AOD) files. From the AODs the files are further filtered into Derived Physics Data (DPD) files for the purpose of conserving disk space, and decreasing program run-time. DPDs are often tailored to specific analysis requirements, and keep only relevant quantities of interest through the methods of skimming (removing undesired events), thinning (removing undesired objects), and slimming (reducing the stored information per object).

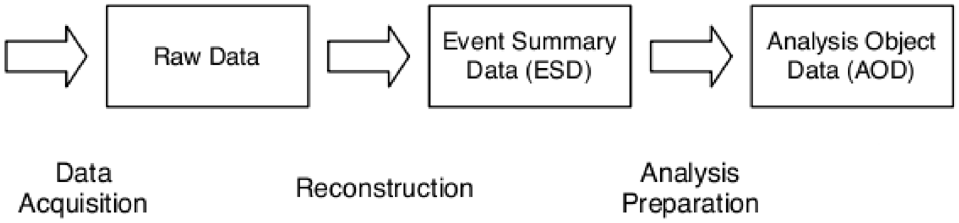

Figure 4.6: Flow of data file production [41].

The resulting files are distributed to ten Tier 1 sites distributed across the world, one of which is located at Brookhaven National Laboratory. In addition to the full set of ESDs and AODs, the Tier 1 facilities also host a fraction of the raw data directly. Furthermore, dozens of Tier 2 sites exist with similarly global distribution, including five in the United States, one of which is located at the University of Michigan. These Tier 2s hold partial replicas of the complete set of AODs, are the major centers for generating the Monte Carlo simulation of various physics processes, and additionally serve to address more specific needs such as acting as calibration centers. A diagram outlining the tier structure is found in Figure 4.7.

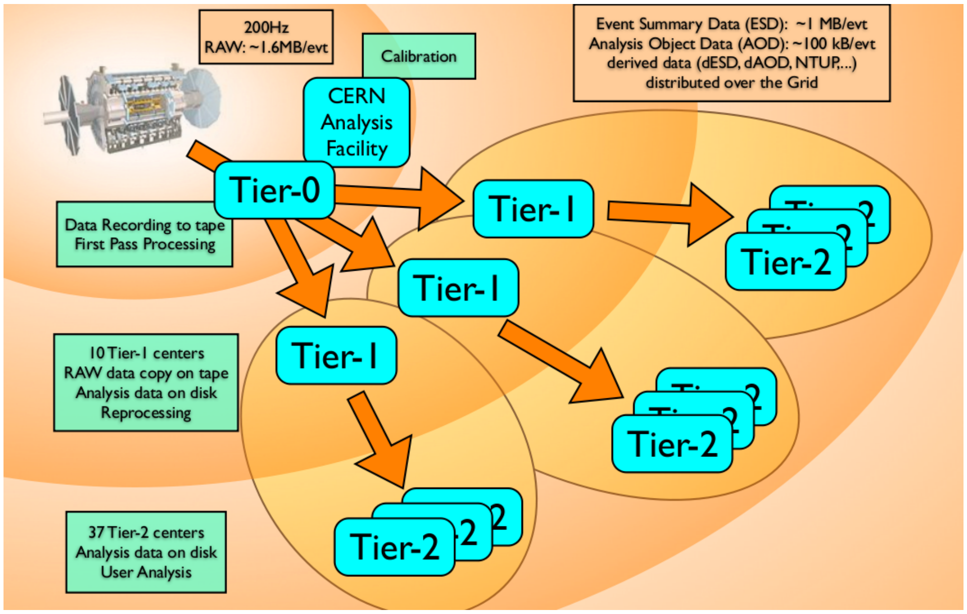

Figure 4.7: Distribution of data across the ATLAS Tier system [43].

Due to the distributed nature of the data, physics analysis is frequently performed in a likewise distributed fashion using the Grid. Further information on the specifics of Grid use can be found in reference [44].

Chapter 5

Monte Carlo Programs

5.1 Monte Carlo Principles

The Z production mechanisms discussed in Chapter 2 and illustrated through Feynman diagrams are only a part of the larger picture. Obtaining predictions based on theory with which to compare observation requires additional work. Due to the nature of the strong interaction and the principle of color confinement one cannot simply collide isolated quarks, antiquarks, and gluons, but must rather collide colorless bound states. In the LHC, the collision is between beams of protons. This has significant impact on the physics of the collisions as, in addition to the production processes shown in Figures 2.1–2.3, the remnants of the protons, and any newly produced partonic quarks or gluons, must also evolve into colorless states. This is referred to as hadronization, for which the details cannot be computed from first principles, but must rather be modeled using phenomenology. Further, the existence of higher-order diagrams that differ only in the amount of initial or final state radiation emitted by partons provides additional complication, as do the interactions of the produced particles as they pass through the detector.

To address all of the issues raised above, specialized computer programs have been developed to handle each stage of the process. Programs using Monte Carlo techniques produce the four-vectors of the particles in the skeleton process according to the appropriate probability distributions, and then apply subsequent corrections. This is referred to as *event generation*. One such event generator is PYTHIA. Following generation, the event can be simulated with a program, such a GEANT, with information about the specifics of the detector construction and response. This is referred to as *event simulation*. The final result of event generation and event simulation can then be analyzed with exactly the same reconstruction routines used to process actual data in order to provide a theoretical prediction for comparison purposes.

All of the Monte Carlo samples considered for this thesis were generated for a center of mass collision energy of 7 TeV, and with the Monte Carlo parameters tuned according to standard ATLAS MC09 specifications [45], designed to produce the best comparison with published data from prior experiments and using the latest PDF sets.

5.2 PYTHIA

PYTHIA is a leading-order Monte Carlo generator. It uses the Lund string model of fragmentation in order to model the hadronization process [46], which it combines with routines that do parton showering in the final state. PYTHIA can be run using different PDF functions as inputs, and can generate a wide variety of Standard Model and beyond SM processes.

For this thesis, PYTHIA implemented the MSRT LO* PDF set [47], which is a modified leading-order parton distribution set designed to give results close to those predicted by next-to-leading order when used in conjunction with leading-order generators. The process of interest for this thesis, that of Z production and decay to muons, is generated by setting PYTHIA's selection mode to full user control (MSEL=0) and selecting the 2 → 1 process $f\bar{f} \rightarrow Z/\gamma^*$ (ISUB=1). The γ^* contributions were varied using MSTP(43) to consider the full interference structure (the default setting), as well as Z-Only and γ^*-Only samples. The lepton decay products from the Z are produced with the correct angular distribution, accounting for spin correlations as well as fermion mass effects. The lower bound on the generated Z mass was set to 60 GeV. No generator level filter was applied, leaving the sample with the full range of generated momenta and rapidities.

In addition, PYTHIA can be interfaced with external programs, letting them perform their own manipulations on the core PYTHIA event. The ATLAS collaboration's default use of PYTHIA links it to the Tauola package for treatment of tau lepton decays, and to PHOTOS to perform final state radiation of photons.

5.3 MC@NLO

MC@NLO is a Monte Carlo generator that operates using next-to-leading order matrix element calculations and interfaces them with existing parton shower generators.

It utilizes a subtraction method to avoid double counting and produces events with positive and negative weights [48]. The MC@NLO samples analyzed in this thesis use the CTEQ 6.6 NLO PDFs and have the HERWIG/JIMMY generator handle the parton showering and underlying event. Again, our interest is the Z production and decay to muons, which is selected by IPROC -1353 [49]. This setting includes γ^* and interference effects as well as spin correlation of the decay leptons. Samples of Z-Only were not produced or considered using MC@NLO. The lower bound for the generated Z mass was 60 GeV and the upper bound was 7 TeV. No generator level filter was applied. The MC@NLO samples were also interfaced to the Tauloa and PHOTOS packages.

5.4 GEANT

The GEANT toolkit provides a framework for managing the detector simulation. GEANT uses a description of the detector geometry and material composition in combination with an array of packages modelling the response of particles in matter [50]. The packages address processes such as electromagnetic, hadronic, and optical responses making use of the material geometry to handle the interactions as the particles are transported through the detector. Possible decays for long-lived particles and the effects of multiple scattering are also taken into account. As the interactions occur the readout detector geometry is used to provide the expected final response of the detector in the same format as for actual data, providing (for example) pixel hits, ADC/TDC counts, and calorimeter cell response.

ATLAS maintains its detector description in a separate geometry database, which allows both ease of use in both simulation and reconstruction programs as well as for maintaining records for different detector configurations (such as when recording data with magnetic fields turned off) [51].

Chapter 6

Measurement of Z Cross-Section

6.1 Definition of Signal

This thesis presents a measurement of the cross-section for Z production with subsequent decay to $\mu^+\mu^-$ using 40237 nb^{-1} of data collected by the ATLAS detector during the 2010 operational period. This covers ATLAS runs numbered from 152166 to 167844 taken between March and November. Analysis is performed on Derived Physics Data (DPD) files produced from the ATLAS standard Analysis Object Data (AOD) files. The DPDs were produced and validated under the direction of Haijun Yang on behalf of the diboson physics working group. These data files were slimmed, skimmed, and thinned to provide samples suitable for any high p_T lepton analysis. Events were required to have at least one electron or muon (of any quality designation) with a transverse momentum of at least 10 GeV and with an absolute value of pseudorapidity of less than 2.7.

While in some analyses the goal is a measurement of the combined cross-section for Z/γ^*, taking into account Drell-Yan and interference effects, here the signal definition is to be taken as strictly those events arising from the resonance production of the Z boson. The motivation behind this choice is that a measurement of the pure Z cross-section has important implications not covered by Z/γ^*. For instance, the Z couples to neutrinos through the weak interaction while γ^* does not. In many searches for new physics, the production of missing transverse energy (MET) plays a pivotal role. Standard Model neutrinos appear in detectors as MET, so having an accurate handle on their production through $Z \to \nu\bar{\nu}$ is desirable for properly considering them as "background" to possible new phenomena.

This choice of signal definition requires additional analysis steps to attain a result. For a measurement of Z/γ^* one can simply count the number of dimuon events observed in a mass window and then subtract off a contribution for QCD and other possible backgrounds, estimated either through Monte Carlo or data driven techniques. Due to the purity of the signal, such effects are small. However, to isolate the Z contributions from the γ^*, the background subtraction process becomes more complicated. The current analysis addresses this task through fitting the dimuon invariant mass distribution to a functional form with two parts, modeling a combination of pure Z signal and background. The Z signal is taken to be a Breit-Wigner function, shown in Expression 6.1, with a fixed width $\Gamma = 2.495$ GeV (corresponding to the measured world average for the Z [7]) that is smeared by a Gaussian resolution function.

$$C_1 \frac{\Gamma}{2\pi} \frac{1}{(E-M)^2 + \frac{\Gamma^2}{4}} \tag{6.1}$$

The absolute normalization C_1, the central value for the mass of the Z, and the variance of the Gaussian σ are free parameters of the fit. The background is parametrized by the exponential function shown in Expression 6.2

$$C_2 e^{ax}, \tag{6.2}$$

where x is the mass in GeV and C_2 and a are allowed to vary. The motivation for using an exponential as the functional form for the background is based in part on the observation that it matches the expected contribution from γ^*. This can be seen in Figure 6.1, showing a Monte Carlo simulation of the dimuon mass distribution due to γ^* plotted on a logarithmic scale, which appears to fall off nearly linearly.

These choices result in some of the signal being classified as background, however, as modeling for final-state radiation (FSR) in the form $Z \to \mu\mu\gamma$ is not included in the signal shape. A correction factor to address this is covered in Section 6.11.

6.2 Ingredients of the Cross-Section Measurement

The cross-section measurement is based on the following relationship:

$$\sigma = \frac{N}{A \cdot C \cdot L}, \tag{6.3}$$

where N is the number of observed signal events corrected for final-state radiation, C is a correction factor related to trigger and muon reconstruction efficiencies, A is an acceptance factor associated with finite detector coverage, and L is the integrated

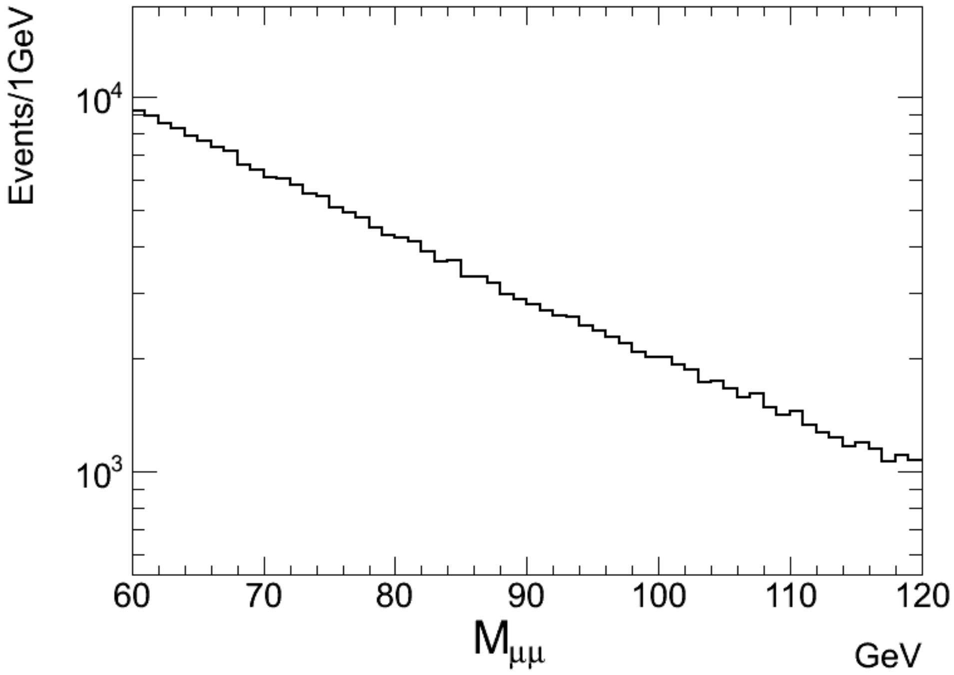

Figure 6.1: $\gamma^* \rightarrow \mu^+\mu-$ mass distribution in PYTHIA. The shape appears as a straight line on a semi-log plot, indicating exponential behavior.

luminosity.

The number of observed Z bosons, the efficiencies that determine the correction factor, and the acceptance factor all depend on the specific selection criteria chosen to extract the Z signal. The program for identifying $Z \rightarrow \mu\mu$ is explored in full detail in Section 6.3, where various parameters and choices of cuts are considered.

The correction factor C is comprised of a combination of various efficiencies, each of which is determined separately using data-driven techniques. The first major efficiency is that of the muon event trigger. This efficiency can be studied in various ways. The method chosen for this thesis examines events selected by a trigger orthogonal to the muon trigger used in the Z analysis. This orthogonal trigger is based on information from the calorimeter system. Events passing this trigger are then examined to see if they contain reconstructed muons, and then further to see whether those muons fired the muon trigger. This procedure is discussed at length in Section 6.4.

The next key efficiency, that to reconstruct the type of quality muons used in the Z selection analysis, is a combination of the individual efficiencies for reconstructing the muon's track in the Inner Detector (ID), in the Muon Spectrometer (MS), and for the determination of whether or not the muon is isolated. These three efficiencies can each be studied in data using a method known as *Tag and Probe*. The general principle behind Tag and Probe exploits the decay of the Z resonance into a pair of muons. The first muon is a well-measured one, referred to as a *Tag*, while a second *Probe* muon is then examined. The Probe search is kept blind to the system whose efficiency is to be measured, but considers information from the rest of the detector. When the invariant mass of the Tag and the Probe is consistent with Z decay, there is confidence that the Probe muon is legitimate and not a "fake" muon misreconstructed by the detector. From there, the efficiency for it to pass the reconstruction category in question is studied, and the calculations for each of the measurements (ID, MS, and Isolation) are detailed in Sections 6.5, 6.6, and 6.7. The various efficiencies are combined into a single overall correction factor in Section 6.8.

The acceptance factor A corrects for the finite extent of the detector and must be determined by Monte Carlo studies examining the distribution of muons from generated Z bosons. By comparing the Z signal populating all of phase space with that in the limited kinematic region of the data, a relation between the measured fiducial cross-section and the expected total cross-section is derived. These studies are detailed in Section 6.9.

6.3 Z Selection Criteria

To obtain a clean sample of Z bosons from the data, a variety of requirements must be imposed on several discriminating variables. Those events which fail to satisfy these requirements are rejected from consideration. In the following investigations the measured dimuon invariant mass distribution at each stage in the selection process is fitted as was described in Section 6.1. Following the fit, the number of signal events is obtained by integrating the background function (using the parameters obtained from the fit) and subtracting this computed background from the total number of observed events.

The signal region covers the mass interval from 60 to 120 GeV. This interval was chosen because it is roughly symmetric about the Z mass and is wide enough to cover the tails of the Breit-Wigner distribution. Table 6.1 summarizes the results for a sequential series of requirements, including the number of events classified as signal and background, the chi-square per degree of freedom (χ^2/dof) associated with each fit, and the values obtained for the central value of the Z mass as well as the width of the fitted Gaussian resolution.

The obtained values of χ^2/dof indicate that the functional form of the fits represents an imperfect model of the shape of the measured mass distribution. Our fits do not model the radiative tail below the Z peak. However, by subtracting the fitted background from the total number of events in the dimuon mass interval the signal includes a major fraction of events in the radiative tail. A further correction factor for final-state radiation is discussed in Section 6.11. This neglect of final-state radiation in the fits is also partially responsible for the fact that the Z mass obtained from the fits is 0.5 GeV below the world average for M_Z [7].

Table 6.1: Cutflow fit results.

Sequential Requirements	N_Z	N_{BG}	$\frac{\chi^2}{dof}$	$M_Z(GeV)$	$\sigma(GeV)$
Triggered with $\mu^+\mu^-$	18795	39975	2.644	90.73	2.501
Muons from same good collision vertex	18598	7577	2.595	90.66	2.658
Muon impact parameters	18515	6865	2.750	90.66	2.669
Both muons combined	17613	4200	3.415	90.64	2.684
Both muons isolated	17542	1582	4.672	90.62	2.750
Both muons $p_T > 10$ GeV and $\lvert\eta\rvert < 2.5$	17094	1307	4.710	90.62	2.695
Both muons $p_T > 20$ GeV and $\lvert\eta\rvert < 2.4$	14892	859	4.280	90.69	2.649

The first dimuon mass histogram, shown in Figure 6.2, requires only that the event fired the muon trigger appropriate to the time period of the data run (see Section 6.4 for more details) and that the event contains two oppositely charged muons. At this stage of the analysis the Z peak contains approximately 19000 events sitting on a background of roughly twice that number. This background has many sources, including muons from cosmic rays and from pile-up collisions buried in the main event. To reduce these particular sources, track vertexing information is used.

We select good collision events by demanding the existence of a vertex with at least three tracks passing the quality threshold of having at least one pixel layer hit, and at least 6 SCT hits. The requirement of three tracks rejects most cosmic rays, since these generate only two apparent tracks as they pass straight through the detector. Such vertices are considered to be *good collision vertices*, and the distribution of the number of these per event is shown in Figure 6.3.

Next, we demand that the muons used to reconstruct the Z originate from the same good collision vertex. Figure 6.4 shows the dimuon mass distribution after this requirement. We note that the fitted Z signal has decreased by only a few hundred events, maintaining $\sim$ 99% of the previous value, while the background is now at approximately one fifth of its former value.

Additional improvement is obtained by cutting on the muon impact parameters with respect to the event vertex. These parameters are referred to as d_0 for the impact parameter in the transverse plane, and z_0 for the impact parameter along the

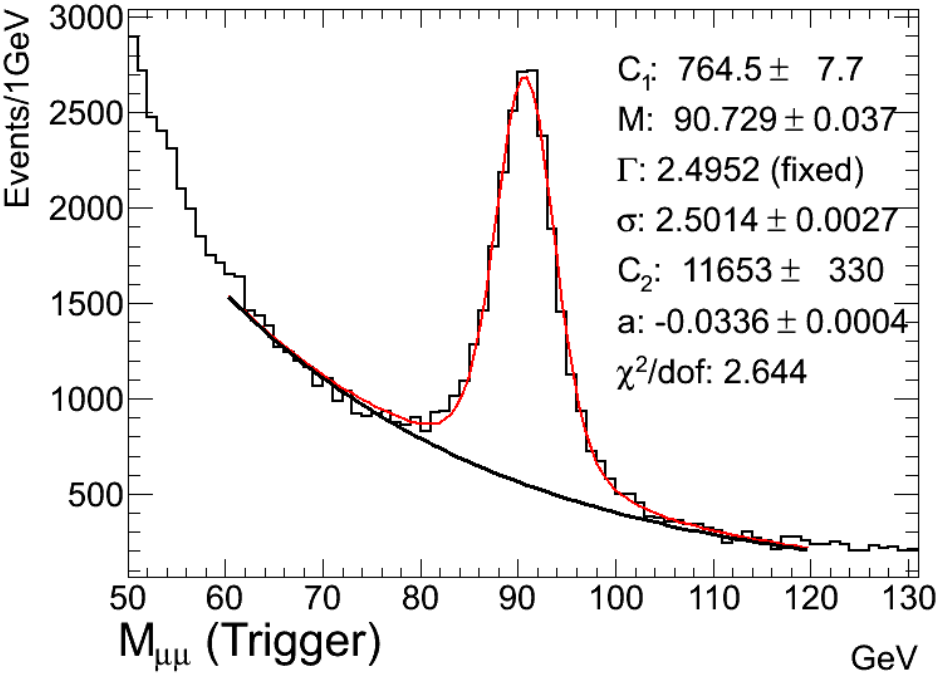

Figure 6.2: Dimuon invariant mass after a trigger requirement. There is a prominent Z signal on top of substantial background. In the region $60 < M_{\mu\mu} < 120$ GeV there are 39975 events classified as background leaving 18795 events as signal.

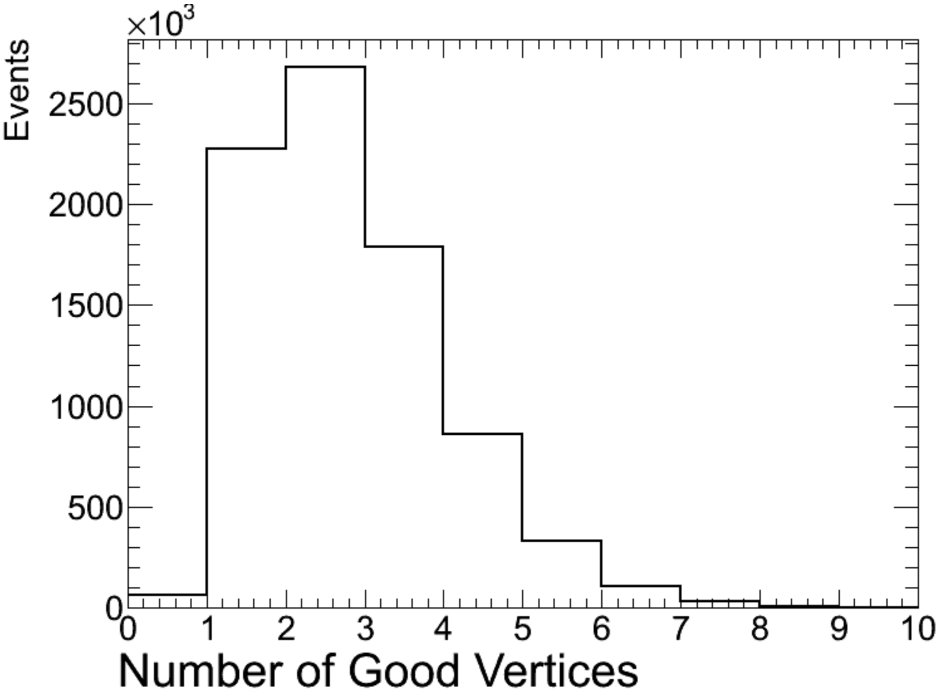

Figure 6.3: Distribution of the number of good vertices per event. This is filled after the requirement of the muon trigger.

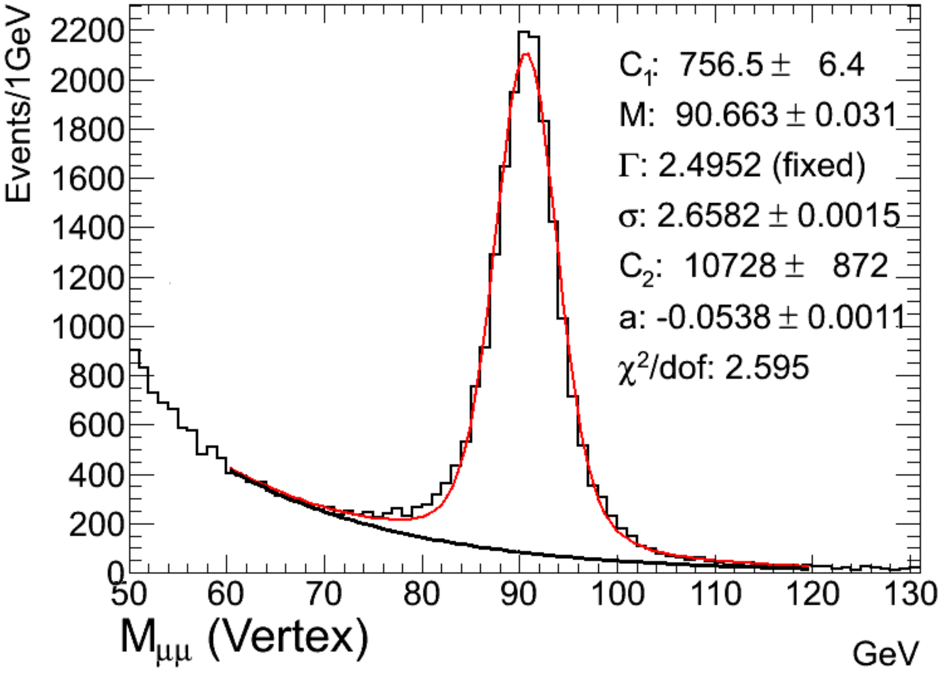

Figure 6.4: Dimuon invariant mass after a vertex requirement. Both muons are required to come from the same good collision vertex. In the region $60 < M_{\mu\mu} < 120$ GeV there are 7577 events classified as background leaving 18598 events as signal.

beam direction. Their distributions after the trigger and vertex cuts are shown in Figures 6.5 and 6.6. Requiring that $|d_0| < 1$ mm and $|z_0| < 5$ mm provides further confidence in the assignment of the muons to a good vertex. This selection preserves over 99% of the signal while rejecting another 10% of background events, as shown in Figure 6.7.

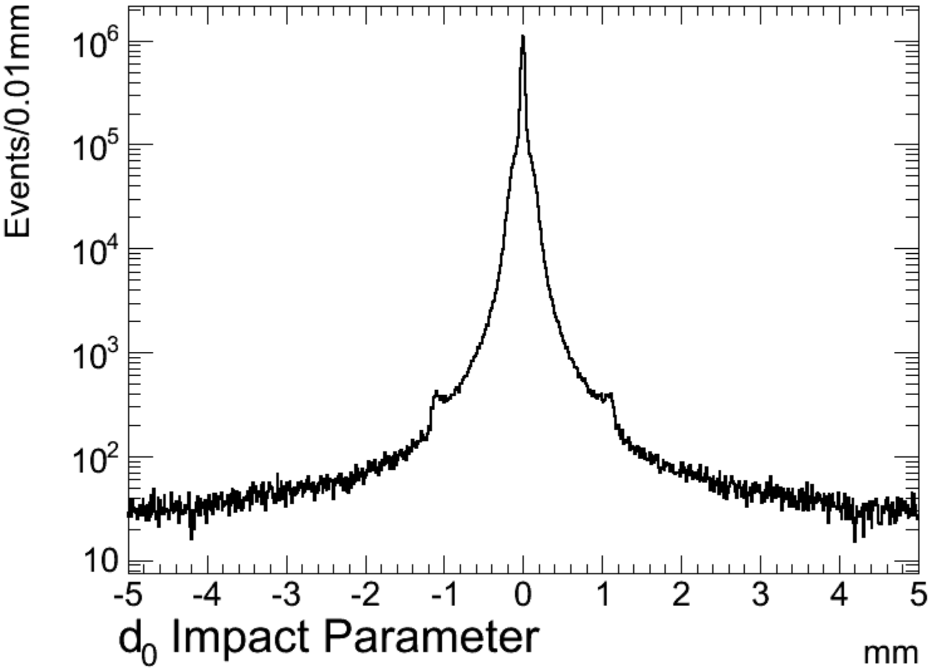

Figure 6.5: Distribution of the transverse impact parameter. This parameter, d_0, is shown for muons in events after the vertex cut has been applied.

The small bulges seen in the d_0 impact parameter distribution near ±1 mm were investigated further. As was discussed in Section 4.6, ATLAS has a variety of muon identification algorithms of various quality levels. Muons of the Standalone quality were found to be responsible for the small bulges in the d_0 distribution. Requiring all muons to be Combined muons produces the d_0 impact parameter shown in Figure 6.8, where the small bulges have vanished. The dimuon invariant mass distribution with the requirement that both muons have Combined quality is presented in Figure 6.9, where we see that the background has been further decreased by 39%, while preserving 95% of the signal.

Next, the degree to which each muon was *isolated* was investigated. Isolation is defined in terms of the sum of the transverse momenta of other ID tracks within a cone in R-space around the muon track. (R is defined as $\sqrt{(\Delta\eta)^2 + (\Delta\phi)^2}$.) This sum is normalized to the transverse momentum of the muon. The distribution of this

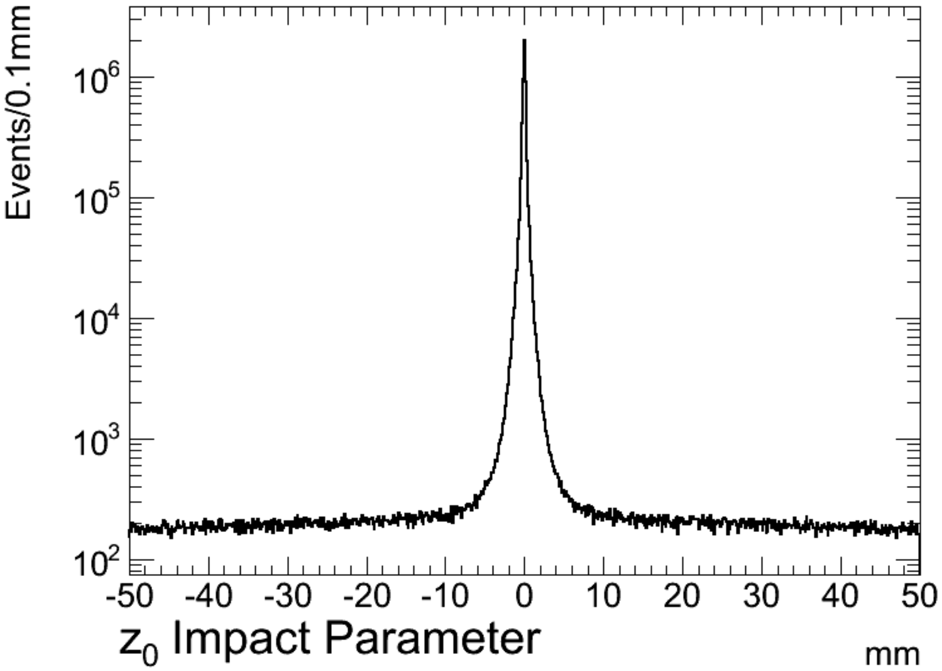

Figure 6.6: Distribution of the longitudinal impact parameter. This parameter, z_0, is shown for muons in events after the vertex cut has been applied.

normalized isolation variable is shown in Figure 6.10. Requiring that both muons possess an isolation parameter less than 0.20 produces the dimuon mass distribution shown in Figure 6.11.

Cuts on the muon transverse momentum and pseudorapidity were also explored. The p_T distribution is shown in Figure 6.12, and that of η in Figure 6.13. The structure seen in the transverse momentum distribution is due to several factors. One of these is the skimming requirement involved in the DPD file production, responsible for the peak at 10 GeV. Another factor is that the trigger threshold changed over time, responsible for the peak at 13 GeV. Requiring that both muons have a transverse momentum greater than 10 GeV and an absolute value of the pseudorapidity less than 2.5 yields the invariant mass distribution in Figure 6.14. Finally, an alternate set of kinematic cuts was applied to check the stability of the cross-section measurements. This second set of kinematic cuts required each muon to have a transverse momentum of at least 20 GeV and with an absolute value of the pseudorapidity less than 2.4. The mass distribution for these cuts is shown in Figure 6.15.

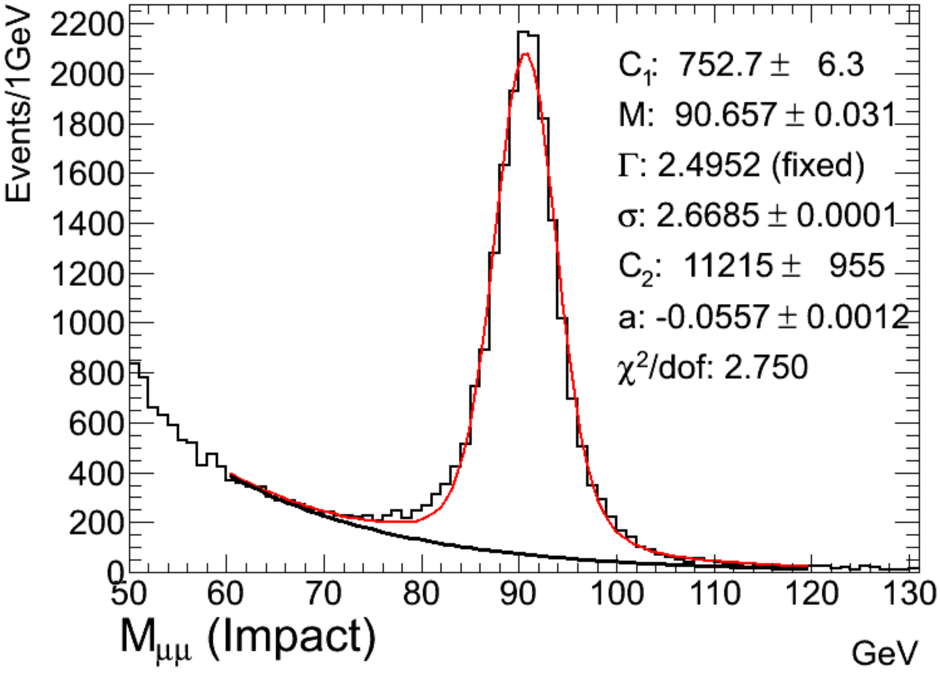

Figure 6.7: Dimuon invariant mass after an impact parameter requirement. Both muons are required to satisfy $|d_0| < 1$ mm and $|z_0| < 5$ mm. In the region $60 < M_{\mu\mu} < 120$ GeV there are 6865 events classified as background leaving 18515 events as signal.

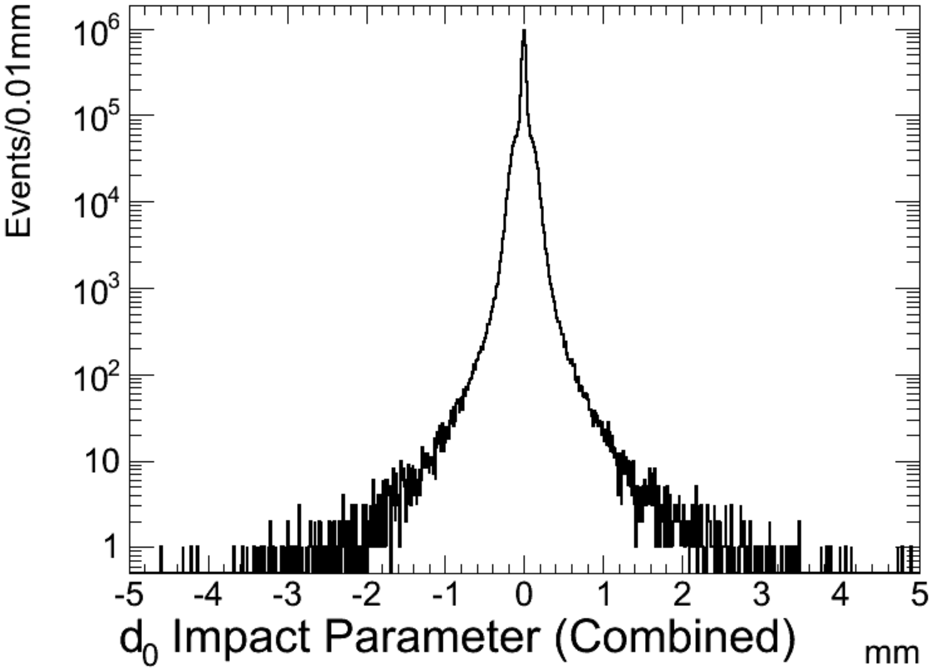

Figure 6.8: Transverse impact parameter distribution for Combined muons.

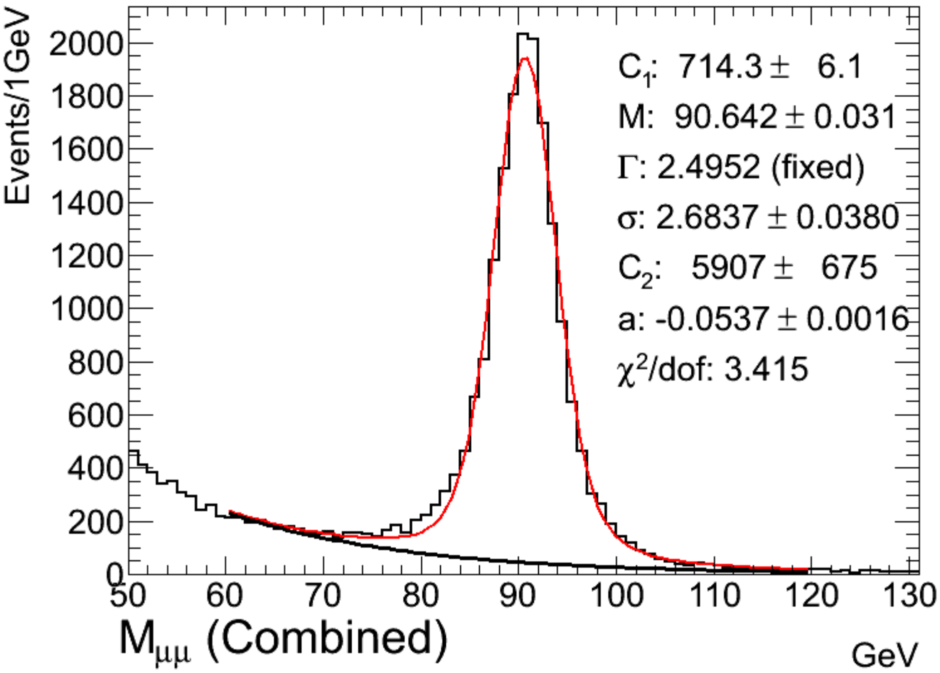

Figure 6.9: Dimuon invariant mass after requiring Combined quality. In the region $60 < M_{\mu\mu} < 120$ GeV there are 4200 events classified as background leaving 17613 events as signal.

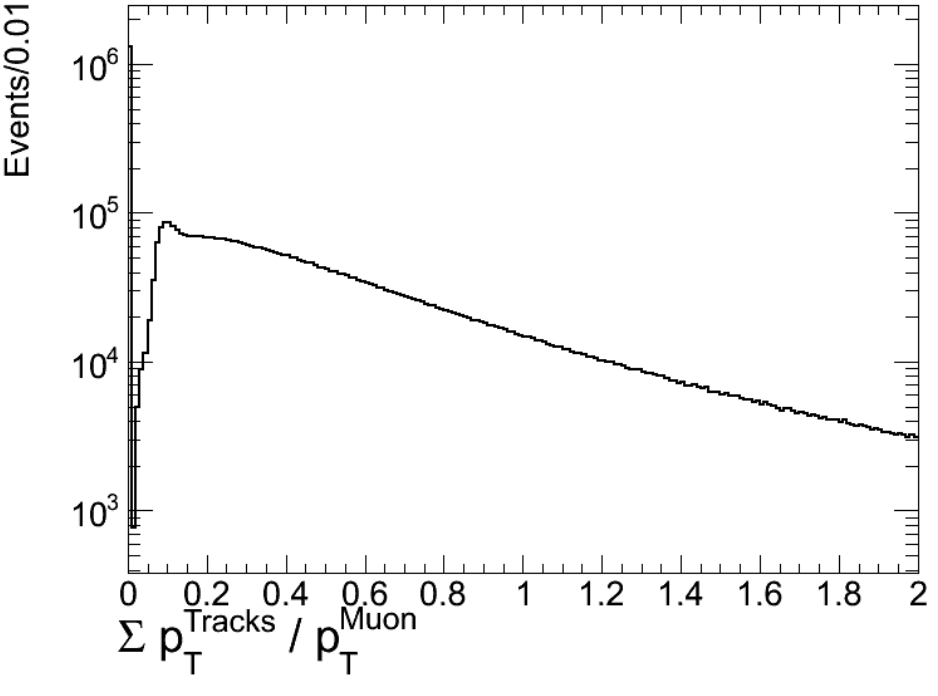

Figure 6.10: Distribution of the isolation variable. This follows the application of the previous cuts up to the Combined quality on muons.

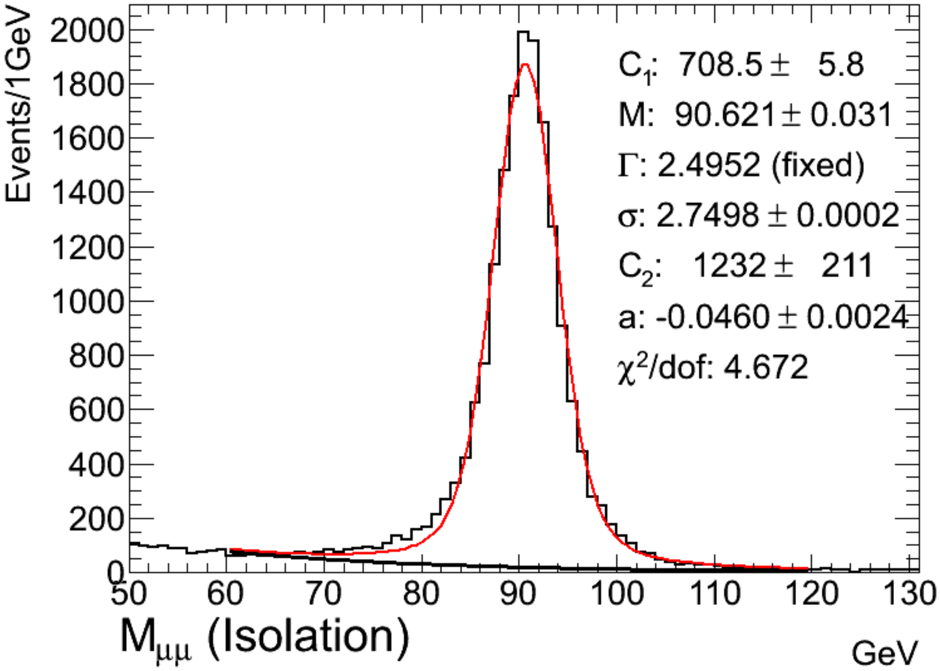

Figure 6.11: Dimuon invariant mass after the isolation requirement. Both muons are required to have isolation parameter<0.20. In the region $60 < M_{\mu\mu} < 120$ GeV there are 1582 events classified as background leaving 17542 events as signal.

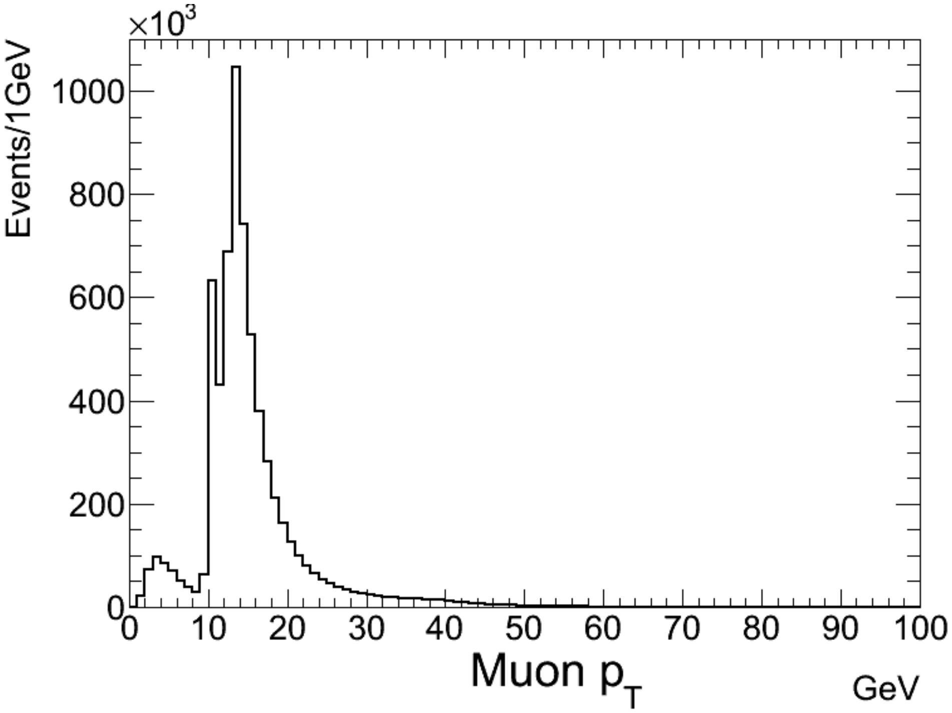

Figure 6.12: Distribution of the muon transverse momentum. Plotted after the requirement of all cuts through isolation.

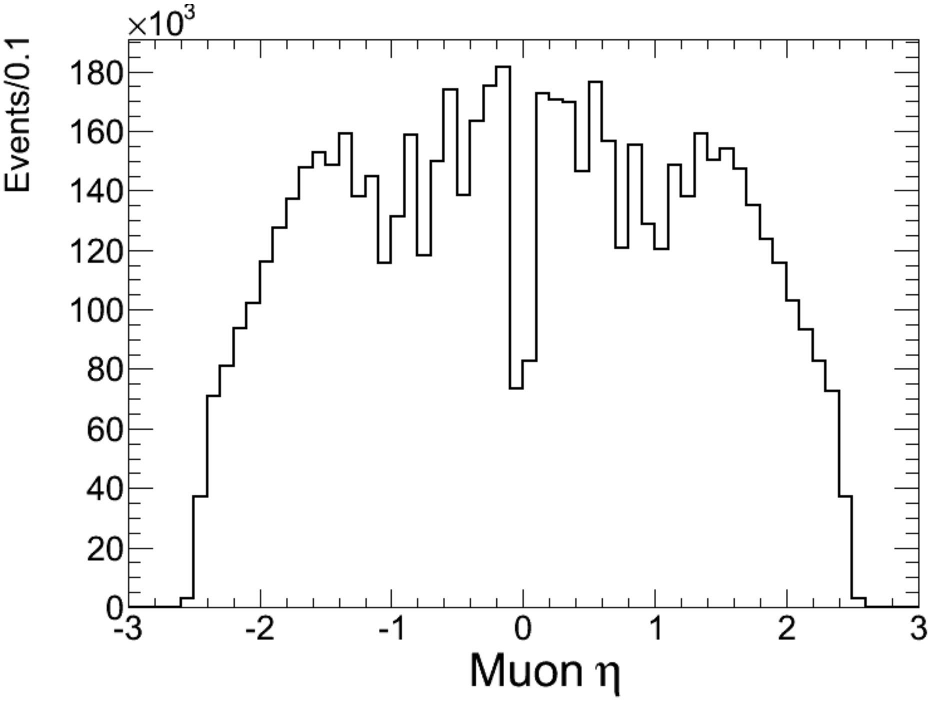

Figure 6.13: Distribution of the muon pseudorapidity. Plotted after the requirement of all cuts through isolation.

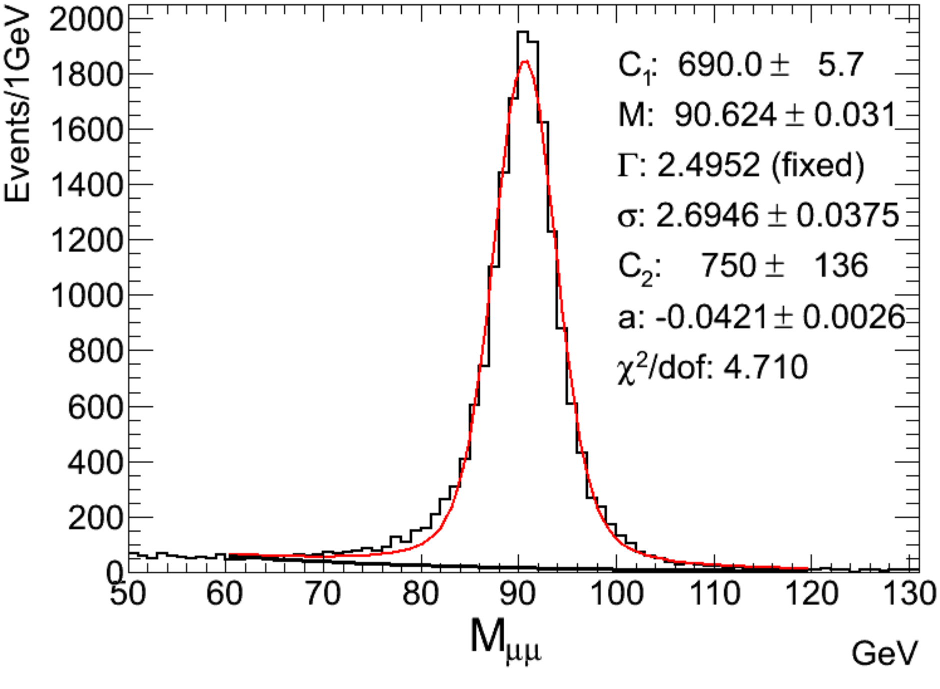

Figure 6.14: Dimuon invariant mass after kinematic requirements. Both muons are required to have $p_T > 10$ GeV and $|\eta| < 2.5$. In the region $60 < M_{\mu\mu} < 120$ GeV there are 1307 events classified as background leaving 17094 events as signal.

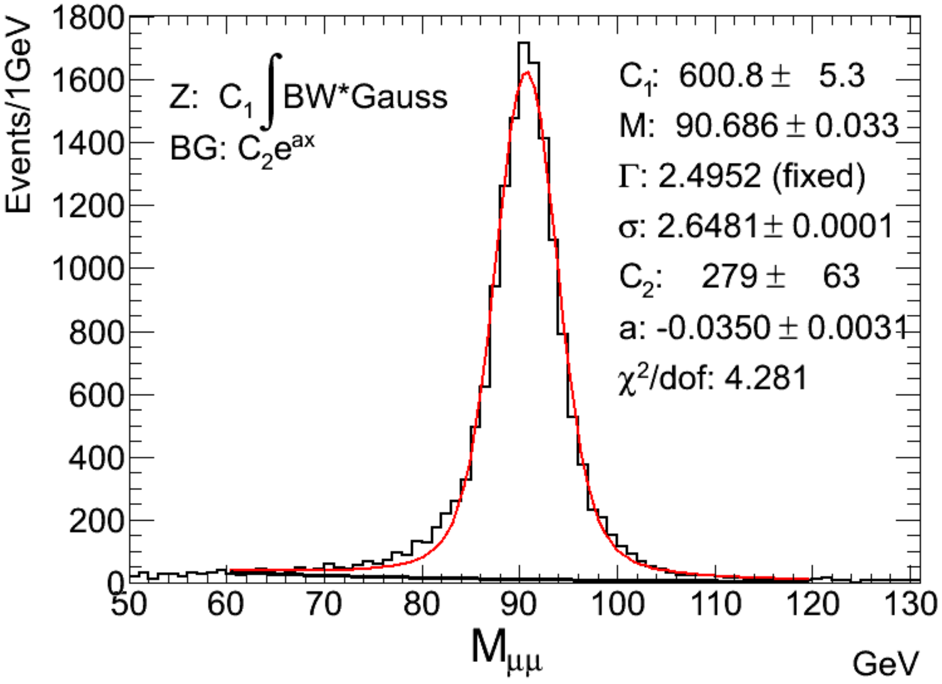

Figure 6.15: Dimuon invariant mass after alternate kinematic requirements. Both muons are required to have $p_T > 20$ GeV and $|\eta| < 2.4$. In the region $60 < M_{\mu\mu} < 120$ GeV there are 859 events classified as background leaving 14892 events as signal.

6.4 Efficiency of the Trigger System

The efficiency of the muon trigger is studied with an independent data sample obtained from non-muon triggers. The ATLAS data acquisition system creates several different *data streams* where events are stored according to trigger. These data streams are independent and inclusive. The main Z analysis relies on data in the "Muon stream". By considering events that are sorted into other independent streams and investigating whether they contain muons that fired the muon trigger, we can determine the muon trigger efficiency.

This process is slightly complicated by the fact that over the course of the first year of ATLAS running, the trigger system was constantly evolving, and changes were made to data stream production. This evolving situation—brought about by new triggers being added, old triggers becoming *prescaled* (the introduction of an arbitrary additional rejection factor designed to keep the overall event rate at a manageable level), and other factors—necessitated that the analysis used different trigger requirements for different periods of running. This required studies of trigger efficiencies for each time period. A summary of the time periods considered in this thesis, the muon trigger used, the corresponding integrated luminosity, and the muon trigger efficiency is provided in Table 6.2, with a more detailed breakdown of the efficiency for various detector rapidities found in Table 6.3. For the sake of brevity, plots for the variables and efficiencies studied will be provided only for Period 4, which had the highest statistics.

Table 6.2: Muon trigger summary for the ATLAS data used in the analysis. An explanation of the trigger names is found in the text. Average efficiencies are given for muons with $p_T > 20$ GeV and $|\eta| < 2.4$.

Period	Covering Runs	Muon Trigger Used	Luminosity (nb^{-1})	Muon Trigger Average Efficiency
Period 1	152166 — 159224	L1_MU6	318	80%
Period 2	160387 — 165818	EF_mu10_MG	6300	81%
Period 3	165821 — 166964	EF_mu13_MG	11492	84%
Period 4	167575 — 167844	EF_mu13_MG_tight	22127	82%
Grand Total			40237	

An attractive data sample for this trigger study consists of events triggered by jets and missing transverse energy, where we could expect to find W boson production and subsequent decay to muons. Such muons have kinematic properties similar to those from Z decay. For much of the overall running period, the "Tau, Jet, and Missing Energy stream" serves this purpose. However for the earliest time period, this stream

Table 6.3: Muon trigger efficiency by region. Average efficiencies are given for muons with $p_T > 20$ GeV and $|\eta| < 2.4$.

	Efficiency			
	$\eta < -1.05$ (End-cap)	$-1.05 < \eta < 0$ (Barrel)	$0 < \eta < 1.05$ (Barrel)	$1.05 < \eta$ (End-cap)
Period 1	86%	69%	80%	85%
Period 2	88%	69%	72%	93%
Period 3	95%	69%	75%	94%
Period 4	91%	73%	71%	91%

was not yet produced and so for this period the "L1Calo stream" was used instead. This stream was triggered by activity in the EM Calorimeter.

In this first period, corresponding to runs between 152166 and 159224, event rates were low and Level 1 triggers were not yet prescaled. Therefore, for this period, we use the Level 1 muon trigger "L1_MU6", where the MU6 indicates the trigger is for muons with a transverse momentum of at least 6 GeV.

For the trigger efficiency analysis, events were required to have a good collision vertex and to fire the L1_EM5 trigger, a Level 1 hardware trigger on electromagnetic calorimeter cluster deposits in excess of 5 GeV. We then searched for "good" muons, that is to say those muons passing the same quality requirements as described in Section 6.3 (isolated combined muons associated with a good vertex and passing impact parameter cuts). The kinematic requirements were $p_T > 5$ GeV, to allow observation of the trigger turn-on curve, and $|\eta| < 2.5$. Additionally, a cut on the missing transverse energy (MET) was applied, requiring at least 25 GeV, in an attempt to preferentially select for muons from W decays. This selection program was also used for the other trigger periods. In events with exactly one good muon, whether or not the L1_MU6 trigger fired then determines the muon trigger efficiency. For Period 1 the average muon trigger efficiency was found to be 80% for $p_T > 20$ GeV.

During the second trigger period, from runs 160387 to 165818, the muon trigger was EF_mu10_MG, an Event Filter level trigger for muons with a transverse momentum of at least 10 GeV. The trigger study for this period proceeds in the same way as it did for Period 1 except that instead of requiring a L1_EM5 trigger an OR of L1_J30_XE10 (a Level 1 trigger requiring a jet of at least 30 GeV and 10 GeV of missing energy) and L1_XE30 (a Level 1 trigger requiring at least 30 GeV of missing energy) triggers was used. The average efficiency for the muon trigger in this time period is 81% for $p_T > 20$ GeV.

The third trigger period, from runs 165821 to 166964, used the EF_mu13_MG muon trigger, identical to the one used in Period 2 except for a p_T threshold of 13 GeV. The average efficiency for the trigger in this time period is 84% for $p_T > 20$ GeV.

The final trigger period, from runs 167575 to 167844, used the EF_mu13_MG_tight muon trigger, identical to the Period 3 trigger except in that it is seeded by a different L1 trigger (L1_MU10 rather than L1_MU0). The muon trigger efficiency for this period is 82% for $p_T > 20$ GeV.

The transverse momentum and pseudorapidity distributions of muons found by the study are shown in Figures 6.16 and 6.17, and are similar to the distributions seen in the Z selection search. In addition, the distribution of the transverse mass variable, as calculated from Equation 6.4 (taking the W momentum variables to be a vector sum of the muon and MET variables in the transverse plane), is shown in Figure 6.18. A clear contribution from W decays is observed.

$$M_T = \sqrt{p^2 - p_x^2 - p_y^2} \tag{6.4}$$

Muon trigger efficiencies as a function of muon transverse momentum, pseudorapidity, and azimuthal angle are shown in Figures 6.19, 6.20, and 6.21, respectively. The figures for the η and ϕ dependence require a p_T cut of 20 GeV to avoid threshold effects. The structure seen in Figure 6.21 has a dip in efficiency around values of -1 and -2 in ϕ, resulting from a dead region in the detector created by the feet supporting the muon spectrometer.

As discussed in Chapter 4, the end-cap and barrel regions utilize different trigger technologies (TGC and RPC respectively). As seen in Figure 6.20 the muon trigger efficiencies are different in these two regions, with the end-cap having roughly 90% efficiency compared to the barrel's roughly 70%. For this reason, separate histograms of efficiency as a function of p_T for four regions of pseudorapidity were created to serve as efficiency look-up tables in later calculations.

6.5 Efficiency of the Inner Tracker

To measure the efficiency of the inner tracker, the general Tag and Probe method is used in the following fashion: one MuID combined muon (which requires identification with an ID track) is used as the Tag. Then a muon that is found by the muon spectrometer is considered for the Probe. The ATLAS muon data format is such that this requires selecting Probe muons that are either Combined or Standalone but not Tagged.

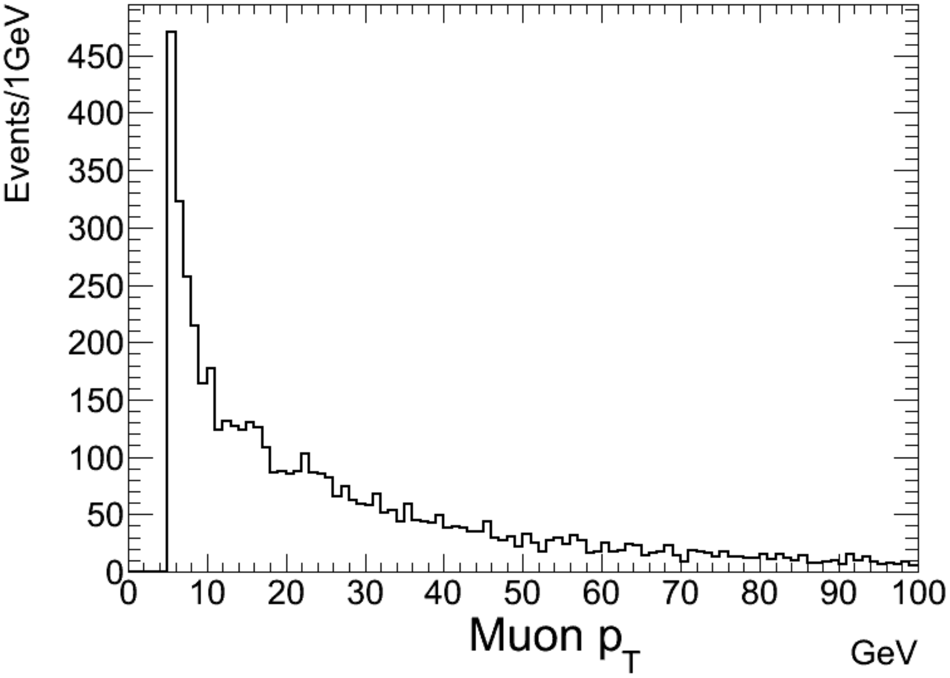

Figure 6.16: Distribution of the muon transverse momentum in the trigger study.

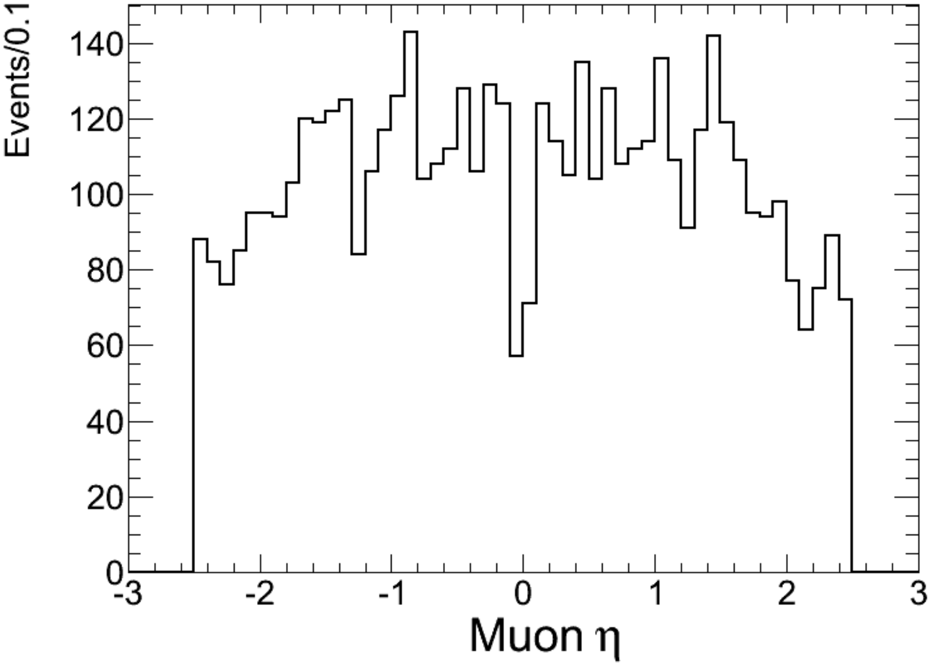

Figure 6.17: Distribution of the muon pseudorapidity in the trigger study.

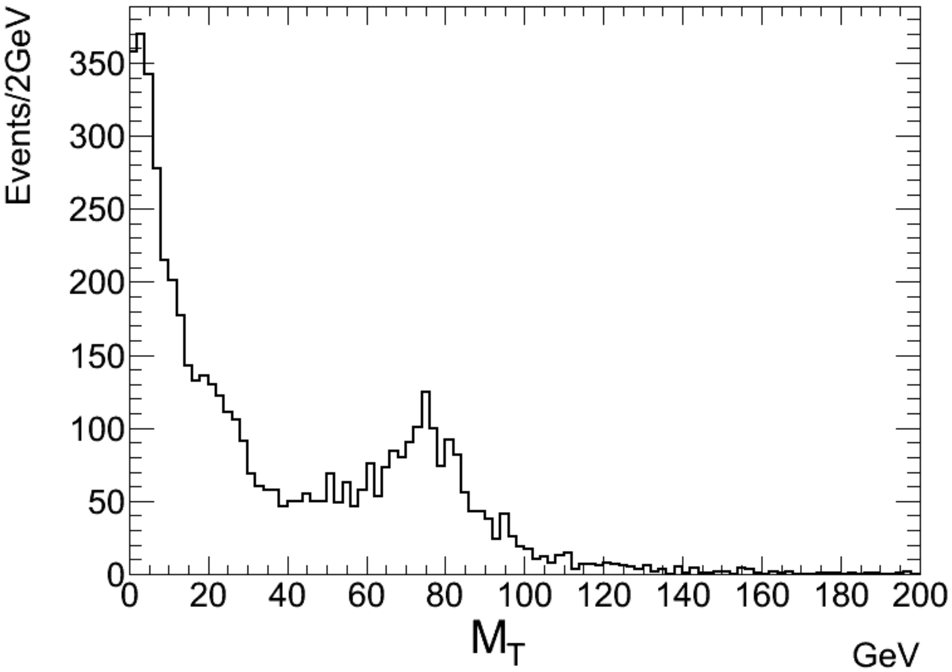

Figure 6.18: Distribution of the transverse mass for the trigger efficiency study. This plot shows a clear peak from W bosons.

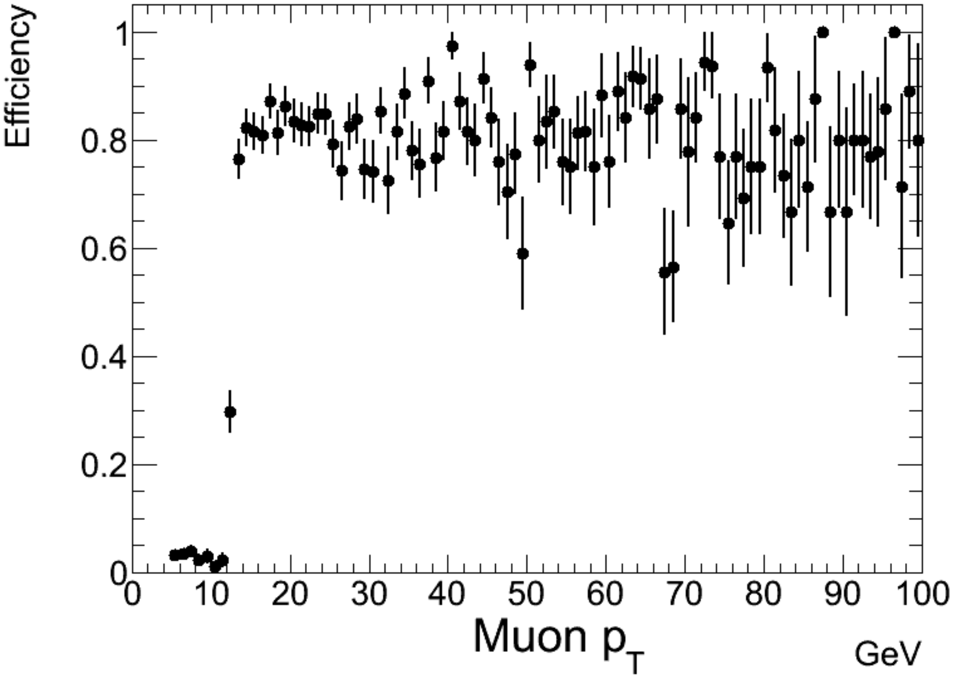

Figure 6.19: Trigger efficiency as a function of muon transverse momentum.

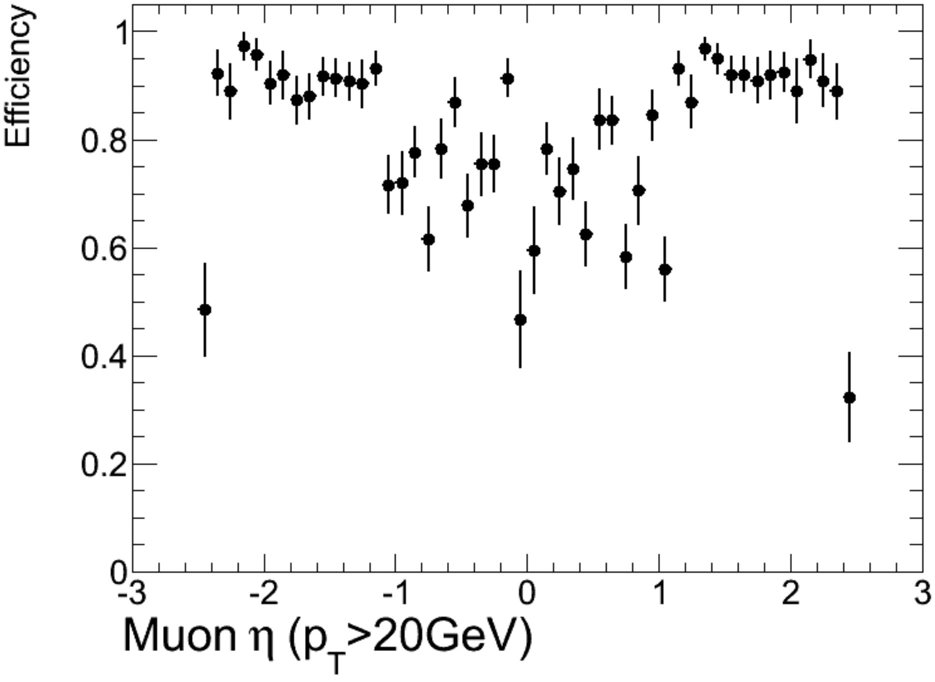

Figure 6.20: Trigger efficiency as a function of muon pseudorapidity.

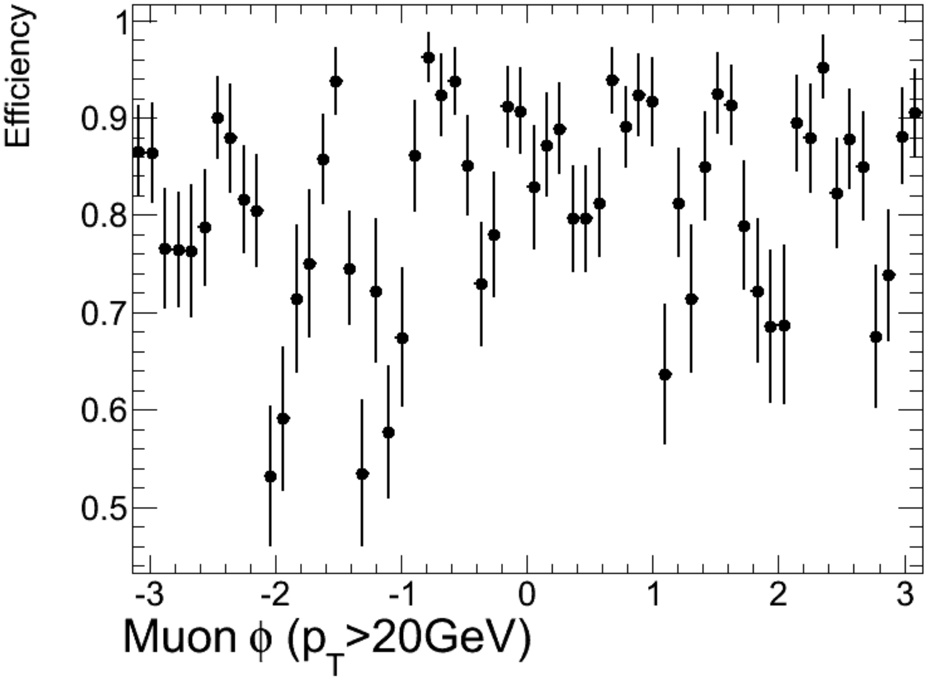

Figure 6.21: Trigger efficiency as a function of muon azimuthal angle.

The Tag is required to be a good, combined MuID muon (satisfying vertex, impact parameter, isolation, and trigger requirements, with $p_T > 20$ GeV and $|\eta| < 2.4$). The Probe muon is required to satisfy impact parameter, isolation requirements, and have $p_T > 5$ GeV and $|\eta| < 2.5$. It must come from either the Combined or Standalone category for the MuID family. Due to extrapolation from the muon spectrometer back to the interaction point, the impact parameters of Standalone muons have a much broader distribution, and the impact parameter cut was loosened from that of the selection analysis to $|d_0| < 10$ mm and $|z_0| < 200$ mm. The pair of muons are then tested to see if they reconstruct to have a dimuon mass between 60 and 120 GeV. If so, they are examined to see whether or not the Probe is matched to an ID track as a Combined muon.

These efficiencies are displayed as functions of p_T and η in Figures 6.22 and 6.23. The pseudorapidity efficiency is plotted for muons with $p_T > 20$ GeV, to minimize threshold effects. For muons in the plateau region, the efficiency of the Inner Detector is found to be 99.9%.

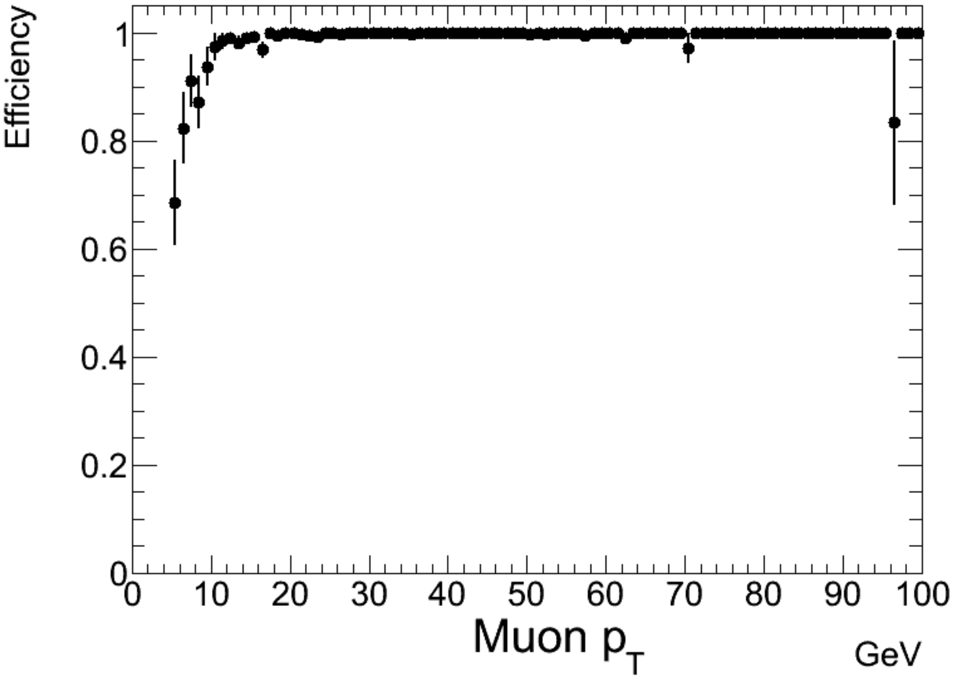

Figure 6.22: Inner detector efficiency as a function of muon transverse momentum.

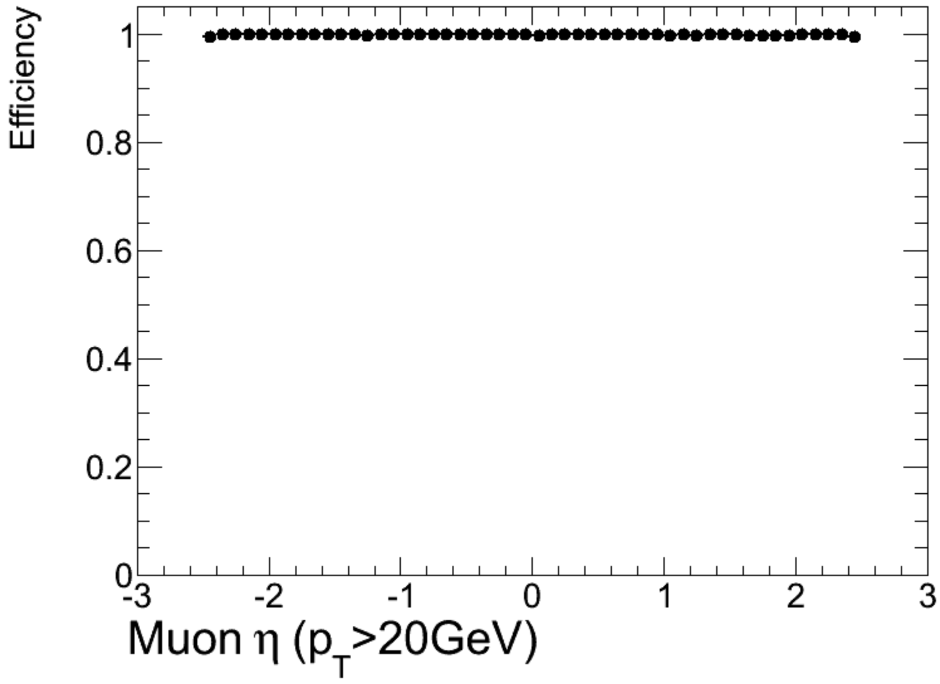

Figure 6.23: Inner detector efficiency as a function of muon pseudorapidity.

6.6 Efficiency of the Muon Spectrometer

To measure the efficiency of the muon spectrometer, the general Tag and Probe method is used in the following fashion: one MuID combined muon (which requires identification with a MS track) is used as the Tag. Then an Inner Detector track is used as the Probe.

The Tag is required to be a good, combined MuID muon (satisfying vertex, impact parameter, isolation, and trigger requirements, with $p_T > 20$ GeV and $|\eta| < 2.4$). The Probe muon is a track from the Inner Detector required to satisfy vertex, impact parameter, isolation requirements, and have $p_T > 5$ GeV and $|\eta| < 2.5$. The Tag muon and Probe track are tested to see if they reconstruct to within 10 GeV of the Z mass, if their difference in azimuthal angle ϕ is greater than 2.0, and if the difference in their impact parameters satisfies $\Delta d_0 < 0.1$ mm and $\Delta z_0 < 1$ mm. If those three conditions are satisfied, the Probe track is examined to see whether or not it is associated with a Combined muon.

These efficiencies are displayed as functions of p_T and η in Figures 6.24 and 6.25. The pseudorapidity efficiency is plotted for muons with $p_T > 20$ GeV, to minimize threshold effects. For muons in the plateau region, the efficiency of the Muon Spectrometer is found to be 94.4% with an absolute statistical uncertainty of 0.8%.

6.7 Efficiency of the Isolation Requirement

To measure the efficiency of the isolation requirement of the muon, the general Tag and Probe method is used in the following fashion: one MuID combined muon that passes isolation requirements is used as the Tag. This Tag muon also must satisfy the vertex, impact parameter, isolation, and trigger requirements, and have $p_T >$ 20 GeV and $|\eta| < 2.4$. For the Probe, a second MuID combined muon with the same requirements is used, except that $p_T > 5$ GeV, $|\eta| < 2.5$, and no isolation requirements are imposed.

These Tag and Probe muons are tested to see if they reconstruct to within 10 GeV of the Z mass, if their difference in ϕ is greater than 2.0, and if the difference in their impact parameters satisfies $\Delta d_0 < 0.1$ mm and $\Delta z_0 < 1$ mm. If those three conditions are satisfied, the Probe muon is examined to see whether or not it is also isolated. The isolation efficiencies are shown in Figures 6.26 and 6.27. The pseudorapidity efficiency is plotted for muons with $p_T > 20$ GeV, to minimize threshold effects. For muons in the plateau region, the efficiency of the isolation requirement is found to be 99.2%.

6.8 Determination of Correction Factor C

The factor C corrects for muon trigger and track reconstruction efficiencies as well as for isolation requirements. This factor is obtained by combining the results of the previous efficiency studies and applying them to the muons in the Z selection search. Since the efficiencies are a function of p_T and η, for each study efficiency look-up tables were produced. These look-up tables were made as a function of transverse momentum and were segmented into different regions of pseudorapidity: one each for end-cap and barrel for positive and for negative pseudorapidities, as described in Section 6.4. The efficiency for each muon is obtained from the appropriate look-up table and the efficiencies are then combined in each event to arrive at the probability that the event would have been triggered and the muons properly reconstructed.

Since there are two muons in the event, either muon can fire the trigger and therefore the overall efficiency for triggering on a dimuon event is:

$$\epsilon^{Trigger} = 1 - (1 - \epsilon^{Trigger}_{LeadMu}) \cdot (1 - \epsilon^{Trigger}_{SubMu}). \tag{6.5}$$

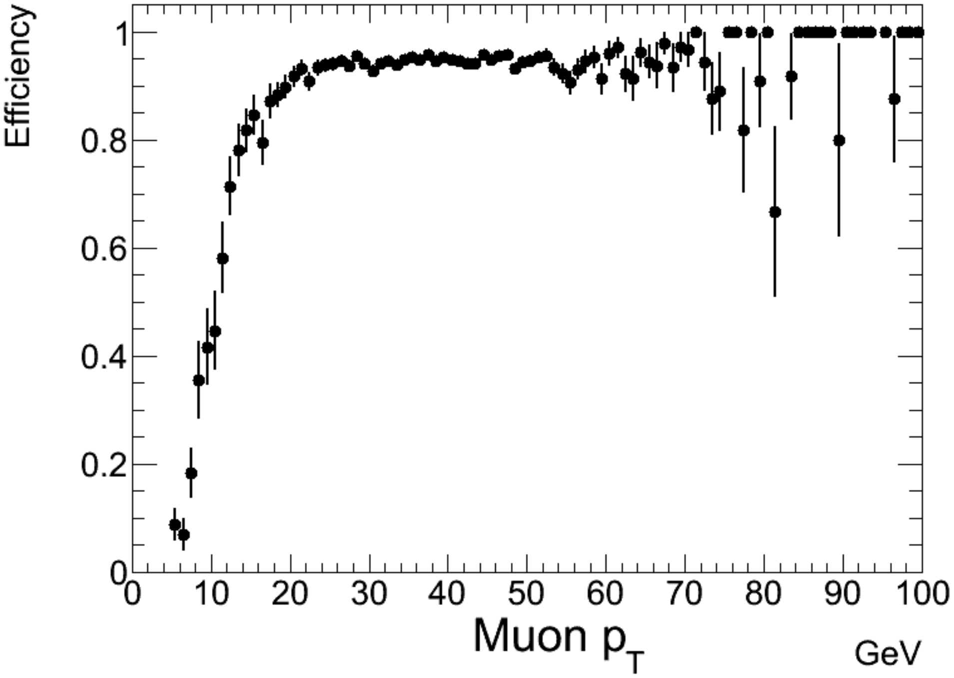

Figure 6.24: Muon spectrometer efficiency as a function of muon transverse momentum.

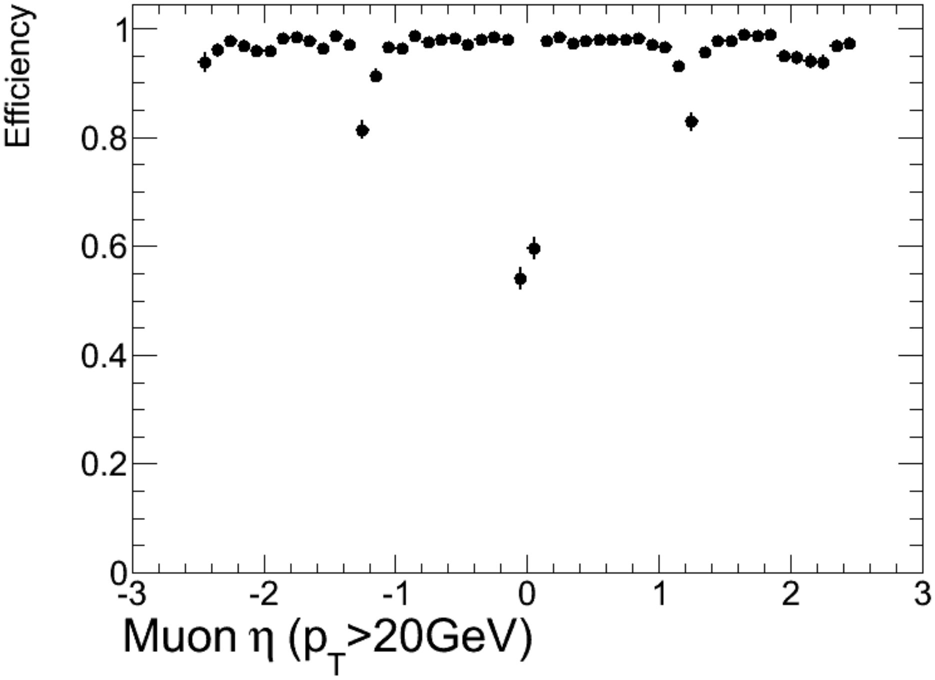

Figure 6.25: Muon spectrometer efficiency as a function of muon pseudorapidity.

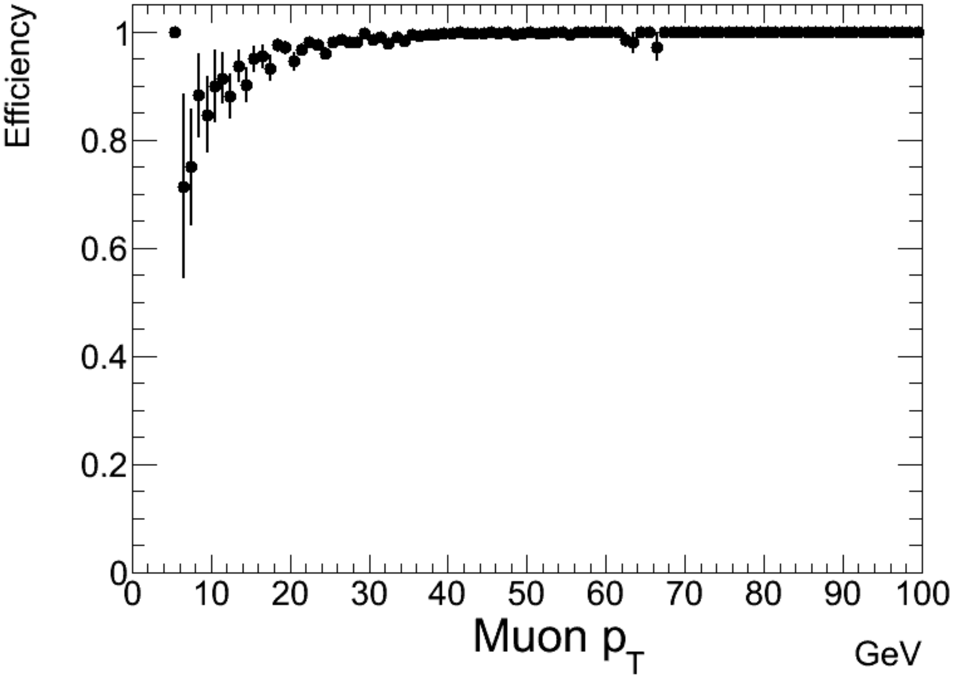

Figure 6.26: Muon isolation efficiency as a function of muon transverse momentum.

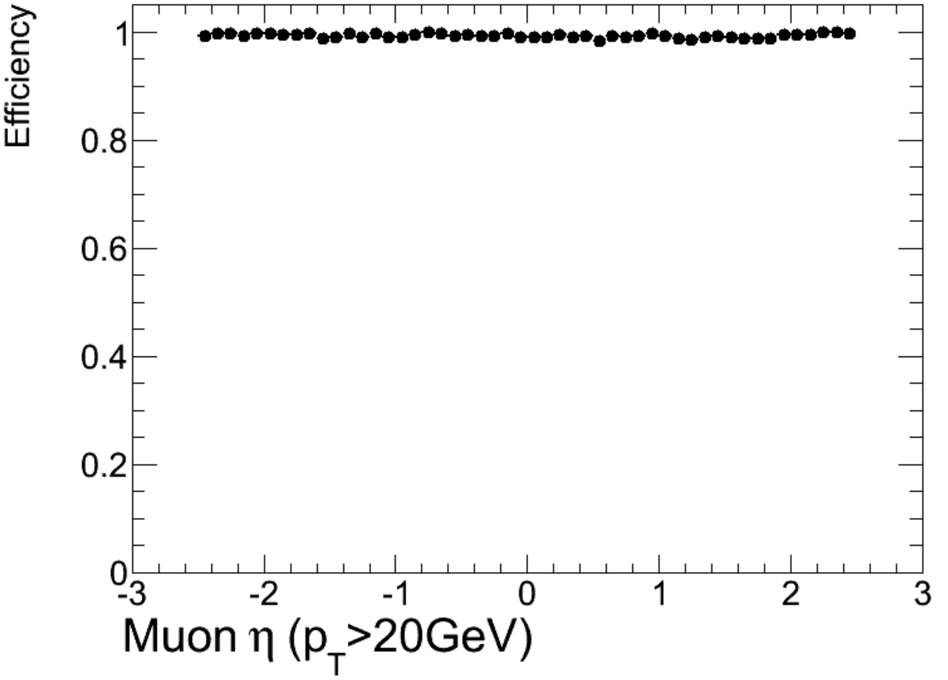

Figure 6.27: Muon isolation efficiency as a function of muon pseudorapidity.

For the other reconstruction efficiencies, the two muons yield additional efficiency factors:

$$\begin{aligned}\epsilon^{ID} &= \epsilon^{ID}_{LeadMu} \cdot \epsilon^{ID}_{SubMu} \qquad (6.6)\\ \epsilon^{MS} &= \epsilon^{MS}_{LeadMu} \cdot \epsilon^{MS}_{SubMu}\\ \epsilon^{Isolation} &= \epsilon^{Isolation}_{LeadMu} \cdot \epsilon^{Isolation}_{SubMu}\end{aligned}$$

and the overall efficiency for any given event is then the combination

$$\epsilon = \epsilon^{Trigger} \cdot \epsilon^{ID} \cdot \epsilon^{MS} \cdot \epsilon^{Isolation}. \qquad (6.7)$$

Histograms of the total efficiency factor for the two sets of kinematic cuts are shown in Figures 6.28 and 6.29. A scatter plot of the efficiency factor vs dimuon mass is shown in Figure 6.30. By definition

$$C = \frac{N_{observed}}{N_{expected}}, \qquad (6.8)$$

where

$$N_{expected} = \sum_{i=1}^{N_{observed}} \frac{1}{\epsilon_i}. \qquad (6.9)$$

There is no way, *a priori*, to know whether a given event will be classified as "signal" or "background" by the fitting procedure. Given the possibility that signal and background events may have slightly different efficiency, we create additional histograms where the dimuon mass entries are stored weighted by $1/\epsilon$ in order to produce plots compensated for detector inefficiencies. The number of signal events obtained from fits to these weighted histograms will be referred to hereafter as $N_{Reweighted}$. This value will replace the role of N/C in Equation 6.3. Figures 6.31 and 6.32 show the mass distributions after reweighting and fitting. The values for $N_{Reweighted}$ are given in Table 6.4, along with the raw number of signal events, N, and their ratio is defined as " $C^{'}$". The original C factor obtained without considering the reweighted histograms is also provided and the differences with $C^{'}$ are slight, below the percent level.

Table 6.4: Efficiency correction factors.

Cuts	**N**	$N_{Reweighted}$	$C^{'}$	**C**
$p_T > 10$ GeV and $\lvert\eta\rvert < 2.5$	17094	21177	0.8072	0.8004
$p_T > 20$ GeV and $\lvert\eta\rvert < 2.4$	14897	17763	0.8387	0.8362

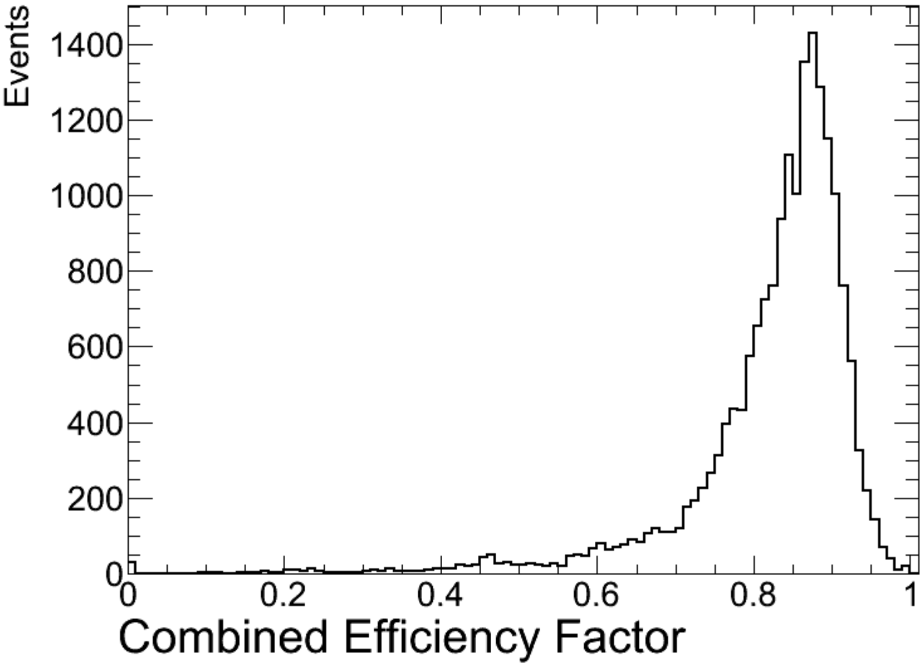

Figure 6.28: Combined efficiency factors when both muons satisfy $p_T > 10$ GeV and $|\eta| < 2.5$.

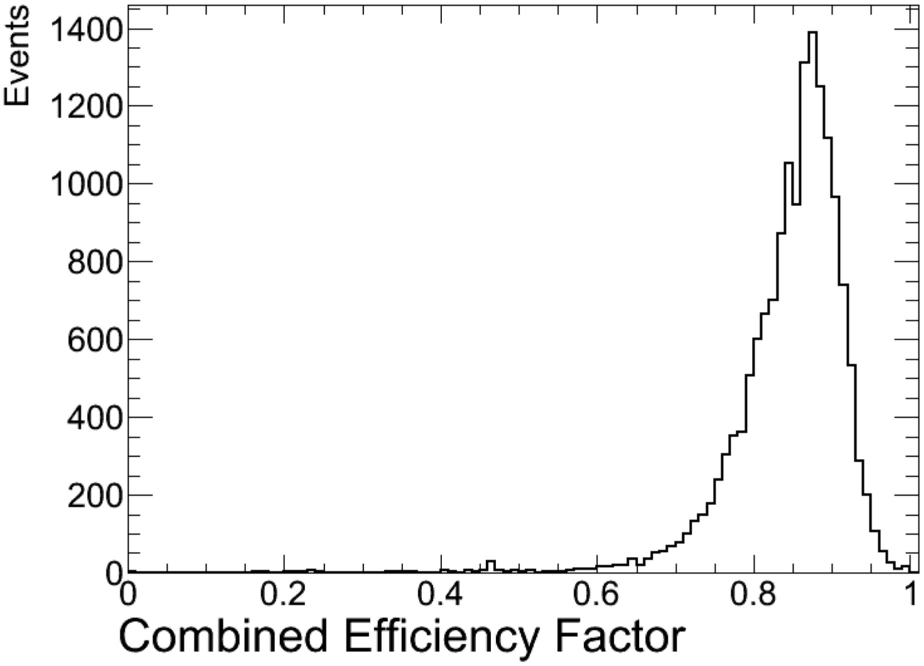

Figure 6.29: Combined efficiency factors when both muons satisfy $p_T > 20$ GeV and $|\eta| < 2.4$.

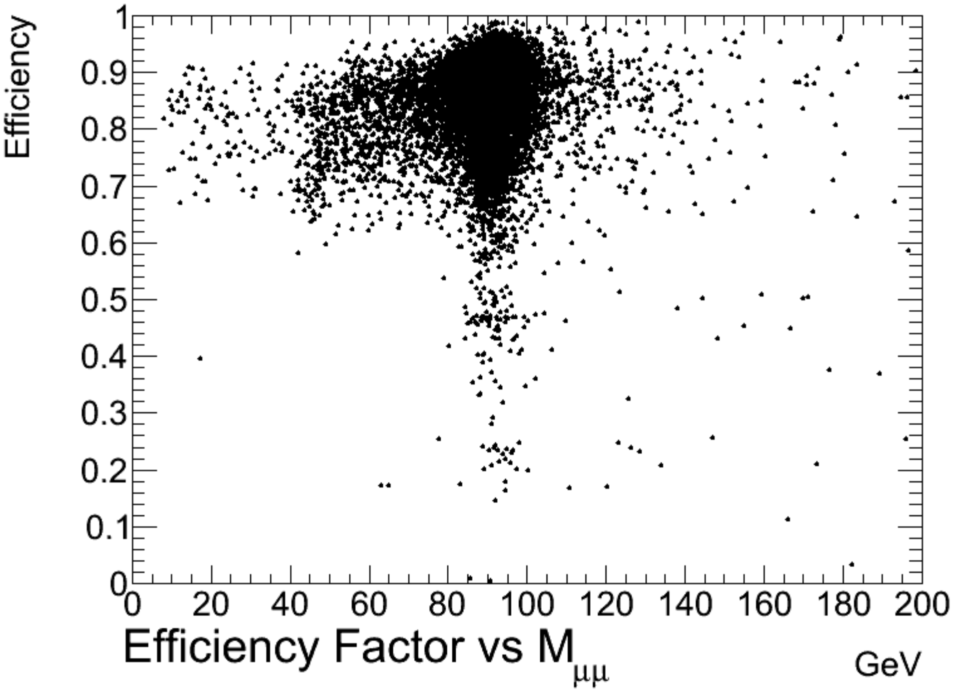

Figure 6.30: Efficiency vs dimuon invariant mass when both muons satisfy $p_T >$ 20 GeV and $|\eta| < 2.4$.

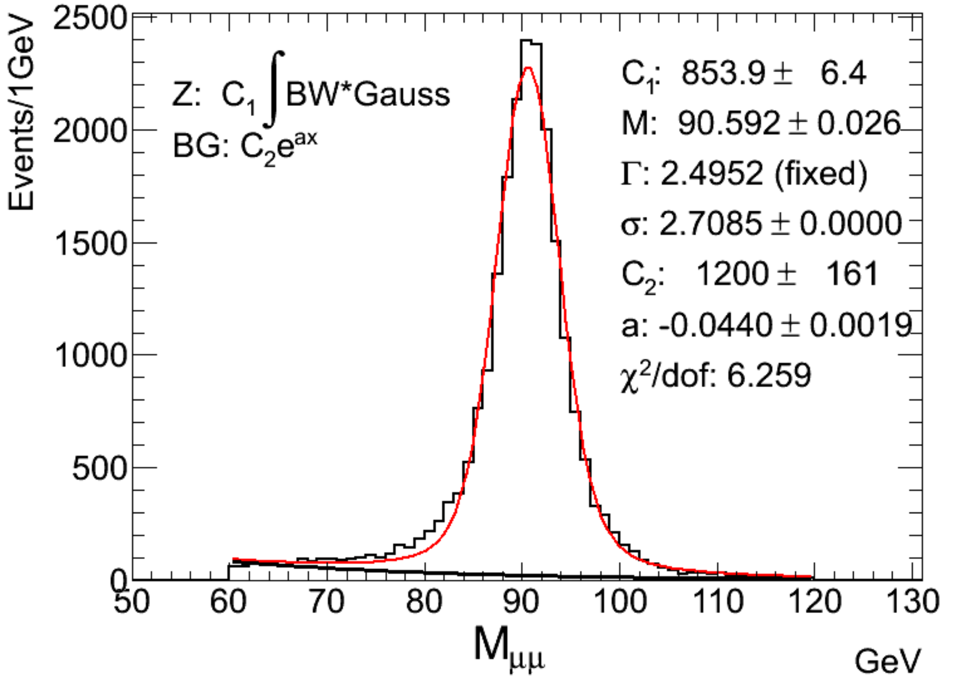

Figure 6.31: Reweighted dimuon invariant mass when both muons satisfy $p_T > 10$ GeV and $|\eta| < 2.5$. In the region $60 < M_{\mu\mu} < 120$ GeV there are 1812 events classified as background leaving 21177 events as signal.

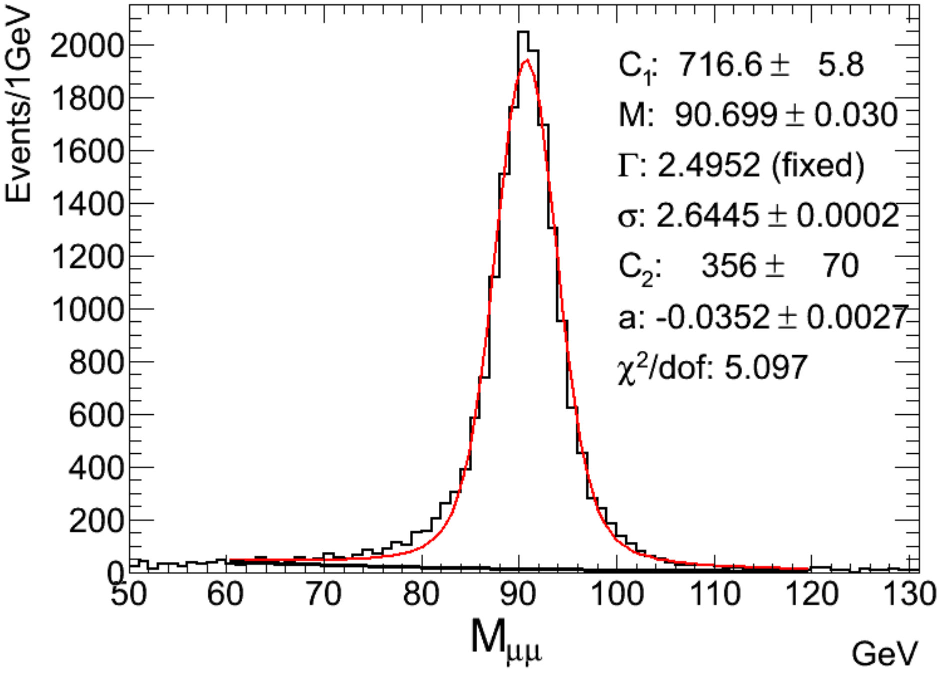

Figure 6.32: Reweighted dimuon invariant mass when both muons satisfy $p_T > 20$ GeV and $|\eta| < 2.4$. In the region $60 < M_{\mu\mu} < 120$ GeV there are 1074 events classified as background leaving 17763 events as signal.

6.9 Determination of Acceptance Factor A

The acceptance factor A must be applied to extrapolate the measured *fiducial* cross-section to the *total* cross-section measured by a perfect detector sensitive to all muons from all Z decays. The only available method for deriving this relies on using Monte Carlo methods that generate events over the full phase space. This factor is given by:

$$A = \frac{N_{FiducialCuts}}{N_{Total}}. \tag{6.10}$$

At the Monte Carlo level, we can separate the Z from the γ^* process directly by choice of generator options. To calculate the A factor we use samples of Z-only events with final-state radiation applied. In this case it is no longer necessary to perform a fit to remove the background, and we can simply use the number of events in the mass window under consideration. Figure 6.33 shows the invariant mass of the two muons for all ranges of generated p_T and η, and the number of events in our mass window, 651120, serves as the denominator in Equation 6.10. Figures 6.34 and 6.35 are for our two choices of kinematic cuts, and the event numbers, 366333 and 313854, are the numerators for the A factor for the $p_T > 10$ GeV $|\eta| < 2.5$ and $p_T > 20$ GeV $|\eta| < 2.4$ sets respectively.

Two Monte Carlo generators were used for determining A, Pythia and MC@NLO. We summarize all A-factor results in Table 6.5. The difference between generators is 1.5% which provides an estimate of the uncertainty on the measurement of the total cross-section. The results from the Pythia study will be taken as the central value, since this Monte Carlo program was used more extensively in other studies of this thesis.

Table 6.5: Acceptance correction factors.

Cuts	**N**	**A**
Pythia		
No p_T or η cuts	651120	
$p_T > 10$ GeV and $\|\eta\| < 2.5$	366333	0.5626
$p_T > 20$ GeV and $\|\eta\| < 2.4$	313854	0.4820
MC@NLO		
No p_T or η cuts	3775696	
$p_T > 10$ GeV and $\|\eta\| < 2.5$	2090486	0.5537
$p_T > 20$ GeV and $\|\eta\| < 2.4$	1791707	0.4745

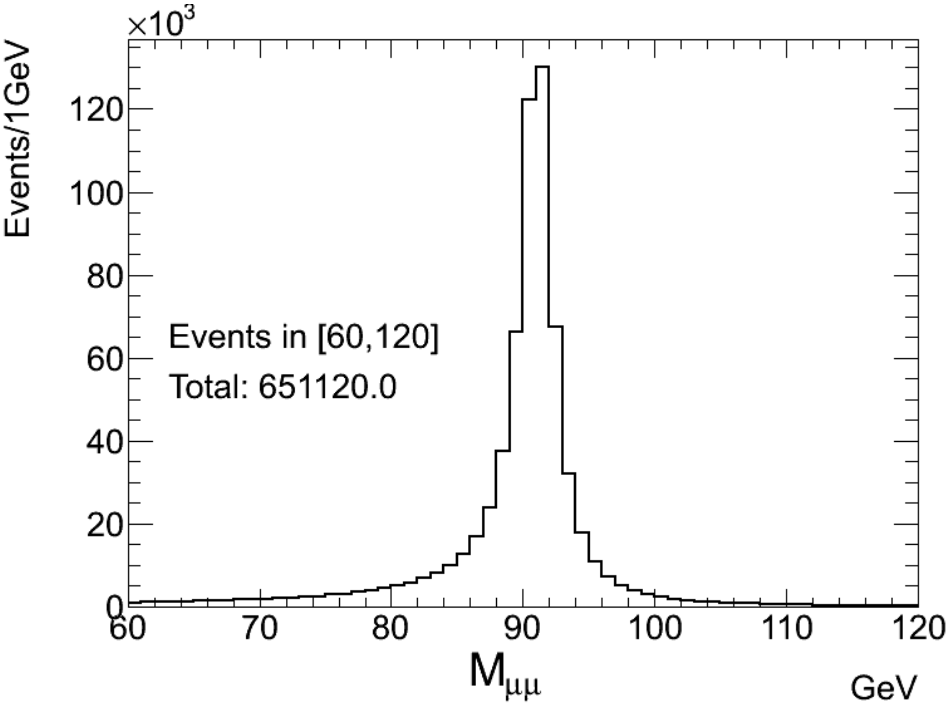

Figure 6.33: Dimuon invariant mass distribution for all Pythia "truth" events. The sample is for Z-Only events with final-state radiation included.

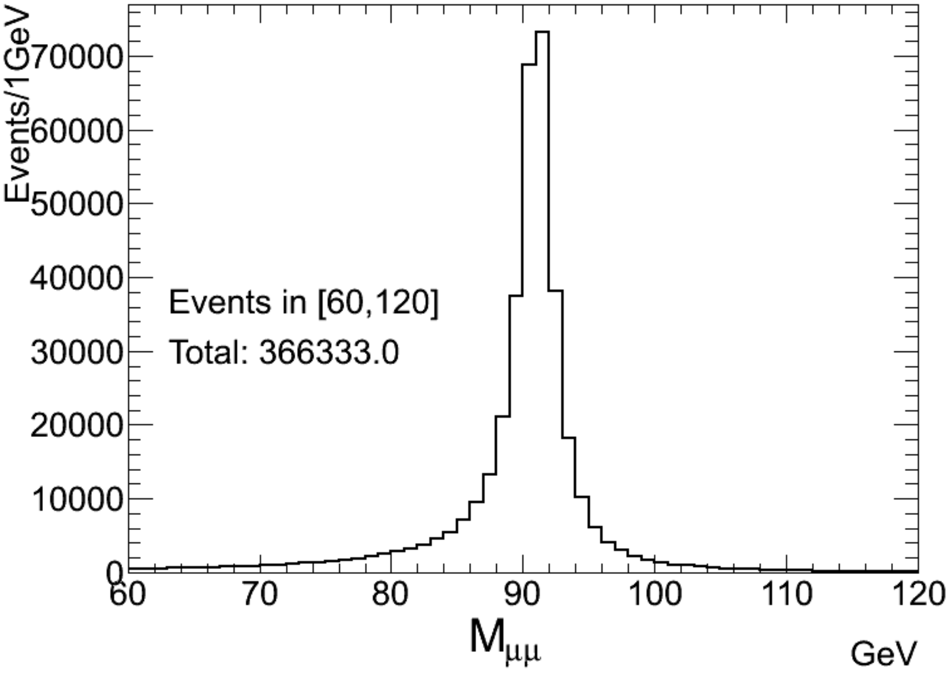

Figure 6.34: Dimuon invariant mass distribution for Pythia "truth" events when both muons satisfy $p_T > 10$ GeV and $|\eta| < 2.5$. The sample is for Z-Only events with final-state radiation included.

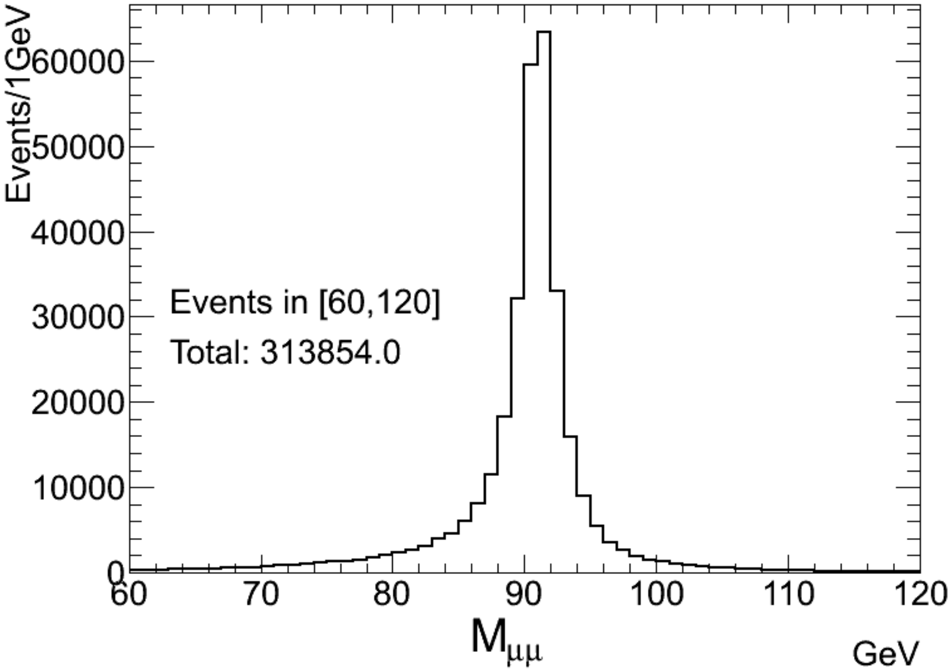

Figure 6.35: Dimuon invariant mass distribution for Pythia "truth" events when both muons satisfy $p_T > 20$ GeV and $|\eta| < 2.4$. The sample is for Z-Only events with final-state radiation included.

6.10 Luminosity

The data analyzed for this thesis were originally calculated to correspond to 41740 nb^{-1} of integrated luminosity when using the official ATLAS luminosity calculator [52]. However, the luminosity working group has recently improved the luminosity measurement, resulting in the decision to scale down the integrated luminosity values by a factor of 0.964 [53]. This results in an actual value for the luminosity of 40237 nb^{-1}, which is used in all cross-section calculations.

6.11 Final-State Radiation

As mentioned previously, the fitting function used for the signal does not model final-state radiation (FSR), and thus part of the radiative tail of real Z events will be erroneously labeled as a contribution to the background. To correct for this, we introduce one further correction factor not included explicitly in Equation 6.3. By examining Monte Carlo events generated where the γ^* contributions have been turned off but where FSR has been included, the total number of events within the mass range considered is *actually* the signal, though some of it will be fitted as background. We thus derive the following correction factor:

$$F = \frac{N_{\text{“}Signal\text{”}} + N_{\text{“}Background\text{”}}}{N_{\text{“}Signal\text{”}}}, \tag{6.11}$$

which relates the actual expected signal to that labeled “signal” after the background subtraction procedure. In the cross-section calculations we then will need to apply this factor to our value of N. Figures 6.36 and 6.37 show the mass plots used to determine F, with the results summarized in Table 6.6. We note that the fitted values of M_Z are slightly below the official value of 91.188 GeV as a result of not taking into account the radiative tail when fitting the signal.

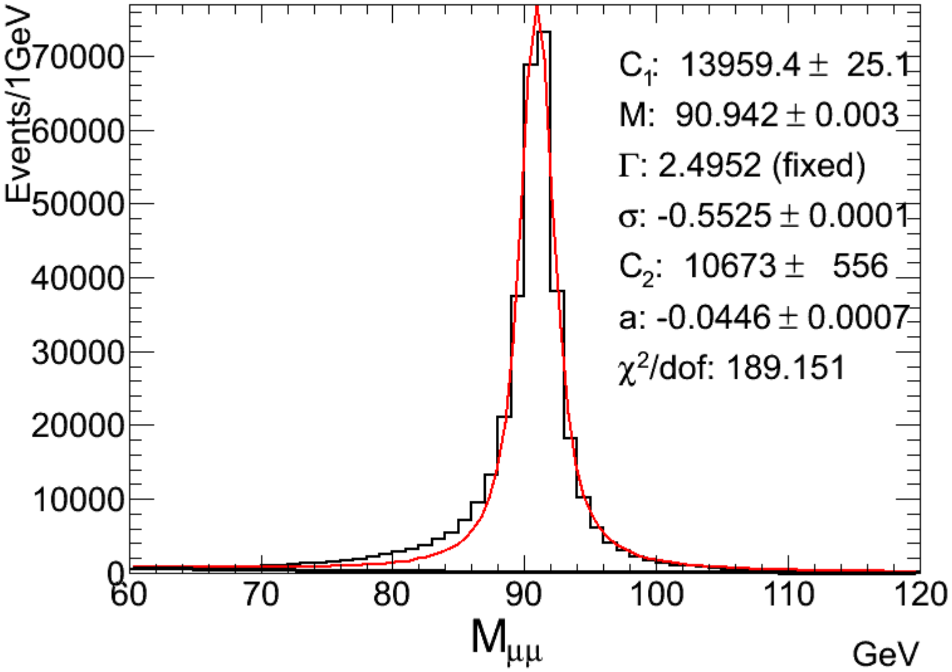

Figure 6.36: Fitted dimuon invariant mass distribution for PYTHIA “truth” events when both muons satisfy $p_T > 10$ GeV and $|\eta| < 2.5$. The sample is for Z-Only events with final-state radiation included. In the region $60 < M_{\mu\mu} < 120$ GeV there are 15291 events classified as background leaving 351042 events as signal.

Table 6.6: Final-state radiation correction factors

Cuts	N_{Tot}	$N_{\text{“}Z\text{”}}$	**F**
$p_T > 10$ GeV and $\lvert\eta\rvert < 2.5$	366333	351042	1.044
$p_T > 20$ GeV and $\lvert\eta\rvert < 2.4$	313854	304709	1.030

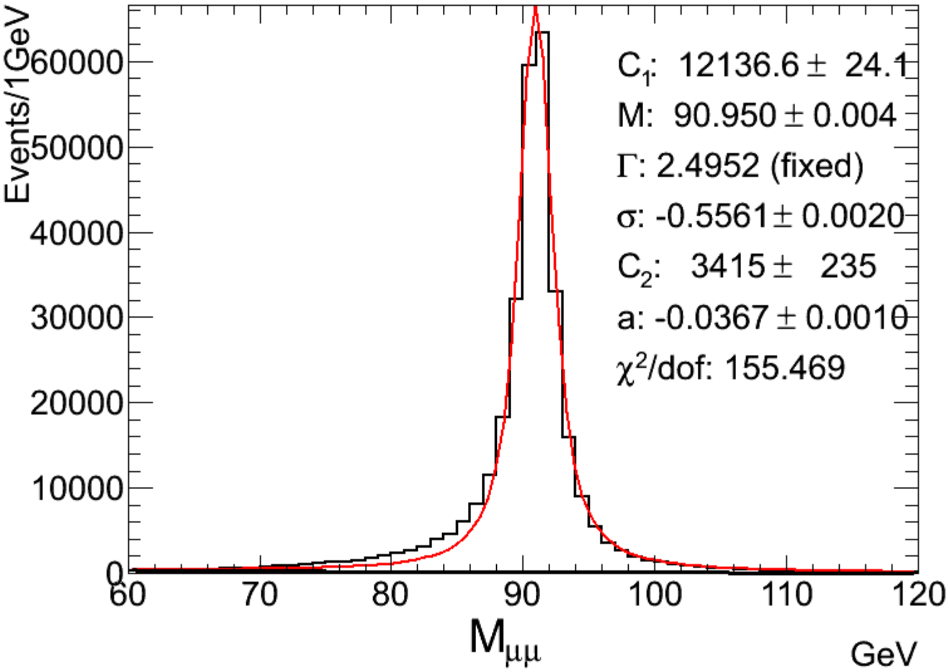

Figure 6.37: Fitted dimuon invariant mass distribution for Pythia "truth" events when both muons satisfy $p_T > 20$ GeV and $|\eta| < 2.4$. The sample is for Z-Only events with final-state radiation included. In the region $60 < M_{\mu\mu} < 120$ GeV there are 9145 events classified as background leaving 304709 events as signal.

6.12 Background Consistency Test

To demonstrate that the F factor makes sense, as well as to put a limit on the size of backgrounds from other sources, we perform the following exercise. Monte Carlo samples were produced consisting solely of the Z resonance as in the previous sections. In addition, the Pythia generator was also run to produce a sample of combined Z/γ^*, including all contributions from interference effects. Through a comparison of the two we can estimate the size of the contribution to background due to γ^*. The Monte Carlo samples were normalized so that the generated integrated luminosity matches the integrated luminosity in our data sample. The F factor is used to derive an estimate of the size of the background contribution due to the mislabeling of final-state radiation Z events as background. Together these two effects should comprise most of the background, with a small contribution left over arising from QCD or other background sources.

We apply this analysis to the data with both muons having $p_T > 20$ GeV and $|\eta| < 2.4$. Figure 6.38 gives a Z-only contribution of 455 events, and Figure 6.39 has 928 events for the combined Z/γ^*, which by process of elimination yields a contribution due to all γ^* effects of 473 events.

The data, corrected for detector reconstruction efficiencies as shown in Figure 6.32, gave a fitted background of 1074 and an estimated signal ($N_{Reweighted}$) of 17763. Using Equation 6.11, $(F-1)N_{\text{``}Signal\text{''}} = N_{\text{``}Background\text{''}}$, we conclude that 533 of the fitted background events are Z signal events with final-state radiation. Assuming the Monte Carlo accurately models the situation, 473 events are attributed to γ^* contributions, leaving 68 events classified as other "background". For the 17763 signal events in the mass window, this is a 0.38% background. An ATLAS working group performed a data-driven study on background from QCD events, and found 66 ± 21 background events for a signal size of 11669 [54] (their sample used less integrated luminosity). This is similar to the background observed here. We conclude that our treatment of the background and our procedures for handling its effects on the cross-section measurement are well understood.

6.13 Calculation of Cross-Section

Based on the work described above, we now present two cross-section measurements for the process $pp \to (Z \to \mu^+\mu^-) +$ anything at a center of mass collision energy of 7 TeV, where the dimuon mass interval is restricted to the range from 60 to 120 GeV.

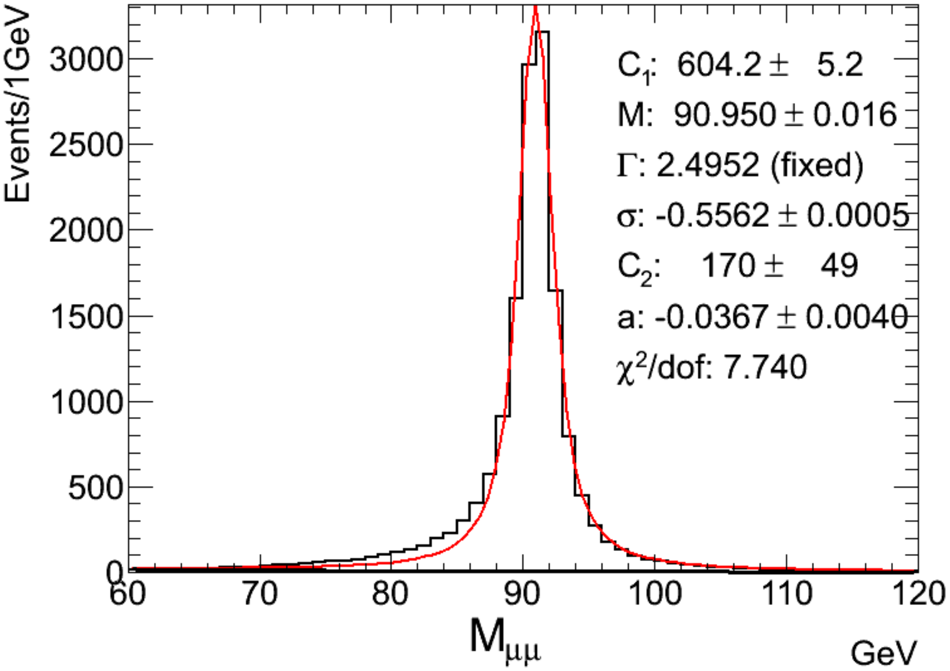

Figure 6.38: Scaled dimuon invariant mass distribution for Pythia "truth" events when both muons satisfy $p_T > 20$ GeV and $|\eta| < 2.4$. The sample is for Z-Only events with final-state radiation included. The number of MC events is normalized to the integrated luminosity of the data. In the region $60 < M_{\mu\mu} < 120$ GeV there are 455 events classified as background leaving 15170 events as signal.

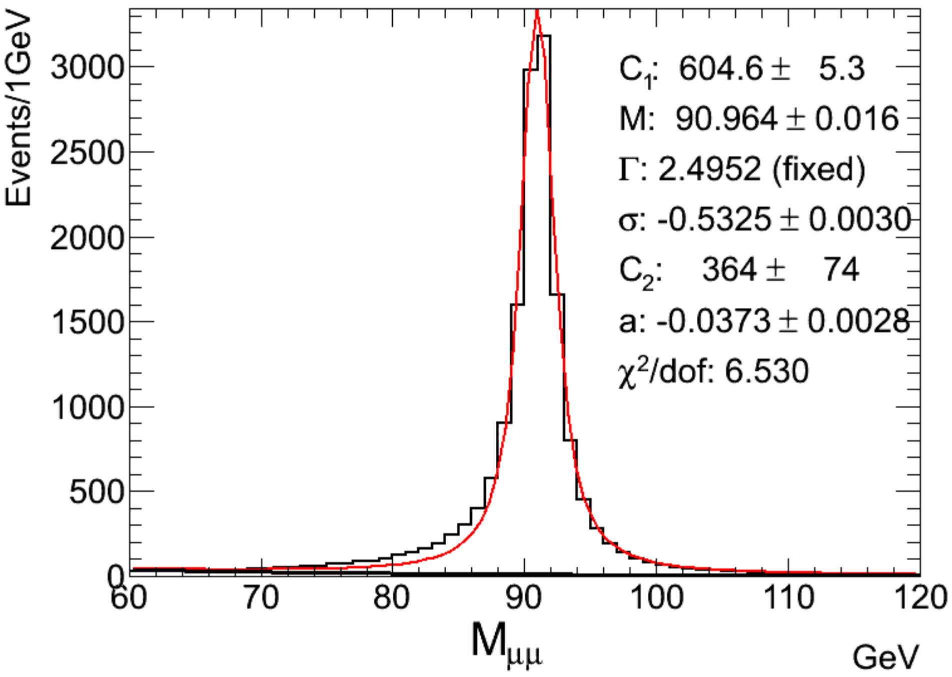

Figure 6.39: Scaled dimuon invariant mass distribution for Pythia "truth" events when both muons satisfy $p_T > 20$ GeV and $|\eta| < 2.4$. The sample is for Z/γ^* events with final-state radiation included. The number of MC events is normalized to the integrated luminosity of the data. In the region $60 < M_{\mu\mu} < 120$ GeV there are 928 events classified as background leaving 15113 events as signal.

The first of these is the fiducial cross-section σ_{fid} (multiplied by the branching ratio to muons) defined by:

$$\sigma_{fid} \times BR_{\mu\mu} = \frac{N_{Reweighted} \cdot F}{L}, \tag{6.12}$$

where $N_{Reweighted}$ is the number of $Z \to \mu^+\mu^-$ signal events corrected for trigger, muon reconstruction, and isolation efficiencies. The second is the total cross-section σ_{tot} defined by:

$$\sigma_{tot} = \frac{\sigma_{fid}}{A}, \tag{6.13}$$

where A is the kinematic acceptance factor that corrects for the limited ranges of transverse momentum p_T and pseudorapidity η of the σ_{fid} measurement.

For both σ_{fid} and σ_{tot} we present results for two sets of muon kinematic requirements, ($p_T > 10$ GeV, $|\eta| < 2.5$) and ($p_T > 20$ GeV, $|\eta| < 2.4$), imposed on both muons. While σ_{fid} will clearly differ for the two cases, we would expect the derived value for σ_{tot} to be the same in both cases. All of the relevant factors are presented in Table 6.7.

For the $p_T > 10$ GeV and $|\eta| < 2.5$ case the cross-sections are found to be

$$\sigma_{fid} \times BR_{\mu\mu} = \frac{N_{Reweighted} \cdot F}{L} = 0.550 \pm 0.023 \text{ nb} \tag{6.14}$$

$$\sigma_{tot} \times BR_{\mu\mu} = \frac{N_{Reweighted} \cdot F}{A \cdot L} = 0.977 \pm 0.047 \text{ nb} \tag{6.15}$$

while for the $p_T > 20$ GeV and $|\eta| < 2.4$ case the results are

$$\sigma_{fid} \times BR_{\mu\mu} = \frac{N_{Reweighted} \cdot F}{L} = 0.455 \pm 0.017 \text{ nb} \tag{6.16}$$

$$\sigma_{tot} \times BR_{\mu\mu} = \frac{N_{Reweighted} \cdot F}{A \cdot L} = 0.943 \pm 0.041 \text{ nb} \tag{6.17}$$

where the determination of the uncertainties of these cross-section measurements is described in Section 6.14.

Table 6.7: Cross-section correction factors.

Cuts	$N_{Reweighted}$	**F**	**A**	**L**
$p_T > 10$ GeV and $|\eta| < 2.5$	21177	1.044	0.5626	40237
$p_T > 20$ GeV and $|\eta| < 2.4$	17763	1.030	0.4820	40237

6.14 Cross-Section Measurement Uncertainties

This section addresses the uncertainties of the cross-section measurements. Statistical and systematic uncertainties are treated and reported separately for each of the main factors (N, L, A, F, C) that contribute to the cross-section measurements. These factors are essentially independent, and their errors will be summed in quadrature. The results of these studies are summarized in Table 6.8, with the details elaborated in the following subsections.

Table 6.8: Uncertainties of cross-section correction factors.

Factor	**Central Value**	**Statistical Uncertainty**	**Systematic Uncertainty**	**Combined Uncertainty**
For $p_T > 10$ GeV and $\|\eta\| < 2.5$				
N	17094	0.76%	0.60%	0.97%
L	40237	<0.1%	3.4%	3.4%
A	0.5626	0.11%	2.26%	2.26%
F	1.044	0.06%	0.15%	0.16%
C	0.8072	0.80%	2.10%	2.25%
For $p_T > 20$ GeV and $\|\eta\| < 2.4$				
N	14892	0.82%	0.37%	0.90%
L	40237	<0.1%	3.4%	3.4%
A	0.4820	0.13%	2.27%	2.27%
F	1.030	0.06%	0.15%	0.16%
C	0.8387	0.99%	0.40%	1.07%

6.14.1 Uncertainty of N

The statistical uncertainty of the number of observed signal events is given by the usual Gaussian $\sqrt{N}$ statistics, given our sample size. The systematic uncertainty of N derives primarily from the uncertainty in the determination of the background under the Z signal peak.

To estimate the systematic uncertainty in the background we investigate contributions introduced by our choice of functional form for the expected background. Our choice of an exponential background function was motivated by the general shape of the γ^* distribution, however, other choices of background shapes can give comparable chi-squared values. To estimate the error associated with choice of background shape, we have also examined a linearly decreasing background. The fraction of mislabeled background due to FSR will also depend on background shape assumptions. The uncertainty on the combined value of N·F due to different background functional forms was found to be 0.37% for the case of muons with $p_T > 20$ GeV and $|\eta| < 2.4$, and 0.60% for the muons with $p_T > 10$ GeV and $|\eta| < 2.5$.

6.14.2 Uncertainty of FSR Factor F

The methods for determining the correction factor F involve the same fitting techniques used for deriving the number of signal events N. Therefore the systematic errors for F and N associated with the functional forms of the fits are correlated and have been combined in the systematic error for N as described above. An additional systematic uncertainty considered here is the uncertainty quoted for the PHOTOS program that interfaces FSR with the Pythia generator. By comparing the results of the PHOTOS approach with another generator using matrix elements, for the $Z \to \mu\mu\gamma$ process, the PHOTOS authors report an overall 0.15% uncertainty in the shape of the dimuon mass spectrum [55]. As this is negligible compared to other errors, it is simply taken as a conservative estimate on the uncertainty in the factor F.

The statistical uncertainty of the correction factor F is derived from the uncertainty of the fitted background. The uncertainties of the fit parameters are the chief contributors. However, since C_2 and a are correlated, we must use the following formula for error propagation [56]

$$\delta_{N_B} = \sqrt{(\frac{\partial N_B}{\partial C_2}\sigma_{C_2})^2 + (\frac{\partial N_B}{\partial a}\sigma_a)^2 + 2\frac{\partial N_B}{\partial C_2}\frac{\partial N_B}{\partial a}\sigma_{C_2a}}, \tag{6.18}$$

where σ_{C_2} and σ_a are the standard deviations for C_2 and a respectively, and σ_{C_2a} is the covariance of C_2 and a, as given by the fitting program. While varying either of the parameters individually by their quoted errors would have yielded an uncertainty on F of $\sim 0.2\%$, the correct treatment of the large anti-correlation of the fit parameters results in an uncertainty of 0.06% for both choices of kinematic cuts.

6.14.3 Luminosity Uncertainty

The ATLAS luminosity working group has performed a detailed and dedicated analysis of the uncertainty of the integrated luminosity measurement, independent of any given physics analysis. The published result for this uncertainty is ±3.4% [53].

6.14.4 Uncertainty of Acceptance Factor A

As discussed in Section 6.9, we have calculated the acceptance factor A using the Pythia and MC@NLO generators. We used the Pythia result in computing total cross-sections and take the 1.58% (1.56%) difference with respect to the MC@NLO value for A for choice of kinematic cuts of $p_T > 10$ GeV and $|\eta| < 2.5$ ($p_T > 20$ GeV and $|\eta| < 2.4$) as one source of systematic uncertainty for A.

In addition we have considered the effect of the choice of PDF sets used by the generator, and also the variation of the internal PDF parameters about their defaults. The Les Houches Accord PDF Interface (LHAPDF) [57] is used to vary both the PDF sets and their internal parameters to determine the effects that a particular choice of set and default parameters has on the calculation of the acceptance factor A.

The CTEQ PDF set has 22 eigenvectors that define the set. We determine A for PDF sets where the value of one of the eigenvectors has been varied up or down by the tolerance results. Doing this for all eigenvectors separately generates 44 PDF sets in addition to the set for the central value. Letting the value for the acceptance calculated using the PDF sets associated with varying the eigenvector up by the tolerance be denoted by A_i^+, and those based on the sets where it has been varied down by A_i^-, the systematic uncertainty relative to the central value A_0 is then given by the following formula [58]:

$$\delta = \frac{\sqrt{\Sigma(A_i^+ - A_0)^2} + \sqrt{\Sigma(A_i^- - A_0)^2}}{2 \cdot A_0}. \tag{6.19}$$

The result is a systematic error of 1.61% due to PDF uncertainties based on variation about the central value when considering the fiducial region for muons with $p_T > 10$ GeV and $|\eta| < 2.5$. The uncertainty is 1.65% for $p_T > 20$ GeV and $|\eta| < 2.4$. These uncertainties are added in quadrature with the uncertainty associated with choice of generator to give the 2.26% (2.27%) uncertainties shown in Table 6.8.

We compute the statistical uncertainty on A due to the MC sample size to be 0.11% (0.13%).

6.14.5 Uncertainty of Efficiency Factor C

For the uncertainty on C, we combine the uncertainties for each of the efficiency measurements. The statistical uncertainty for the efficiencies derived from Tag and Probe is correlated with the statistical uncertainty on the number of signal events N as the same muon data stream provided the events for both. However the trigger study was performed on an independent sample, and the contributions to the statistical uncertainty of the correction factor C from this sample were calculated to be 0.99% when muons were required to have $p_T > 20$ GeV and $|\eta| < 2.4$ and 0.80% with $p_T > 10$ GeV and $|\eta| < 2.5$. Systematic uncertainties for each of the efficiency measurements were studied through cut variations and finally combined for an overall systematic error on C.

For the Tag and Probe studies, one potential source of systematic uncertainty is a background of non-Z decay dimuons where one of the muons is a "fake". We adjust the applied cuts to increase and decrease the purity of the sample, observing the effect this has on the efficiency measurement, and take this as a contribution to the uncertainty.

For brevity, we give details for the case with muon $p_T > 20$ GeV and $|\eta < 2.4$. We also give final results for the other fiducial choice of $p_T > 10$ GeV and $|\eta| < 2.5$. For the MS and Isolation efficiencies, we have redone the computations without the $\Delta\phi$, Δd_0, and Δz_0 requirements on the Tag and Probe tracks. For the average MS efficiency this amounts to a 0.19% effect, while for the Isolation efficiency it is a 0.03% effect.

For the ID efficiencies, we have varied the Z mass window cut. This yields a 0.04% variation compared to the original cut.

For the trigger studies, we varied the MET cut that preferentially selected for muons from W decay. For Periods 2 through 4 this has between a 0.3% and 0.6% effect, while for Period 1 the effect is 2.4%. Taking the average of percent uncertainty in the trigger efficiency across the periods, with weighting performed according to the integrated luminosity, the total uncertainty due variations in cut requirements is seen to be 0.5%.

To combine all of these individual systematic effects on efficiencies into an overall systematic error on C we refer to its definition in Equations 6.8 and 6.9, and take the ϵ_i to be the total efficiency factors calculated when both muons are reconstructed at their average efficiency rate, so that $C = \epsilon_{Avg}$. We then apply the general formula for error propagation:

$$\delta\epsilon_{Avg} = \sqrt{\Sigma(\frac{\partial\epsilon_{Avg}}{\partial\epsilon^{type}}\delta\epsilon^{type})^2} \tag{6.20}$$

where the ϵ^{type} range over $\epsilon^{Trigger}, \epsilon^{ID}, \epsilon^{MS}$, and $\epsilon^{Isolation}$. Again taking the efficiency for both the individual muons at its average value, the uncertainty of the combined efficiency for each type is computed and the final value of the uncertainty for C is found to be 0.4%. For the other fiducial region, $p_T > 10$ GeV and $|\eta| < 2.5$, the final value on the uncertainty for is 2.1%, where the increase is due entirely to contributions from the trigger efficiencies. Since the trigger coverage only extends to 2.4 in $|\eta|$ and since the trigger thresholds for periods 3 and 4 are at 13 GeV this is not an unreasonable result.

6.14.6 Overall Cross-Section Uncertainty

The overall uncertainty of the fiducial cross-section measurement is a combination of the uncertainties on N, L, C, and F. For the choice of fiducial region defined by muons with $p_T > 10$ and $|\eta| < 2.5$ summing these contributions in quadrature yields a final uncertainty of 4.2% on σ_{fid}. Extrapolating this to the total cross-section requires the acceptance factor A and its associated uncertainty, bringing the uncertainty of σ_{tot} to 4.8%. The measurements for the other kinematic cuts, $p_T > 20$ and $|\eta| < 2.4$, have uncertainties of 3.7% on σ_{fid} and 4.3% on σ_{tot}. A breakdown of the uncertainties into the categories of statistical, systematic, and luminosity for each measurement is provided in Table 6.9.

Table 6.9: Final cross-section uncertainties.

Measurement	**Statistical Uncertainty**	**Systematic Uncertainty**	**Luminosity Uncertainty**	**Total Uncertainty**
For $p_T > 10$ GeV and $|\eta| < 2.5$				
$\sigma_{fid} \times BR_{\mu\mu}$	1.1%	2.2%	3.4%	4.2%
$\sigma_{tot} \times BR_{\mu\mu}$	1.1%	3.2%	3.4%	4.8%
For $p_T > 20$ GeV and $|\eta| < 2.4$				
$\sigma_{fid} \times BR_{\mu\mu}$	1.3%	0.6%	3.4%	3.7%
$\sigma_{tot} \times BR_{\mu\mu}$	1.3%	2.3%	3.4%	4.3%

6.15 Comparison with ATLAS Working Group Result

The ATLAS Standard-Model working groups have also been analyzing the data, and an official cross-section paper for the W and Z signatures has been prepared [54]. For comparison purposes the analysis has been repeated mimicking their selection criteria, though using different run periods and a different *Good Run List* (GRL).

The major differences in selection criteria are that the ATLAS working group imposes two additional rejection criteria, one on jets/MET and one on muon quality. The cut on jets/MET was a jet cleaning requirement that analyzed three different aspects of the jet calorimetry reconstruction and rejected events with "bad jets" in them. Bad jets were defined as jets that: possessed a large energy-squared-weighted cell timing (> 50 ns), if predominately composed of activity in the hadronic end-cap calorimeter (HEC fraction > 0.8) had their energy concentrated in only a few calorimeter cells (90% of the energy in 5 cells or less), or if predominately composed of activity in the EM calorimeter (EM fraction > 0.95) had a large (> 0.8) quality factor (a measure of the difference between expected pulse shape and measured pulse shape). The additional quality cut imposed on the muons was to require that the transverse momentum of the MS track be greater than 10 GeV, and the difference in transverse momenta between the ID and MS tracks be less than 15 GeV. The working group also did not impose some of the criteria that were used in this thesis: it did not cut on the impact parameters of the muons and its vertexing requirement was looser, only requiring that a good vertex existed and not that both muons come from the same good vertex.

The mass range considered by the working group was also different, ranging from 66 and 116 GeV. The goal was to measure Z/γ^* and our signal/background fitting techniques were not used. Finally, only the kinematic cut choice of $p_T > 20$ GeV and $|\eta| < 2.4$ was considered. Figure 6.40 shows the results of our analysis re-tailored to be in accordance with what the ATLAS working group considered.

The C and A factor studies were also redone properly, with results shown in Figures 6.41, 6.42, and 6.43. In this case there was no need to modify Equation 6.3 and so it has been used directly with all of the components collected in Table 6.10.

Table 6.10: ATLAS Standard Model working group cross-section correction factors.

Cuts	**N**	**C**	**A**	**L**
$p_T > 20$ GeV and $\lvert\eta\rvert < 2.4$	14332	0.7883	0.4833	40237

This gives a resulting fiducial cross-section of 0.453 nb, and total cross-section of 0.935 nb for Z/γ^* in the mass interval from 66 to 116 GeV, in close agreement with the results obtained by the ATLAS working group of 0.456 nb fiducial, and 0.941 nb total.

6.16 Comparison with Theory

The total cross-sections measured in Section 6.13 are compared with theoretical predictions performed at next-to-next-to-leading order (NNLO) using the FEWZ [59] program with the MSTW08 NNLO pdfs. FEWZ calculates the NNLO cross-section

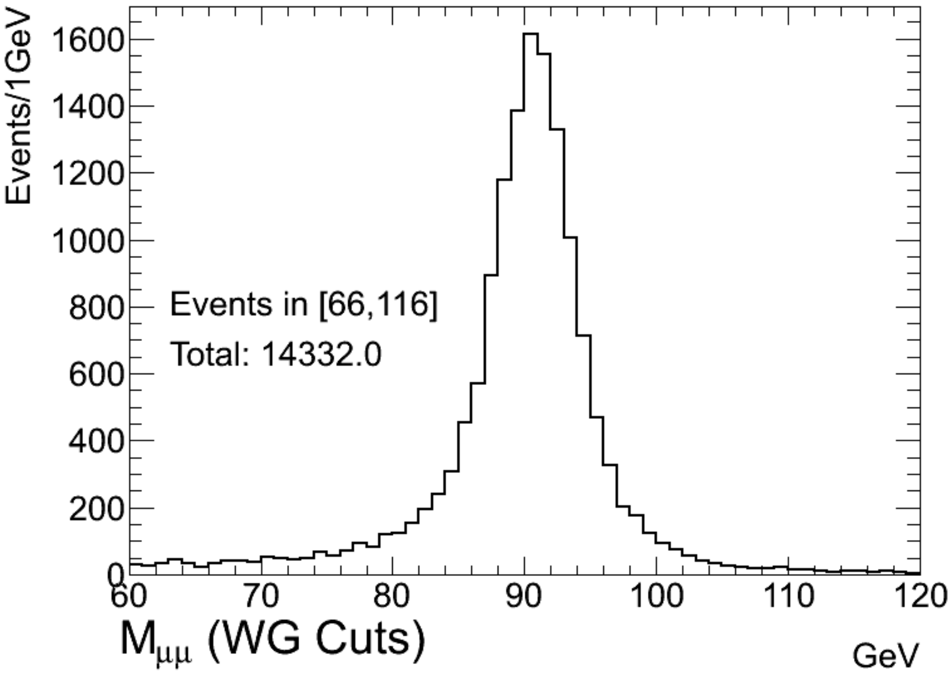

Figure 6.40: Dimuon invariant mass distribution with the ATLAS Standard Model working group selection requirements.

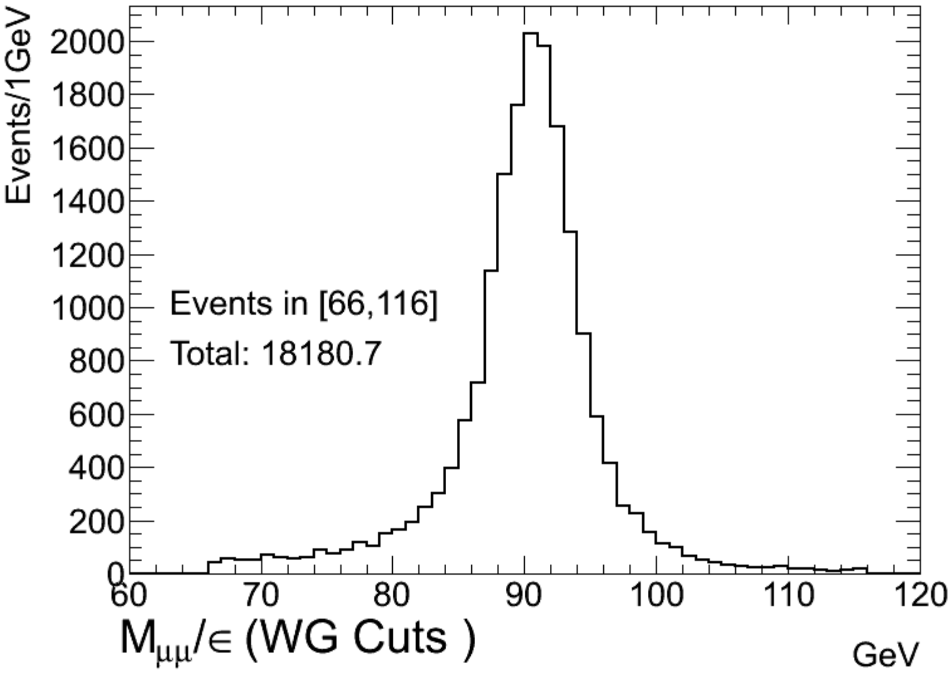

Figure 6.41: Reweighted dimuon invariant mass distribution with the ATLAS Standard Model working group selection requirements.

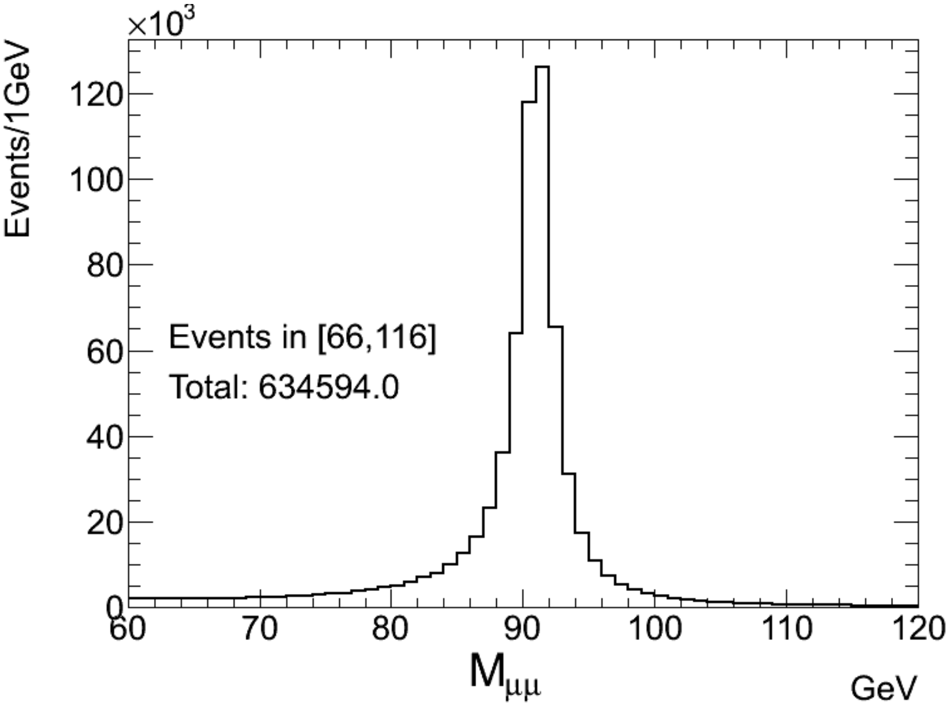

Figure 6.42: Dimuon invariant mass distribution for all Pythia "truth" events. The sample is for Z/γ^* events with final-state radiation included.

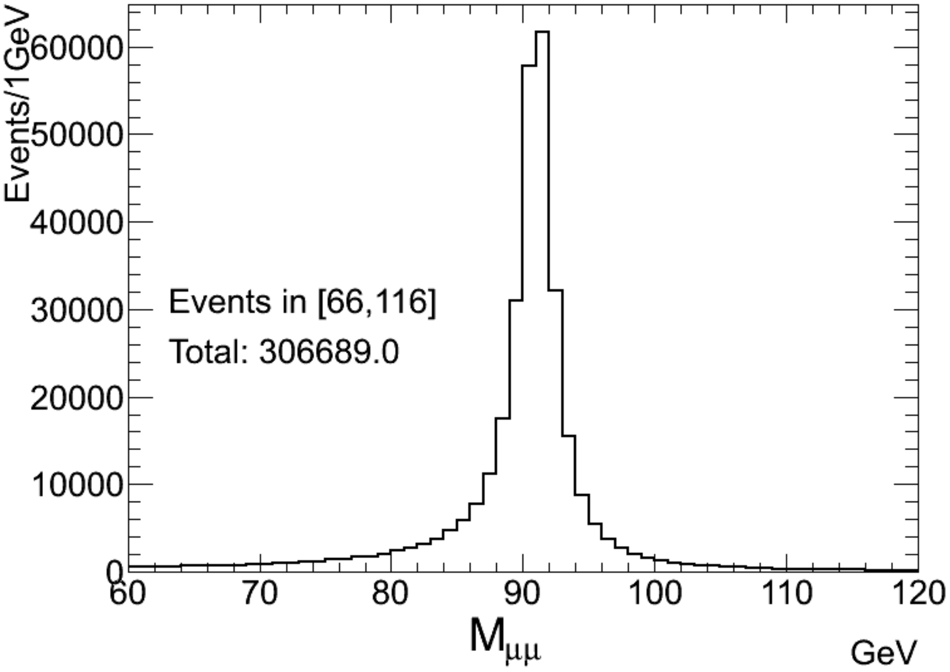

Figure 6.43: Dimuon invariant mass distribution for Pythia "truth" events when both muons satisfy $p_T > 20$ GeV and $|\eta| < 2.4$. The sample is for Z/γ^* events with final-state radiation included.

by integrating corrections to the NLO cross-section separately and summing the result. The program can be altered so as to include or exclude the γ^* contributions and the Z/γ^* interference, to restrict the invariant mass range considered, and even to impose selections on the kinematics of the decay leptons.

The result of running the program for the total Z cross-section with no γ^* and using our choice of mass window, 60 to 120 GeV, gave the result at NNLO for the total cross-section of 0.9499 nb with a 0.0018 nb statistical error on the integration process. An ATLAS study used an assortment of cross-section calculation programs (including MCFM and ZWPROD in addition to FEWZ) and examined the effects of variations on the PDFs, the value of the strong coupling α_s, as well as the renormalization and factorization scales. The result was a recommendation to estimate the systematic uncertainty on the theory prediction for the cross-section at 5% [60]. This dominates the integration uncertainty and puts the prediction from theory for the total cross-section at 0.950±0.048 nb.

In Section 6.13 we measured the value of the total cross-section to be 0.977 ± 0.047 nb for the case when the muons were required to have $p_T > 10$ GeV and $|\eta| < 2.5$ and 0.943 ± 0.041 nb for the case of $p_T > 20$ GeV and $|\eta| < 2.4$. These numbers are in agreement within errors with the theory value of 0.950 nb.

Using the option in FEWZ to add constraints on the lepton decay products, requiring $p_T > 20$ GeV and $|\eta| < 2.4$ produced a resulting NNLO fiducial cross-section of 0.447 ± 0.022 nb, while the measured fiducial cross-section for this choice was 0.455 ± 0.017 nb. For the other choice of cuts, $p_T > 10$ GeV and $|\eta| < 2.5$, the result from FEWZ was 0.523 ± 0.026 nb, while the measured value was 0.550 ± 0.023 nb. For both fiducial cross-section cases the measurements and the values predicted from theory agree within errors. Table 6.11 collects the values for the cross-sections, both fiducial and total, both measured and theory, for comparison.

Table 6.11: Comparison of measured cross-sections with predictions from theory.

	$p_T > 10$ **GeV,** $\lvert\eta\rvert < 2.5$	$p_T > 20$ **GeV,** $\lvert\eta\rvert < 2.4$
$\sigma_{fid} \times BR_{\mu\mu}$ (Measured)	0.550 ± 0.023 nb	0.455 ± 0.017 nb
$\sigma_{fid} \times BR_{\mu\mu}$ (Theory)	0.523 ± 0.026 nb	0.447 ± 0.022 nb
$\sigma_{tot} \times BR_{\mu\mu}$ (Measured)	0.977 ± 0.047 nb	0.943 ± 0.041 nb
$\sigma_{tot} \times BR_{\mu\mu}$ (Theory)	0.950±0.048 nb	

We have also used FEWZ to calculate the NNLO A factor by dividing the prediction for the fiducial cross-section with that of the total cross-section, yielding A=0.4704 for the case of muons with $p_T > 20$ GeV and $|\eta| < 2.4$ and A=0.5508 for $p_T > 10$ GeV and $|\eta| < 2.5$. In Section 6.9 these values were found to be respectively 0.4820 and 0.5626 using the Pythia samples, and 0.4745 and 0.5537 with MC@NLO. The A factor determined with FEWZ are thus found to be consistent with those obtained by Pythia and MC@NLO.

Chapter 7

Transverse Momentum and Rapidity Distributions

7.1 Introduction

We investigate the transverse momentum (p_T) and rapidity (Y) distributions of the observed Z bosons. The rapidity is defined as $\mathrm{Y}=\frac{1}{2}\ln\frac{E+p_L}{E-p_L}$ where E is the energy of the Z/γ^* boson and p_L is the longitudinal component of its momentum. Since the technique of eliminating the γ^* contribution by fitting the invariant mass distribution cannot be simply applied to these distributions, throughout this chapter the focus will be on measurements of combined Z/γ^*. The Pythia Monte Carlo generates transverse momentum for the Z/γ^* through a combination of parton showers from initial state radiation (q→ qg and q→ qγ) and explicit matrix-element inspired corrections [46]. We find good agreement between data and the prediction from the Pythia Monte Carlo for the p_T and Y distributions of the Z/γ^*. Normalized differential cross-sections for each are obtained from the truth information of the Pythia Monte Carlo and compared to results of a detailed analysis performed by an ATLAS working group.

7.1.1 Definition

The measurement of the Z/γ^* transverse momentum and rapidity can proceed along one of two main paths depending on the treatment of final state radiation (FSR) from the lepton decay products. One approach is to simply take the two leptons as measured in the detector after emission of FSR, and find the p_T and Y of the resulting lepton pair. Another involves searching for nearby FSR photons and including them in the p_T and Y measurements. The two methods each have their advantages. For simplicity, the Z/γ^* distributions presented in this thesis are based on the first approach and do not incorporate FSR. The ATLAS working group study gives results for both approaches, allowing a comparison with our analysis.

Differential cross-sections will be based on events for which the muons pass the kinematic requirements $p_T > 20$ GeV and $|\eta| < 2.4$, in addition to isolation and other analysis requirements as outlined in the previous chapter. These fiducial differential cross-sections will be normalized, $\frac{1}{\sigma}\frac{d\sigma}{dp_T}$ and $\frac{1}{\sigma}\frac{d\sigma}{dY}$, to reduce systematic errors such as those produced by uncertainties of the luminosity.

7.2 Measurement of Z/γ^* Transverse Momentum

7.2.1 Examination of Pythia Simulation

If the Z/γ^* transverse momentum distribution of Pythia Monte Carlo events, after full detector simulation, provides a good match to the recorded data, then the Pythia truth information can be used to determine the differential cross-section.

To this end we consider the p_T distribution of the Z/γ^* boson in Figure 7.1, which provides a comparison of the data and the fully simulated Pythia Monte Carlo events with the MC statistics scaled to the number of events measured in data. Considering one hundred 1 GeV bins, the agreement between data and Monte Carlo can be quantified by constructing a chi-square defined in Equation 7.1.

$$\chi^2 = \sum_{bin=1}^{100} \frac{(N_{bin}^{Data} - N_{bin}^{MC} \cdot \frac{N_{tot}^{Data}}{N_{tot}^{MC}})^2}{N_{bin}^{Data} + N_{bin}^{MC} \cdot (\frac{N_{tot}^{Data}}{N_{tot}^{MC}})^2} \tag{7.1}$$

The total chi-square for this comparison is 114.6, which given 100 bins in p_T produces a chi-square per degree of freedom (dof) of 1.15, demonstrating good agreement between the data and the Monte Carlo.

The default detector simulation used to produce Figure 7.1 is known to underestimate the muon momentum resolution. This can be seen in Figure 7.2, where the measured Z peak is broader than the simulated one. Performing a comparison chi-square test on the sixty 1 GeV bins from 60 GeV to 120 GeV gives a chi-square per dof of 9.78 indicating significant disagreement between the distributions.

We improve the simulation by introducing an additional smearing function for the

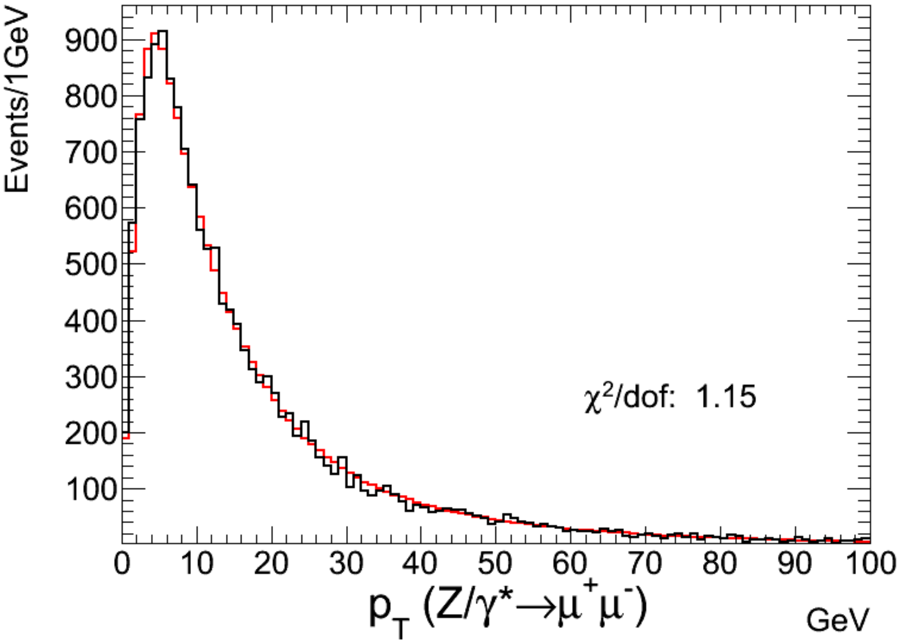

Figure 7.1: Comparison of data and Pythia transverse momentum distributions for Z/γ^* events. Both muons are required to satisfy $p_T > 20$ GeV, $|\eta| < 2.4$, and the dimuon invariant mass is restricted to fall within $60 < M_{\mu\mu} < 120$ GeV. The Pythia events (red) using the default full simulation of the ATLAS detector are normalized to the number of data events (black).

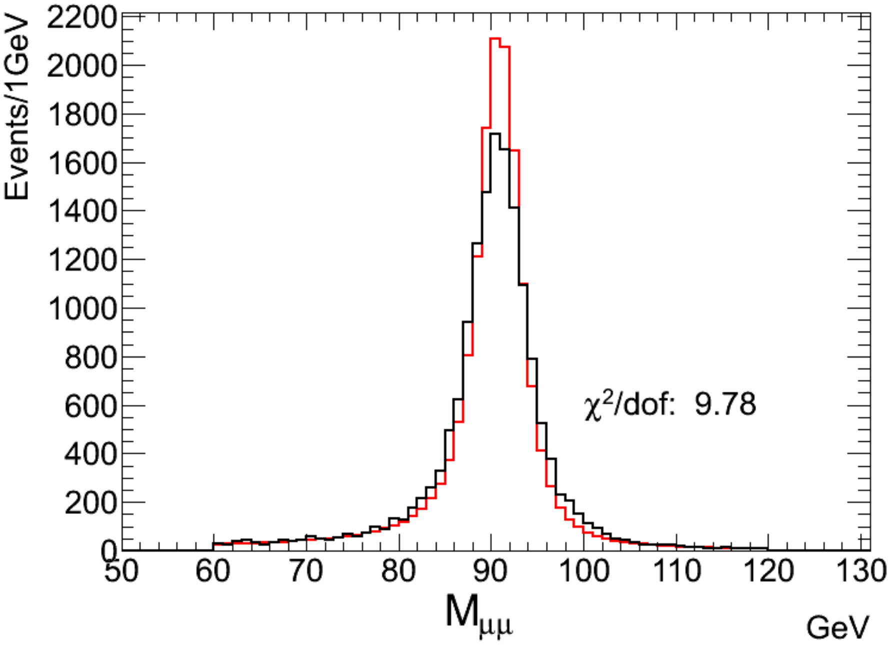

Figure 7.2: Comparison of data and PYTHIA invariant mass distributions for Z/γ^* events. Both muons are required to satisfy $p_T > 20$ GeV and $|\eta| < 2.4$. The PYTHIA events (red) using the default full simulation of the ATLAS detector are normalized to the number of data events (black).

muon momentum, given by:

$$(p_T)_{smear} = \frac{C_1 \cdot (p_T)_{default}}{1 + x \cdot C_2}. \tag{7.2}$$

An ATLAS study arrived at the values for C_1 and and C_2 empirically, considering separately the cases of muons measured in the end-cap region (C_1=1.0006 and C_2=0.0351) and those in the barrel region (C_1=0.9992 and C_2=0.0150) [61]. The value for x is a random number drawn from a Gaussian distribution with a mean of zero and unit width. After applying the additional smearing from Equation 7.2 to the momentum of the simulated Monte Carlo muons, the simulated invariant mass distribution in Figure 7.3 is in much better agreement with the data, with a chi-square per dof of 1.34.

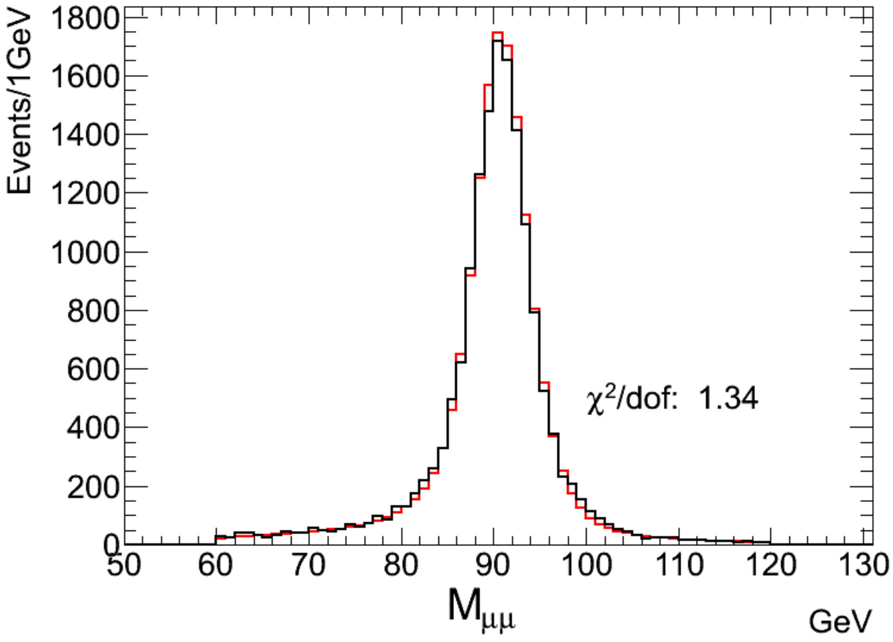

Figure 7.3: Comparison of data and smeared Pythia invariant mass distributions for Z/γ^* events. Both muons are required to satisfy $p_T > 20$ GeV and $|\eta| < 2.4$. The Pythia events (red) using the full simulation of the ATLAS detector with additional smearing as given in Equation 7.2 are normalized to the number of data events (black).

As shown in Figure 7.4 the introduction of the additional smearing has little effect on the simulated p_T distribution. Data and simulation are still in good agreement, with a chi-square per dof of 1.21.

To facilitate a comparison with another ATLAS analysis, we next selected MC events which, when fully simulated and with additional smearing, passed our analysis

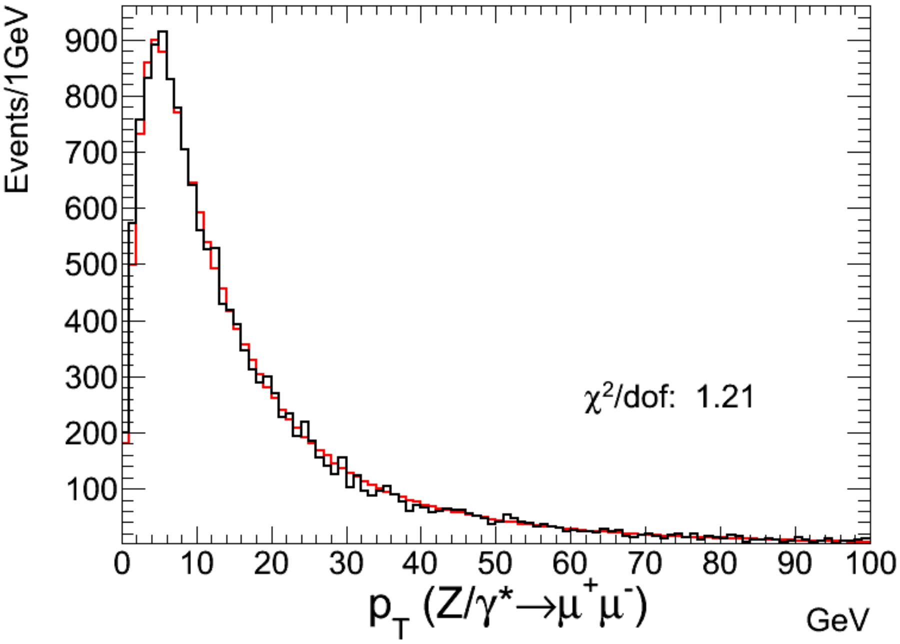

Figure 7.4: Comparison of data and smeared Pythia transverse momentum distributions for Z/γ^* events. Both muons are required to satisfy $p_T > 20$ GeV, $|\eta| < 2.4$, and the dimuon invariant mass is restricted to fall within $60 < M_{\mu\mu} < 120$ GeV. The Pythia events (red) using the full simulation of the ATLAS detector with additional smearing as given in Equation 7.2 are normalized to the number of data events (black).

requirements and fell within the mass range of $66 < M_{\mu\mu} < 116$ GeV. The PYTHIA truth information of these events was used to determine the normalized distribution for $p_T(Z/\gamma* \rightarrow \mu^+_{truth}\mu^-_{truth})$, shown in Figure 7.5. This serves as the basis for the comparison discussed in the next section.

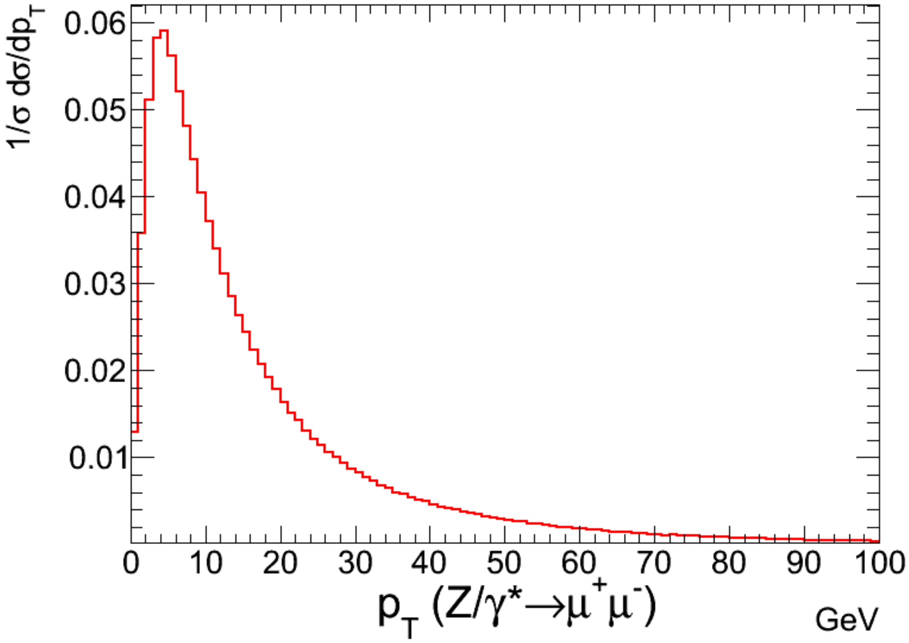

Figure 7.5: Normalized differential transverse momentum distribution for smeared PYTHIA Z/γ^* events. $(\frac{1}{\sigma}\frac{d\sigma}{dp_T})_{fid}$ has been calculated using the truth information from those events where the simulated reconstructed muons satisfies $p_T > 20$ GeV, $|\eta| < 2.4$, and $66 < M_{\mu\mu} < 116$ GeV.

7.2.2 Comparison with ATLAS Working Group Result

Relying on the good agreement between the data and the smeared MC demonstrated above, we proceed with a simplified approach to the measurement of the normalized differential cross-sections. Taking the PYTHIA truth information of the selected MC events as our measurement we compare our result with a more sophisticated treatment undertaken by an ATLAS working group. For the comparison, the dilepton mass is required to be between 66 GeV and 116 GeV, and the transverse momentum distribution is divided into seventeen variable-sized bins covering the range from 0 to 100 GeV, and ranging in size from 3 GeV for low p_T bins up to 20 GeV for the bins with highest p_T. In Table 7.1 we compare three sets of numbers for the normalized cross-section $(\frac{1}{\sigma}\frac{d\sigma}{dp_T})_{fid}$: a measurement directly from data uncorrected for detector ef-

Table 7.1: Comparison of normalized transverse momentum distributions. $(\frac{1}{\sigma}\frac{d\sigma}{dp_T})_{fid}$ are listed for uncorrected data, Pythia MC truth, and results from an ATLAS study [62]. The errors provided for the Data and MC are statistical only, while the errors provided for the ATLAS study are the result of summing statistical and systematic uncertainties in quadrature. Also given is the percent difference between Pythia truth results and the ATLAS study results.

p_T **bin (GeV)**	**Data**	Pythia **Truth**	**ATLAS Study**	**Difference**
0-3	0.0324 ± 2.7%	0.0328 ± 0.2%	0.0358 ± 5.6%	-9.15%
3-6	0.0558 ± 2.1%	0.0572 ± 0.2%	0.0568 ± 4.5%	0.70%
6-9	0.0489 ± 2.2%	0.0476 ± 0.2%	0.0469 ± 2.6%	1.47%
9-12	0.0366 ± 2.5%	0.0368 ± 0.2%	0.0358 ± 2.9%	2.72%
12-15	0.0291 ± 2.8%	0.0283 ± 0.2%	0.0276 ± 3.3%	2.47%
15-18	0.0223 ± 3.2%	0.0223 ± 0.3%	0.0220 ± 3.5%	1.35%
18-21	0.0182 ± 3.5%	0.0176 ± 0.3%	0.0174 ± 3.9%	1.14%
21-24	0.0138 ± 4.0%	0.0140 ± 0.3%	0.0137 ± 4.4%	2.14%
24-27	0.0119 ± 4.3%	0.0112 ± 0.4%	0.0117 ± 4.7%	-4.46%
27-30	0.00891 ± 4.9%	0.00925 ± 0.4%	0.00880 ± 5.4%	4.86%
30-36	0.00647 ± 4.1%	0.00698 ± 0.3%	0.00645 ± 4.6%	7.59%
36-42	0.00444 ± 4.9%	0.00496 ± 0.4%	0.00462 ± 5.4%	6.85%
42-48	0.00380 ± 5.3%	0.00364 ± 0.5%	0.00394 ± 5.8%	-8.24%
48-54	0.00283 ± 6.2%	0.00272 ± 0.6%	0.00286 ± 6.7%	-5.15%
54-60	0.00204 ± 7.2%	0.00204 ± 0.6%	0.00211 ± 7.7%	-3.43%
60-80	0.00119 ± 5.2%	0.00120 ± 0.5%	0.00128 ± 5.9%	-6.67%
80-100	0.000581 ± 7.4%	0.000539 ± 0.7%	0.000540 ± 8.5%	-0.19%

fects, the Pythia truth distribution, and finally the values from the ATLAS working group paper [62].

Generally good agreement between Pythia truth and the ATLAS study is observed, with the differences within or nearly within the errors, which were the quadratic sum of the statistical and systematic uncertainties quoted by the ATLAS study. Figure 7.6 displays the differences based on the numbers from Table 7.1. We conclude that our simple analysis provides a nice check of the results obtained by the much more complicated and sophisticated analysis of reference [62].

7.3 Measurement of Z/γ^* Rapidity

Next we consider the rapidity distribution of the Z/γ^* boson. We begin again by proceeding through the steps in Section 7.2 to demonstrate good agreement between the data and the Pythia Monte Carlo. Already having shown the need to correct the muon momentum resolution in the default Monte Carlo simulation, Figure 7.7 presents the comparison between the data and the simulated events with the addi-

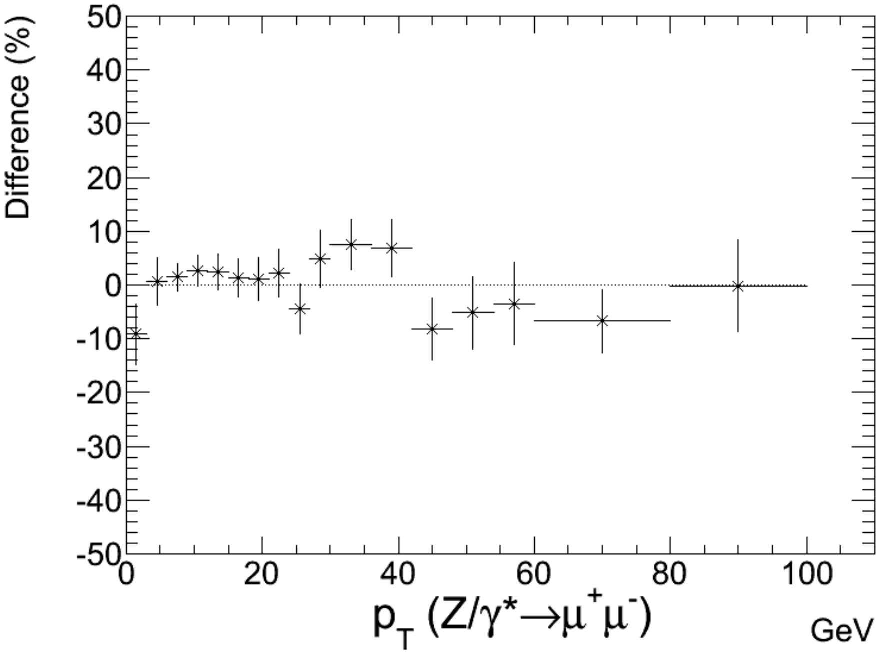

Figure 7.6: Percent difference between reference study and Pythia. $\frac{\textsc{Pythia}-ATLAS}{\textsc{Pythia}}$ plotted as a function of the transverse momentum with the ATLAS study errors applied as symmetric uncertainties.

tional smearing of Equation 7.2 applied. The same chi-square test was performed as in Section 7.2, finding good agreement ($\chi^2/dof = 0.840$) between the data and the smeared Monte Carlo.

In the case of the transverse momentum distribution we took this result as indication that the Pythia Truth was accurate and used it for a comparison with a previous ATLAS study. However, the ATLAS working group did not publish results for the rapidity distribution. We therefore proceed by correcting the data to account for detector effects, before making a final comparison with the Pythia Monte Carlo truth information, which serves as the theory prediction. In what follows we retain the standard ATLAS mass requirement 66 GeV< $M_{\mu\mu}$ <116 GeV.

7.3.1 Efficiency Corrections

Corrections for detector efficiency were discussed in depth in Section 6.8, and we summarize the important details here. Four efficiencies for muon detection were studied: the trigger system, the inner detector, the muon spectrometer, and the isolation requirement imposed upon the muons. These were studied as a function of the muon transverse momentum and pseudorapidity, and for each event we computed a single

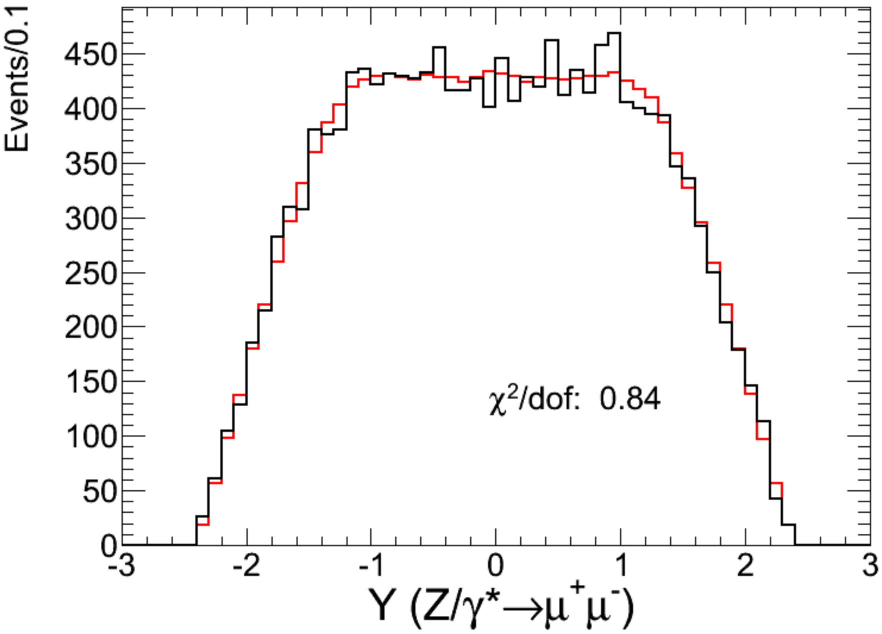

Figure 7.7: Comparison of data and Pythia rapidity distributions for Z/γ^* events. Both muons are required to satisfy $p_T > 20$ GeV, $|\eta| < 2.4$, and the dimuon invariant mass is restricted to fall within $60 < M_{\mu\mu} < 120$ GeV. The Pythia events (red) using the full simulation of the ATLAS detector with additional smearing as given in Equation 7.2 are normalized to the number of data events (black).

combined efficiency factor expressing how likely an event with those kinematics would be recorded by the detector. This was used to weight histograms of the rapidity of the dimuon pair to account for events that escape detection due to inefficiency. A comparison of the raw data and the efficiency corrected data are displayed in Figure 7.8.

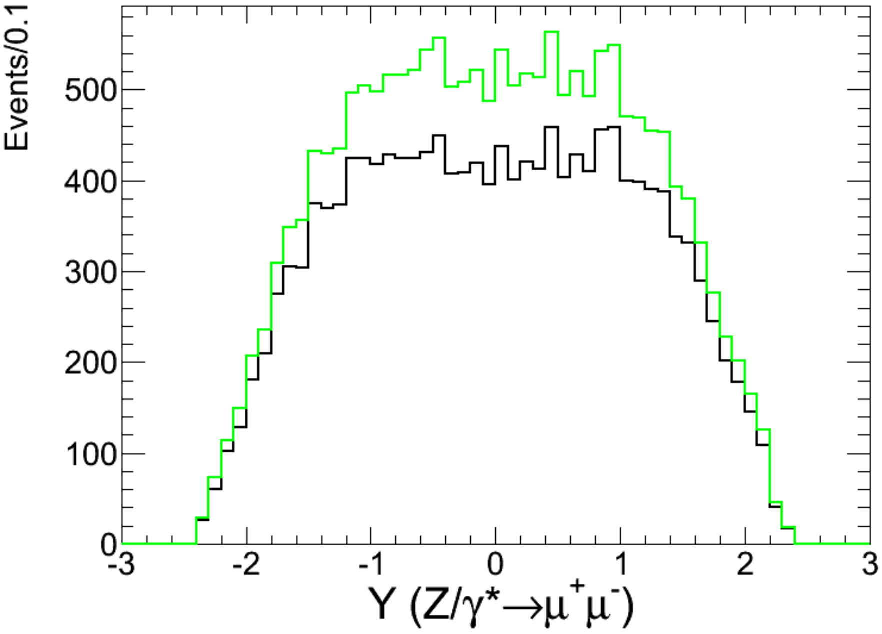

Figure 7.8: Comparison of efficiency corrected data (green) and raw data (black) rapidity distributions for Z/γ^* events. Both muons are required to satisfy $p_T > 20$ GeV, $|\eta| < 2.4$, and the dimuon invariant mass is restricted to fall within $66 < M_{\mu\mu} < 116$ GeV.

7.3.2 Rapidity Resolution Study

Next we consider the effect of detector resolution on the rapidity measurement. Uncertainties in the measurement can shift events from one rapidity bin to another. Factors such as the size of the expected shift in rapidity in a given rapidity range, as well as the number of events expected for that range must be studied to determine whether such migration effects are significant. Figure 7.9 shows the difference between the Z/γ^* rapidity for Pythia Monte Carlo events with full detector simulation and the rapidity in the Monte Carlo truth, for those events with a rapidity in the range 0<Y<0.2. The shifts in rapidity are small and centered around zero. Similar plots were made over the entire range of rapidities, and the RMS values of the distributions

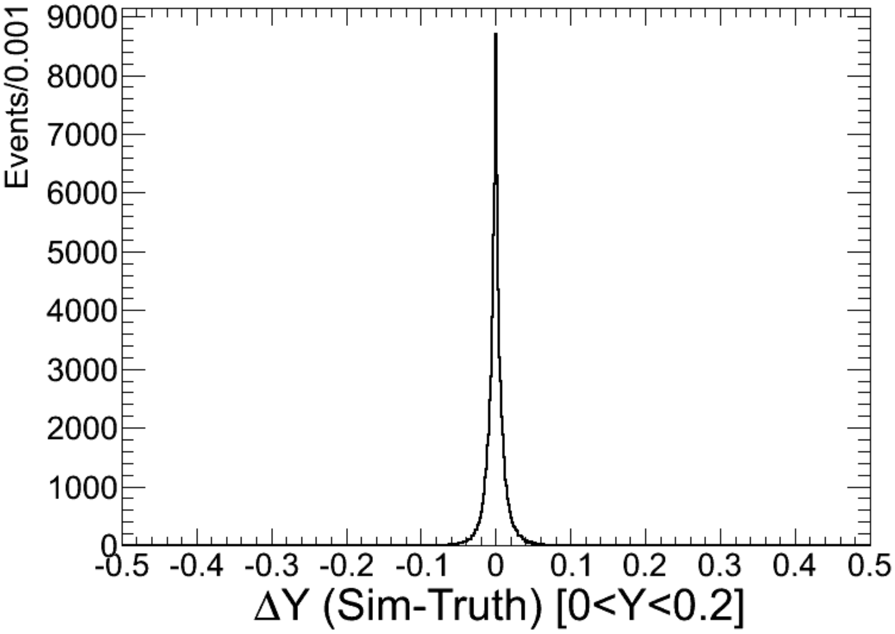

Figure 7.9: Difference between simulated and truth rapidity in Pythia Z/γ^* events. This plot is a representative example, covering muon pairs falling in the range 0<Y<0.2. The distribution is centered around zero and has an RMS value of 0.0124.

are plotted in Figure 7.10, showing a roughly constant migration width in the central rapidity ranges, and smaller migration effects at the extremes.

Using these results, one further test was performed. A simple smearing of the dimuon rapidity was made by adding a random number drawn from a Gaussian distribution with width given by the RMS value appropriate for the rapidity range. This result was also corrected for the efficiency effects and then compared with the efficiency corrected data in the absence of migration. The resulting ratio is plotted in Figure 7.11, and gives a first-order indication of the effect migration would have on data. The results show that there is no significant systematic effect, as the ratio remains flat across the entire rapidity range. Furthermore while the values of the ratio fluctuate around the average, they are consistently close to one. Compared to statistical uncertainties rapidity smearing is insignificant, and is neglected in the final analysis of the rapidity distribution.

7.3.3 Comparison between Corrected Data and MC Truth

The raw data, the data corrected for the detector effects described in the prior sections, and the truth information from Pythia were used to produce the normalized

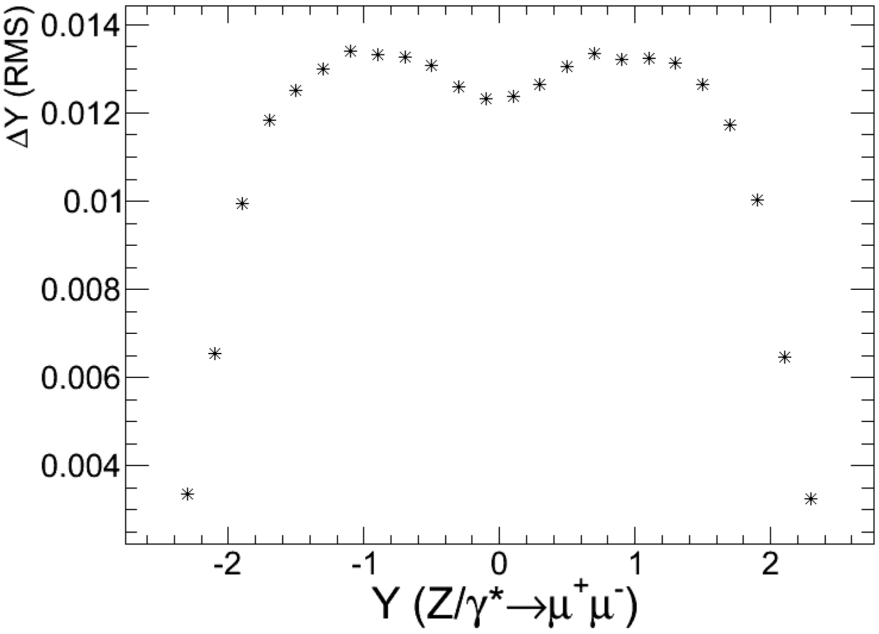

Figure 7.10: Summary of difference between simulated and rapidities in Pythia Z/γ^* events. This plot shows the RMS values for the shifts in rapidity between simulation and truth values across the full range of Z/γ^* rapidities.

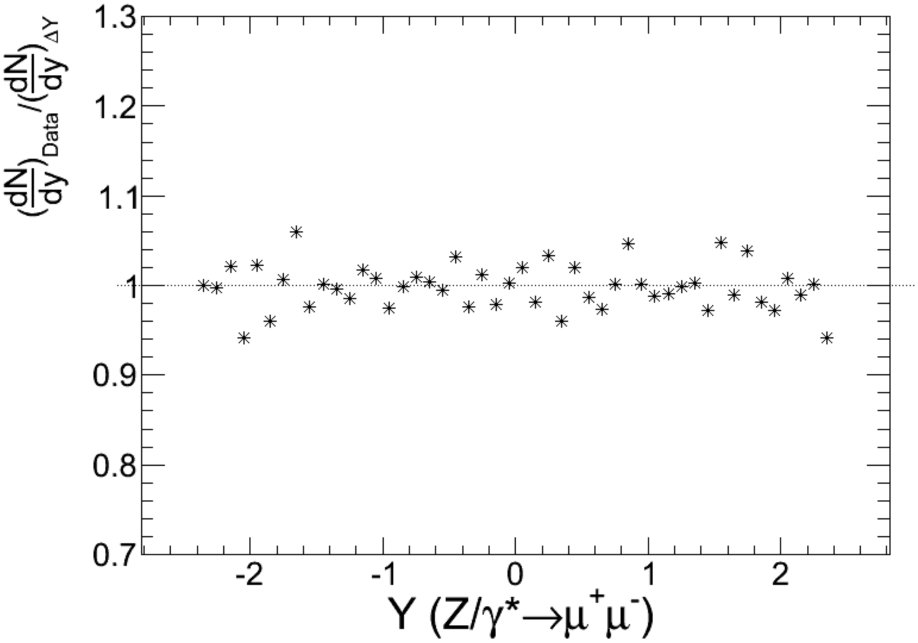

Figure 7.11: Ratio of data to data with additional rapidity smearing. The additional rapidity smearing was applied in accordance with the findings of the Monte Carlo RMS studies.

differential distributions, $(\frac{1}{\sigma}\frac{d\sigma}{dY})_{fid}(Z/\gamma* \to \mu^+_{truth}\mu^-_{truth})$, plotted in Figure 7.12. Results are also provided numerically in Table 7.2, which additionally gives the percent difference between the corrected data and the Pythia truth as well as all statistical uncertainties. The differences in the last column of Table 7.2 are also shown in Figure 7.13. The corrected data and Pythia truth agree within statistical errors across the full rapidity range.

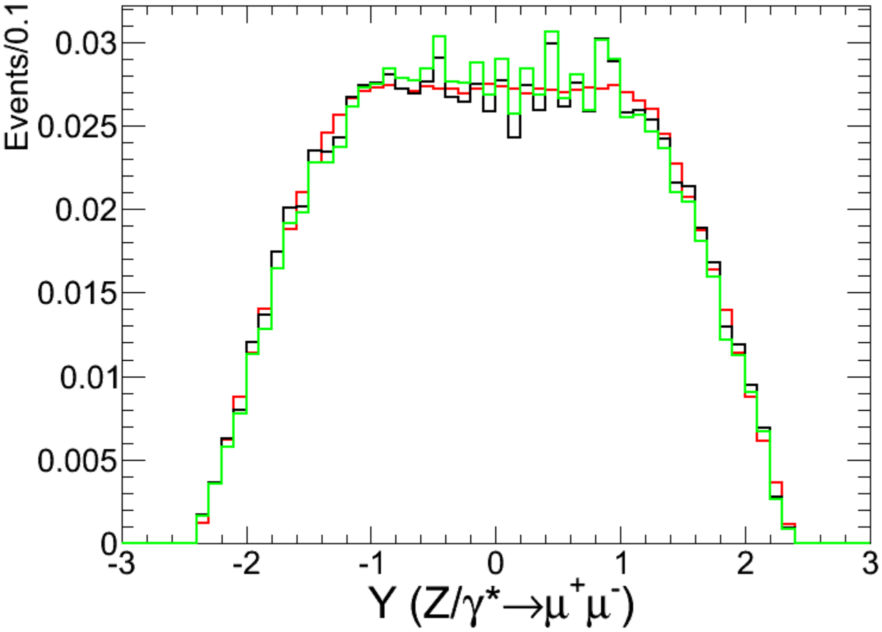

Figure 7.12: Normalized rapidity distribution for Z/γ^* events. Distributions are shown for Pythia truth information (red), raw data (black), and efficiency corrected data (green). Both muons are required to satisfy $p_T > 20$ GeV, $|\eta| < 2.4$, and the dimuon invariant mass is restricted to fall within $66 < M_{\mu\mu} < 116$ GeV.

7.3.4 Comparison of Fiducial and Total Rapidity Distributions

We note that our rapidity distribution measurement is a *fiducial* one, and thus limited by the cuts imposed on the transverse momentum and pseudorapidity of the muons. Given the good agreement between the efficiency-corrected data and the Pythia Monte Carlo truth results, we can use the Pythia program to extrapolate the fiducial rapidity distribution to the full phase space of Z/γ^* production and decay to $\mu^+\mu^-$. This is shown in Figure 7.14.

Table 7.2: Comparison of normalized rapidity distributions. $(\frac{1}{\sigma}\frac{d\sigma}{dY})_{fid}$ are listed for uncorrected data, data corrected for detector efficiency, and for Pythia MC truth. The errors are statistical only. Also given is the percent difference between Pythia truth results and the data.

Y Bin	**Raw Data**	**Corrected Data**	Pythia **Truth**	**Difference**
-2.35	0.0167 ± 19.63 %	0.0157 ± 19.68 %	0.0121 ± 2.00 %	-29.68%
-2.25	0.0386 ± 12.93 %	0.0397 ± 13.01 %	0.0357 ± 1.16 %	-11.31%
-2.15	0.0657 ± 9.93 %	0.0613 ± 10.03 %	0.0619 ± 0.88 %	0.98%
-2.05	0.0825 ± 8.88 %	0.0802 ± 8.99 %	0.0874 ± 0.74 %	8.17%
-1.95	0.1166 ± 7.48 %	0.1116 ± 7.61 %	0.1141 ± 0.65 %	2.23%
-1.85	0.1353 ± 6.95 %	0.1269 ± 7.09 %	0.1400 ± 0.59 %	9.34%
-1.75	0.1771 ± 6.08 %	0.1669 ± 6.25 %	0.1643 ± 0.54 %	-1.57%
-1.65	0.1965 ± 5.78 %	0.1877 ± 5.95 %	0.1884 ± 0.51 %	0.37%
-1.55	0.1958 ± 5.79 %	0.1921 ± 5.96 %	0.2102 ± 0.48 %	8.61%
-1.45	0.2416 ± 5.23 %	0.2332 ± 5.41 %	0.2280 ± 0.46 %	-2.29%
-1.35	0.2383 ± 5.26 %	0.2315 ± 5.45 %	0.2457 ± 0.45 %	5.79%
-1.25	0.2409 ± 5.23 %	0.2348 ± 5.42 %	0.2562 ± 0.44 %	8.35%
-1.15	0.2738 ± 4.92 %	0.2679 ± 5.12 %	0.2661 ± 0.43 %	-0.66%
-1.05	0.2731 ± 4.92 %	0.2719 ± 5.12 %	0.2706 ± 0.43 %	-0.45%
-0.95	0.2693 ± 4.96 %	0.2685 ± 5.15 %	0.2729 ± 0.43 %	1.61%
-0.85	0.2757 ± 4.90 %	0.2785 ± 5.10 %	0.2741 ± 0.42 %	-1.60%
-0.75	0.2731 ± 4.92 %	0.2785 ± 5.12 %	0.2717 ± 0.43 %	-2.48%
-0.65	0.2738 ± 4.92 %	0.2808 ± 5.12 %	0.2705 ± 0.43 %	-3.84%
-0.55	0.2776 ± 4.88 %	0.2932 ± 5.08 %	0.2736 ± 0.42 %	-7.16%
-0.45	0.2892 ± 4.79 %	0.3005 ± 4.99 %	0.2718 ± 0.43 %	-10.56%
-0.35	0.2628 ± 5.02 %	0.2712 ± 5.21 %	0.2718 ± 0.43 %	0.22%
-0.25	0.2635 ± 5.01 %	0.2738 ± 5.21 %	0.2694 ± 0.43 %	-1.65%
-0.15	0.2699 ± 4.95 %	0.2811 ± 5.15 %	0.2719 ± 0.43 %	-3.35%
-0.05	0.2544 ± 5.10 %	0.2631 ± 5.29 %	0.2751 ± 0.42 %	4.37%
0.05	0.2821 ± 4.85 %	0.2930 ± 5.05 %	0.2737 ± 0.42 %	-7.08%
0.15	0.2583 ± 5.06 %	0.2721 ± 5.25 %	0.2723 ± 0.43 %	0.05%
0.25	0.2705 ± 4.95 %	0.2791 ± 5.14 %	0.2694 ± 0.43 %	-3.58%
0.35	0.2660 ± 4.99 %	0.2769 ± 5.18 %	0.2722 ± 0.43 %	-1.73%
0.45	0.2950 ± 4.74 %	0.3040 ± 4.95 %	0.2711 ± 0.43 %	-12.11%
0.55	0.2602 ± 5.04 %	0.2664 ± 5.23 %	0.2703 ± 0.43 %	1.43%
0.65	0.2763 ± 4.89 %	0.2803 ± 5.09 %	0.2715 ± 0.43 %	-3.23%
0.75	0.2641 ± 5.00 %	0.2655 ± 5.20 %	0.2724 ± 0.43 %	2.56%
0.85	0.2937 ± 4.75 %	0.2927 ± 4.96 %	0.2723 ± 0.43 %	-7.50%
0.95	0.2950 ± 4.74 %	0.2956 ± 4.95 %	0.2744 ± 0.42 %	-7.71%
1.05	0.2570 ± 5.07 %	0.2532 ± 5.26 %	0.2701 ± 0.43 %	6.25%
1.15	0.2564 ± 5.08 %	0.2530 ± 5.27 %	0.2652 ± 0.43 %	4.57%
1.25	0.2519 ± 5.12 %	0.2452 ± 5.31 %	0.2600 ± 0.44 %	5.68%
1.35	0.2499 ± 5.14 %	0.2447 ± 5.33 %	0.2454 ± 0.45 %	0.26%
1.45	0.2177 ± 5.50 %	0.2118 ± 5.68 %	0.2274 ± 0.46 %	6.84%
1.55	0.2139 ± 5.55 %	0.2046 ± 5.72 %	0.2073 ± 0.49 %	1.29%
1.65	0.1868 ± 5.93 %	0.1789 ± 6.09 %	0.1873 ± 0.51 %	4.51%
1.75	0.1578 ± 6.44 %	0.1492 ± 6.59 %	0.1639 ± 0.55 %	8.93%
1.85	0.1301 ± 7.08 %	0.1226 ± 7.22 %	0.1398 ± 0.59 %	12.26%
1.95	0.1147 ± 7.54 %	0.1090 ± 7.67 %	0.1140 ± 0.65 %	4.43%
2.05	0.0934 ± 8.34 %	0.0890 ± 8.46 %	0.0876 ± 0.74 %	-1.61%
2.15	0.0702 ± 9.61 %	0.0680 ± 9.72 %	0.0613 ± 0.89 %	-10.94%
2.25	0.0258 ± 15.83 %	0.0244 ± 15.89 %	0.0360 ± 1.16 %	32.39%
2.35	0.0110 ± 24.27 %	0.0101 ± 24.31 %	0.0116 ± 2.04 %	13.04%

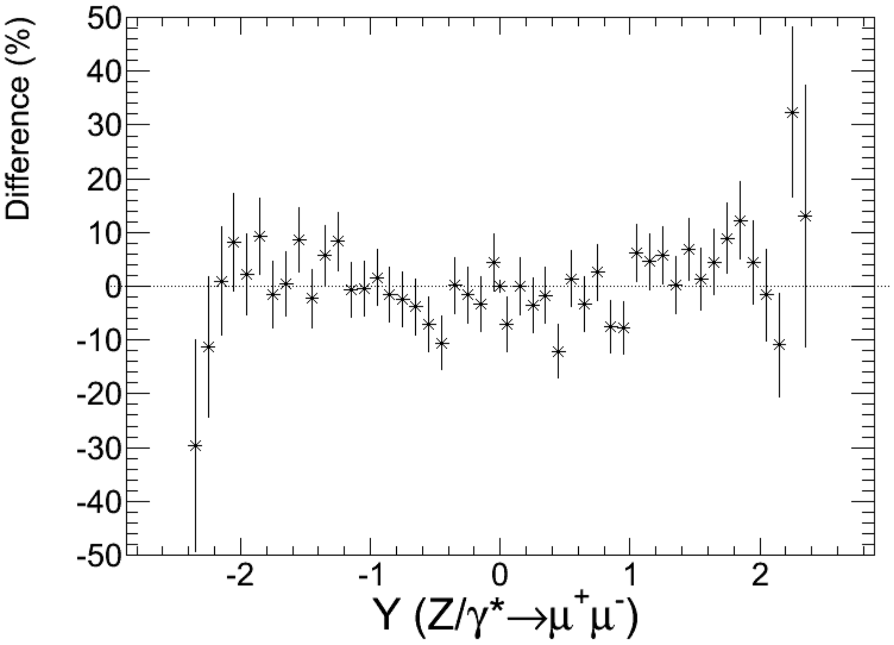

Figure 7.13: Percent difference between Pythia and corrected data. The quantity $\frac{\text{Pythia}-Data}{\text{Pythia}}$ is plotted as a function of rapidity. The errors are statistical only.

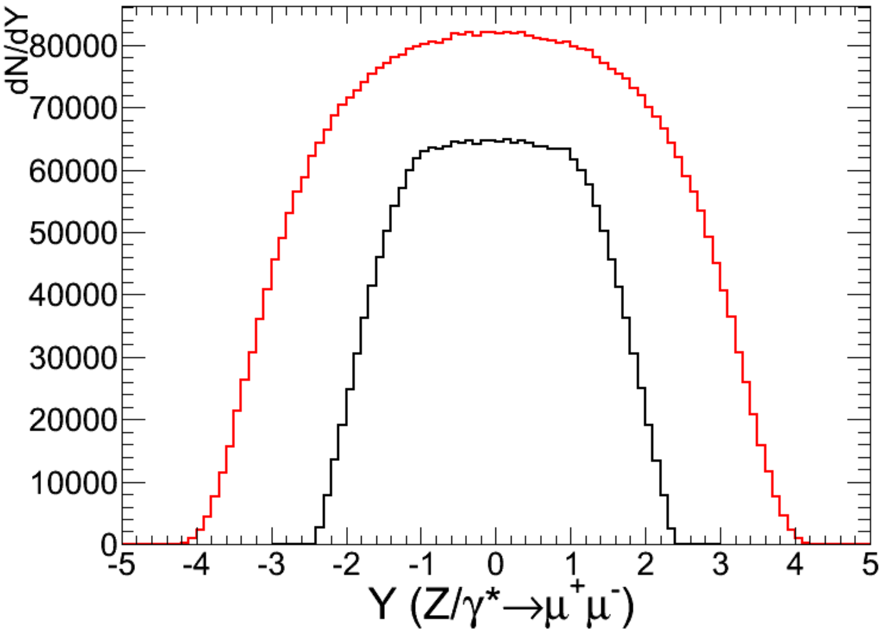

Figure 7.14: Comparison of fiducial and total rapidity distributions. Both the fiducial (black) and the total (red) distributions are based on Pythia MC truth information.

Chapter 8

Summary

This thesis presented measurements of the inclusive process $pp \to (Z \to \mu^+\mu^-) +$ anything based on 40237 nb^{-1} of data from the first year of LHC collisions at center-of-mass energy of $\sqrt{s} = 7$ TeV recorded by the ATLAS detector.

Events with $Z \to \mu^+\mu^-$ were isolated from $\gamma^* \to \mu^+\mu^-$ contributions through fitting the invariant mass of the muons with a combination of a Breit-Wigner signal and smoothly falling background. Detailed consideration was given to final-state radiation of photons and its effects on how events were classified as signal or background. Further, contributions from other background sources were confirmed to be negligible by performing a closure test using Monte Carlo generated events, as well as by referencing external data-driven studies. Four main sources of detector efficiency losses were studied and taken into account: the muon trigger, the inner detector tracking, the measurement in the muon spectrometer, and the muon isolation requirement.

Two choices for fiducial cuts on the kinematics of the muons were considered: one requiring that muons satisfy transverse momentum $(p_T)_\mu > 20$ GeV and pseudorapidity $|(\eta)_\mu| < 2.4$, the other requiring $(p_T)_\mu > 10$ GeV and $|(\eta)_\mu| < 2.5$. For both cases the invariant mass range considered was restricted to $60 < M_{\mu\mu} < 120$ GeV. This yielded two measurements for the product of the fiducial Z production cross-section with the branching ratio to muons: $(\sigma_Z)_{fid} \times BR_{\mu\mu} = 0.455 \pm 0.017$ nb for the first, and $(\sigma_Z)_{fid} \times BR_{\mu\mu} = 0.550 \pm 0.023$ nb for the second.

These fiducial cross-sections were extrapolated to the total Z production cross-section by computing acceptance factors with Monte Carlo event generators. This was done by calculating the ratio of events in the Monte Carlo truth record that satisfied the fiducial cuts to the total number of events generated. Two Monte Carlo generation programs were compared, with the value derived from the Pythia Monte Carlo being taken as the central value, and its difference with the MC@NLO Monte

Carlo being taken as a systematic error.

The extrapolation resulted in a result for the the total Z production cross-section of $(\sigma_Z)_{tot} \times BR_{\mu\mu} = 0.943 \pm 0.041$ nb for the case of $(p_T)_\mu > 20$ GeV and $|(\eta)_\mu| < 2.4$, and $(\sigma_Z)_{tot} \times BR_{\mu\mu} = 0.977 \pm 0.047$ nb for the case of $(p_T)_\mu > 10$ GeV and $|(\eta)_\mu| < 2.5$.

The FEWZ program was used to arrive at the Standard Model value predicted by theory. These calculations were performed at NNLO and gave $(\sigma_Z)_{fid} \times BR_{\mu\mu} = 0.447 \pm 0.022$ nb for the first choice of fiducial cuts, $(\sigma_Z)_{fid} \times BR_{\mu\mu} = 0.523 \pm 0.026$ nb for the second, and $(\sigma_Z)_{tot} \times BR_{\mu\mu} = 0.950 \pm 0.048$ nb for the total cross-section. In every case the measurement from data agrees with these predictions from theory.

Furthermore, an explicit comparison to an ATLAS working group study on a different luminosity sample using similar selection requirements, but with invariant mass restricted to $66 < M_{\mu\mu} < 116$ GeV, was also found to be in good agreement.

The second set of measurements presented in this thesis are the normalized transverse momentum and rapidity distributions of $Z/\gamma^* \rightarrow \mu^+\mu^-$ for dimuon invariant mass in the range $66 < M_{\mu\mu} < 116$ GeV. In both cases the distribution of the data agreed well with the distribution of PYTHIA Monte Carlo events put through the full detector simulation.

A comparison was made for the normalized p_T distribution derived from the PYTHIA truth record information with a sophisticated analysis produced by the official ATLAS Standard Model working group. The distributions were found to agree within their uncertainties. For the rapidity distribution, the data were corrected for detector effects and then compared to the PYTHIA truth. Again, good agreement was found between these rapidity distributions.

Appendix A

Runlist

The following is the list of runs and luminosity blocks which completely describes the dataset being used for the analysis of this thesis. It is a standard Good Run List (GRL) endorsed by the ATLAS subgroup for W and Z boson measurements and was posted to a public repository by Alberto Belloni.[63] The following tables list the run numbers as well as the proper luminosity block identification (LBID) for the start and end of the good quality period(s) of the run.

Table A.1: Good Run List for trigger period 1

Run Number	Starting LBID	Ending LBID	Luminosity (nb^{-1}).
152844	195	234	0.00552805
152845	111	349	0.0262252
152878	99	214	0.0250458
152933	46	173	0.0210681
152994	293	353	0.00539162
153030	120	203	0.0224983
153134	354	573	0.0261839
153136	249	253	0.00067719
153159	87	177	0.0113443
153200	145	178	0.00737709
153565	258	953	0.664095
153599	413	440	0.0213917
154810	158	220	0.152803
154813	8 68	38 187	0˙2995408 .
154815	7	38	0.0624522
154817	9	287	0.533888
154822	177	365	0.427019
155073	82	407	1.17645
155112	127	625	3.57969
155116	8	93	0.51253
155160	240	503	1.32921
155228	131	148	0.0410214
155280	343	375	0.06087
155569	228	467	0.990926
155634	144	333	1.07711
155669	264	311	0.424034
155678	241	308	1.19245
155697	256	506	3.60054
156682	405	512	1.33433
158045	117	177	0.720508
158116	114	554	15.7735
158269	5	81	3.52857
158299	378	434	1.06514
158392	218 358 367	340 358 447	. 7.5512182 .
158443	210	230	0.809174
158466	265	277	1.19038
158545	237	261	1.43914
158548	111	304	10.8137
158582	40	372	17.5338
158632	163	272	5.61342
158801	135	311	7.1641
158975	87 315	282 352	21˙94301 .
159041	106	392	28.7418
159086	117	556	59.0882
159113	261	519	28.3792
159179	222	334	15.7138
159202	187	269	9.94056
159203	3	82	8.39393
159224	249	813	67.7974
Period 1 Subtotal			330.83224085

Table A.2: Good Run List for trigger period 2

Run Number	Starting LBID	Ending LBID	Luminosity (nb^{-1}).
160387	155	394	59.1991
160472	140	521	79.8245
160479	296	320	4.69852
160530	188	625	95.6923
160613	108	323	54.9592
160736	206	263	16.8286
160800	3	87	23.235
160801	3	423	86.304
160879	113	563	89.8295
160899	114	128	4.80642
160953	202	260	21.7395
160954	111	136	8.74339
160958	3	214	43.9739
160963	3	15	2.33397
160975	78	99	4.47556
160980	10	39	8.98622
161118	7	103	34.0418
161379	118	500	103.538
161407	75	177	40.7803
161520	136	498	116.745
161562	41	338	91.2749
161948	349	701	89.3892
162347	119	546	227.963
162526	118	501	272.883
162576	3	65	50.8422
162577	4	12	6.41677
162620	166	237	72.0709
162623	4	338	245.142
162690	264	642	350.295
162764	138	146	104.94505
	148	237	
162843	114	517	328.28
162882	122	448	299.326
165591	73	466	158.803
165632	183	607	621.469
165703	105	146	87.5158
165732	91	499	1102.1515
	549	564	
165767	198	575	1089.5
165815	123	165	168.082
165817	3	7	0.234456
165818	3	94	267.728
Period 2 Subtotal			6535.046556

Table A.3: Good Run List for trigger period 3

Run Number	Starting LBID	Ending LBID	Luminosity (nb^{-1}).
165821	3	89	258.594
165954	111	164	223.979
165956	4	23	101.375
166097	150	215	315.788
166142	136	295	774.674
166143	4	62	263.116
166198	93	157	1462.01
	290	520	
166466	81	276	1651.95
166658	144	429	2258.65
166786	267	541	2212.88
166850	146	310	6.45732
166856	142	165	356.318
166924	51	200	1236.49
166927	7	104	586.575
166964	319	333	212.376
Period 3 Subtotal			11921.23232

Table A.4: Good Run List for trigger period 4

Run Number	Starting LBID	Ending LBID	Luminosity (nb^{-1}).
167575	125	138	121.471
167576	3	293	3754.06
167607	86	430	5477.1
167661	372	439	1335.62
167680	33	266	3680.99
167776	124	546	6050.68
167844	79	270	2533.09
Period 4 Subtotal			22953.011

Table A.5: Run Period Summary

Run Number	Starting LBID	Ending LBID	Luminosity (nb^{-1}).
Period 1 Subtotal			330.83224085
Period 2 Subtotal			6535.046556
Period 3 Subtotal			11921.23232
Period 4 Subtotal			22953.011
Grand Total			41740.12211685

Appendix B

D3PD Requirements

The thesis analysis relies on derived physics data (DPD) files produced from the ATLAS standard analysis object data (AOD) files. This section lists the requirements associated with this process. The conversion script looks at objects in the AOD container titled "ElectronAODCollection" for electrons, "PhotonAODCollection" for photons, and "MuidMuonCollection" and "StacoMuonCollection" for the two different muon reconstruction algorithms. Following that, it examines each object in the container to see whether it passes selction cuts. For electrons the cut is that the cluster transverse energy (cet) is greater than 10GeV, and that the absolute value of the cluster pseudorapidity (ceta) is less than 2.7. For muons each collection is examined separately for whether the transverse momentum of the muon (mu_muid.pt() or mu_staco.pt()) is greater than 10GeV and the absolute value of the muon pseudorapidity (mu_muid.eta() or mu_staco.eta()) must again be less than 2.7. The conversion program tallies how many of each object pass its criteria and then executes the final judgment. While the machinery is in place to allow photons to enter in to the calculation, for the files that were analyzed in this thesis, the only requirements were on the leptons, and that either the sum of electrons and muid muons was greater than one, or the sum of electrons and staco muons was greater than one. There were no other requirements placed on the event (e.g. missing transverse energy).

Bibliography

[1] G. Kane. *Modern Elementary Particle Physics: The Fundamental Particles and Forces?* Perseus Publishing, 1993.

[2] A. Pich. The Standard Model of Electroweak Interactions. May 2007. arXiv:0705.4264v1 [hep-ph].

[3] M. Maltoni, T. Schwetz, M. A. Tortola, and J. W. F. Valle. Status of global fits to neutrino oscillations. *New J. Phys.*, 6:122, 2004. arXiv:hep-ph/0405172.

[4] M. C. Gonzalez-Garcia and Y. Nir. Developments in neutrino physics. *Rev. Mod. Phys.*, 75:345–402, 2003. arXiv:hep-ph/0202058.

[5] A. Djouadi. The Anatomy of electro-weak symmetry breaking. I: The Higgs boson in the standard model. *Phys. Rept.*, 457:1–216, 2008. arXiv:hep-ph/0503172.

[6] A. Pich. Aspects of Quantum Chromodynamics. January 2000. arXiv:hep-ph/0001118v1.

[7] K. Nakamura et al. (Particle Data Group). Review of Particle Physics. *J. Phys.*, G 37, 075021, 2010.

[8] A. Leike, T. Riemann, and J. Rose. S matrix approach to the Z line shape. *Phys. Lett.*, B273:513–518, 1991. arXiv:hep-ph/9508390v1.

[9] H. Lai et al. New parton distributions for collider physics. *Phys. Rev.*, D82:074024, 2010. arXiv:1007.2241v3 [hep-ph].

[10] A. D. Martin, W. J. Stirling, R. S. Thorne, and G. Watt. Parton distributions for the LHC. *Eur. Phys. J.*, C63:189–285, 2009. arXiv:0901.0002v3 [hep-ph].

[11] O. S. Brüning et al. *LHC Design Report.* CERN, Geneva, 2004. CERN-2004-003-V-1, CERN-2004-003-V-2, CERN-2004-003-V-3.

[12] CERN. *LEP Design Report*. CERN, Geneva, 1984. CERN-LEP-84-01.

[13] L. Evans. LHC status report. In *LHC Experiments and World LCG Resources Review Boards*. CERN, November 2008. EDMS Document 976647.

[14] R. Ley et al. Cern accelerators. `http://ps-div.web.cern.ch/ps-div/PSComplex/accelerators.pdf`, May 2001. Accessed August 4, 2011.

[15] AC Team. Diagram of an LHC dipole magnet. Schéma d'un aimant dipôle du LHC, June 1999. CERN-DI-9906025.

[16] The ALICE Collaboration. The ALICE experiment at the CERN LHC. *JINST*, 3:S08002, 2008.

[17] The LHCb Collaboration. The LHCb Detector at the LHC. *JINST*, 3:S08005, 2008.

[18] The ATLAS Collaboration. Luminosity Determination Using the ATLAS Detector. Technical Report ATLAS-CONF-2010-060, CERN, Geneva, July 2010.

[19] S. van der Meer. Calibration of the effective beam height in the ISR. Technical Report CERN-ISR-PO-68-31, CERN, Geneva, 1968.

[20] D. Belohrad et al. Commissioning and First Performance of the LHC Beam Current Measurement Systems. CERN-BE-2010-015. CERN-ATS-2010-100.

[21] E. Metral. LHC Beam parameters: pushing the envelope? In *2nd Evian 2010 Workshop on LHC Beam Operation*. CERN, December 2010.

[22] CERN Press Release. Interim summary report on the analysis of the 19 September 2008 incident at the LHC, October 2008. CERN PR14.08; EDMS Document 973073.

[23] L. Rossi. The subtle side of superconductivity. *CERN Cour.*, 50(7):27–30, 2010.

[24] CERN Press Release. Follow up of the incident of 19 September 2008 at the LHC, December 2008. CERN PR17.08.

[25] The ATLAS Collaboration. *ATLAS Inner Detector: Technical Design Report*. CERN, Geneva, 1997. ATLAS-TDR-004.

[26] The ATLAS Collaboration. *Expected Performance of the ATLAS Experiment: Detector, Trigger and Physics.* CERN, Geneva, 2009. arXiv:0901.0512; CERN-OPEN-2008-020.

[27] The ATLAS Collaboration. The ATLAS Experiment at the CERN Large Hadron Collider. *JINST*, 3:S08003, 2008.

[28] The ATLAS Collaboration. *ATLAS Muon Spectrometer: Technical Design Report.* CERN, Geneva, 1997. ATLAS-TDR-010.

[29] J. Wotschack. ATLAS Muon Chamber Construction Parameters for CSC, MDT, and RPC chambers. Technical Report ATL-MUON-PUB-2008-006, CERN, Geneva, April 2008.

[30] The ATLAS Collaboration. Physics pp v1 LVL1 menu. `https://twiki.cern.ch/twiki/bin/viewauth/Atlas/PhysicsPPV1_LVL1`. Accessed August 4, 2011.

[31] The ATLAS Collaboration. Trigger twiki documentation. `https://twiki.cern.ch/twiki/bin/viewauth/Atlas/MuonTriggerDocLvl2muFast`. Accessed August 4, 2011.

[32] G. Siragusa et al. The muon trigger in ATLAS. Technical Report ATL-COM-DAQ-2007-041, CERN, Geneva, October 2007.

[33] The ATLAS Collaboration. Trigger twiki documentation. `https://twiki.cern.ch/twiki/bin/viewauth/Atlas/MuonTriggerDocEFTrigMoore`. Accessed August 4, 2011.

[34] The TrigMOORE group. The ATLAS muon event filter. `https://twiki.cern.ch/twiki/bin/viewauth/Atlas/MuonHLTReviewEF`, June 2006. Accessed August 4, 2011.

[35] *ATLAS detector and physics performance: Technical Design Report, 1.* Technical Design Report ATLAS. CERN, Geneva, 1999. ATLAS-TDR-014.

[36] D. Fassouliotis et al. Muon identification using the MUID package. Technical Report ATL-COM-MUON-2003-003, CERN, Geneva, November 2000.

[37] D. Adams et al. Track reconstruction in the ATLAS muon spectrometer with MOORE. Technical Report ATL-SOFT-2003-007, CERN, Geneva, May 2003.

[38] A Formica. Design, implementation and deployment of the Saclay muon reconstruction algorithms (Muonbox/y) in the Athena software framework of the ATLAS experiment. Technical Report cs.CE/0306105, June 2003.

[39] E. Moyse, O. Ouraou, D. Quarrie, and N. van Eldik. Muon reconstruction integration task force: Final report. Technical Report ATL-COM-SOFT-2011-003, CERN, Geneva, November 2010.

[40] The ATLAS Collaboration. Luminosity Determination at $\sqrt{s} = 7$ TeV using the ATLAS Detector at the LHC. Technical Report ATL-COM-LUM-2010-029, CERN, Geneva, September 2010.

[41] The ATLAS Collaboration. *ATLAS Computing: Technical Design Report*. CERN, Geneva, 2005. ATLAS-TDR-017.

[42] D. Adams et al. The ATLAS Computing Model. Technical Report ATL-SOFT-2004-007, CERN, Geneva, December 2004.

[43] I. Ueda et al. ATLAS Operations: Experience and Evolution in the Data Taking Era. October 2010. ATL-SOFT-SLIDE-2010-359.

[44] C. Eck et al. *LHC Computing Grid: Technical Design Report*. CERN, Geneva, 2005. LCG-TDR-001.

[45] The ATLAS Collaboration. ATLAS Monte Carlo tunes for MC09. Technical Report ATL-PHYS-PUB-2010-002, CERN, Geneva, Mar 2010.

[46] T. Sjostrand, S. Mrenna, and P. Skands. PYTHIA 6.4 Physics and Manual. *JHEP*, 05:026, 2006. arXiv:hep-ph/0603175v2.

[47] A. Sherstnev and R. S. Thorne. Parton Distributions for LO Generators. *Eur. Phys. J.*, C55:553–575, 2008. arXiv:0711.2473v3 [hep-ph].

[48] S. Frixione and B. R. Webber. Matching NLO QCD computations and parton shower simulations. *JHEP*, 06:029, 2002. arXiv:hep-ph/0204244v2.

[49] S. Frixione et al. The MC@NLO 4.0 Event Generator. 2010. arXiv:1010.0819v1 [hep-ph].

[50] S. Agostinelli et al. GEANT4: A simulation toolkit. *Nucl. Instrum. Meth.*, A506:250–303, 2003.

[51] A. G. Buckley. Simulation strategies for the LHC ATLAS experiment. Technical Report ATL-COM-SOFT-2010-065, CERN, Geneva, November 2010.

[52] The ATLAS Collaboration. ATLAS Luminosity Calculator. `https://atlas-datasummary.cern.ch/lumicalc`.

[53] The ATLAS Collaboration. Updated Luminosity Determination in pp Collisions at $\sqrt{s}$=7 TeV using the ATLAS Detector. Technical Report ATLAS-CONF-2011-011, CERN, Geneva, March 2011.

[54] The ATLAS Collaboration. A measurement of the total $W^{\pm}$ and Z/γ^{*} cross sections in the e and μ decay channels and of their ratios in pp collisions at $\sqrt{s}$ = 7 TeV with the ATLAS detector. Technical Report ATLAS-CONF-2011-041, CERN, Geneva, March 2011.

[55] P. Golonka and Z. Was. PHOTOS Monte Carlo: a Precision tool for QED corrections in Z and W decays. *Eur. Phys. J.*, C45:97–107, 2006. arXiv:hep-ph/0506026v2.

[56] J. R. Taylor. *An Introduction to Error Analysis: The Study of Uncertainties in Physical Measurements.* University Science Books, 1997.

[57] M. R. Whalley, D. Bourilkov, and R. C. Group. The Les Houches Accord PDFs (LHAPDF) and Lhaglue. 2005. `http://hepforge.cedar.ac.uk/lhapdf/`; arXiv:hep-ph/0508110v1.

[58] D. Stump et al. Inclusive jet production, parton distributions, and the search for new physics. *JHEP*, 10:046, 2003. arXiv:hep-ph/0303013v1.

[59] R. Gavin, Y. Li, F. Petriello, and S. Quackenbush. FEWZ 2.0: A code for hadronic Z production at next-to- next-to-leading order. *Comput. Phys. Commun.*, 182:2388–2403, 2011. arXiv:1011.3540v1 [hep-ph].

[60] J. Butterworth et al. Single Boson and Diboson Production Cross Sections in pp Collisions at $\sqrt{s}$=7 TeV. Technical Report ATL-COM-PHYS-2010-695, CERN, Geneva, August 2010.

[61] O. Arnaez et al. A first measurement of the transverse momentum distribution of Drell-Yan lepton pairs at $\sqrt{s}$=7 TeV with ATLAS. Technical Report ATL-COM-PHYS-2011-233, CERN, Geneva, March 2011.

[62] The ATLAS Collaboration. Measurement of the transverse momentum distribution of Z/γ^* bosons in proton-proton collisions at $\sqrt{s}$=7 TeV with the ATLAS detector. 2011. arXiv:1107.2381v1 [hep-ex].

[63] A. Belloni. W/Z GRL for I2 period - 167776-16784. Private correspondence; `https://espace.cern.ch/atlas-perf-muon-sharepoint/Lists/WZ%20Muon%20Observation/AllItems.aspx`.